Fall 11-14-2018

Acoustofluidics and Soft Materials Interfaces for Biomedical Applications

Frank A. Fencl
University of New Mexico

Recommended Citation

Fencl, Frank A.. "Acoustofluidics and Soft Materials Interfaces for Biomedical Applications." (2018). https://digitalrepository.unm.edu/bme_etds/21

Frank A. Fencl
Candidate

Chemical and Biological Engineering
Department

This dissertation is approved, and it is acceptable in quality and form for publication:

Approved by the Dissertation Committee:

Nick J. Carroll, Chairperson

Steven W. Graves

Gabriel P. Lopez

Andrew P. Shreve

Menake E. Piyasena

ACOUSTOFLUIDICS AND SOFT MATERIALS INTERFACES FOR BIOMEDICAL APPLICATIONS

by

FRANK A. FENCL

B.S., Biology, University of New Mexico, 2010
M.S. Biomedical Engineering, University of New Mexico, 2016

DISSERTATION

Submitted in Partial Fulfillment of the
Requirements for the Degree of

Doctor of Philosophy
Engineering

The University of New Mexico
Albuquerque, New Mexico

December 2018

Acknowledgements

I would like to thank my advisor Dr. Nick Carroll for his expertise, advice, and support which has helped me reach this milestone. Dr. Carroll welcomed me to his lab during the onset of his academic career as a Professor. Without Dr. Carroll’s constant reinforcement and positive attitude, I would not have been able to achieve what I have with his group in such a short time span. His collaborators and undergraduate group have been incredible in their hard work and support as well. Additionally, I would like to thank Dr. Steven Graves for introducing me to the field of acoustic flow cytometry and who mentored me during my initial time as a graduate student. My experience and contribution to the field would not have occurred without his mentorship. I would like to thank him for the opportunity to present our work at the various CYTO conferences I attended. I would also like to thank Dr. Gabriel Lopez for his expertise and professionalism during my graduate career. His depth of knowledge and success have motivated me to continue this field of research in my professional career. I also need to thank Dr. Andrew Shreve who has worked diligently with me on my manuscripts. Dr. Shreve’s patience and vast knowledge has been integral in my data analysis and experimental design. Additionally, I thank Dr. Menake Piyasena for not only befriending me during my first few months, but also training me in the design and theory behind acoustofluidic devices.

To my wife Emily Fencl who has been a selfless support over these last few years. Thank you for encouraging me and keeping me sane through these times. I really appreciate going on our many adventures together and in encouraging me in taking this next big step in my life. Thank you for coming to my practice talks and conferences, having you by my side has been wonderful even though I am sure you are sick of hearing the word “acoustics” by now.

I would like to acknowledge my colleagues and the undergrads who I have had the pleasure mentoring over the last few years. I would like to specifically acknowledge Aidira Macias Gonzales who I have had the pleasure mentoring over the last two years in Dr. Carroll’s group. Her hard work, punctuality, and organization have been unmatched. The various collaborations with other students in UNM’s center for biomedical engineering has also helped my success over the years.

To my family and friends both within the academic setting and out, you have been important in encouraging me throughout this time and in maintaining my trajectory throughout each landmark up to my defense. I appreciate you all listening to my practice talks and even sometimes looking at my papers giving external feedback which has been invaluable. I enjoy our Friday nights where I can be myself and enjoy doing activities outside of research, so thank you.

Acoustofluidics and Soft Materials Interfaces for Biomedical Applications

by

Frank A. Fencl

B.S. Biology, University of New Mexico, 2010
Ph.D. Engineering, University of New Mexico, 2018

Abstract

This dissertation describes fabrication of devices and other tools for biomedical applications through the integration of acoustofluidic systems with bio separation assays, instrumentation components, and soft materials interfaces. For example, we engineer a new class of transparent acoustic flow chambers ideal for optical interrogation. We demonstrate efficacy of these devices by enhancing the signal for high throughput acoustic flow cytometry, capable of robust particle focusing across multiple parallel flowing streams. We also investigate an automated sampling system to determine the parameters of transient particle stream focusing in between sample boluses and air bubbles to model a high throughput, multi-sampling acoustic flow cytometry platform. As an extension of our acoustic separations work, we have created a proof of concept lab in a syringe assay to separate elastomeric biofunctionalized negative acoustic contrast particles (NACs) from red blood cells in dilute blood. Finally, we overcome the challenge of fabricating cell culture hydrogels in water/water emulsion systems by engineering an easily deployable microfluidic device that uses acoustic actuation from an audio speaker to create culture microgels that generate cancer cell spheroid-like assemblies. Across all these application spaces, we have illustrated the versatility of integrating acoustofluidic technologies and soft materials across multiple biomedical engineering platforms.

Table of Contents

Table of Figures

Chapter 1 Introduction: Acoustic Standing Waves and Soft Materials for Biomedical Applications

1.1 Integrating acoustics for biomedical equipment

The global human population has grown from approximately 1.65 billion to 6 billion in the 20th century alone.[1] This population growth has led to various global health problems, such as the spread of disease. Less developed countries are greatly affected, as the infrastructure to house large-scale hospitals simply does not exist. This can be mitigated with portable devices and medical laboratory assay technologies which enable medical doctors in these countries to rapidly diagnose at the point of care.[2] Developed countries are having problems as well but largely with patient throughput and rising costs for healthcare spending. For example, in 2016, the U.S. health care spending per person amounted to $10,348 USD or collectively, a total of 17.9 percent of the overall share of gross domestic product.[3] The burden of these costs has been felt across all classes in developed countries. The growth of global healthcare systems has been revolutionary in the treatment of people across all classes but has made current medical systems stressed under the enormous influx of hospital inpatients. Hospitalists have never been in greater demand as their numbers are less than the amount needed to treat the patients admitted. Modern technology is constantly evolving the capability to more rapidly and accurately diagnose ailments so that the retention time of patients is minimized. Lessening the time to diagnose and then treat patients allows for more people to be accurately treated and discharged so that hospitals can better manage high quality inpatient throughput. In this regard, biomedical instruments and equipment have been important in the early diagnosis for the administration of proper treatments for many diseases.

Technological evolution for these diagnostic tools has been progressing on several different fronts. Easily deployable devices for sample analytics and platforms for tissue growth are on the forefront of solving these issues. Integrating acoustic, or sound wave-based technologies, has aided in many of these tools. Acoustics have historically been used for instruments spanning from ultrasound mapping of pre-nascent infants and tumors, to the separation of key biosensors and elements in blood samples.

Separating and spatially controlling particles in a blood sample has been key in high throughput analysis of components within blood. Of these instruments, flow cytometers have been responsible for accurately presenting blood cell counts for millions of patient samples. We will discuss these instruments in detail later. In parallel with their use for clinicians however, researchers have relied on the high throughput and accurate interrogative abilities of flow cytometers for research in detecting a host of pathogens including microbial agents and circulating tumor cells.[4–6] To have the capabilities of the latter, flow cytometry research has spurred the development of complex, versatile, micro-scale beads for biological sample interrogation.[7] In parallel with research in the development of assay components, flow chamber design has also grown in complexity. Flow chambers are the component of a flow cytometer that focus the sample components into discrete geometric regions for optical interrogation and analysis. More recent flow cytometry technologies integrate acoustics to replace traditional hydrodynamics for media focusing in flow chambers, a method that focuses particles based on their physical properties. Using semiconductor fabrication methods plays an important role in the construction of acoustic flow chambers for flow cytometry.

As an extension of these technologies, point of care devices are critical to rapid diagnosis in remote, less developed areas, large-scale hospitals, and in urban homes.[2] These devices allow hospitalists to take small amounts of patient sample, at the bedside or at home, and quickly obtain information that allows for early stage diagnosis and treatment of various ailments such as glucose levels, cardiac markers and pathogenic microbes.[2] Detecting viruses and pathogenic microbes at early onset of infection is critical in treatment for these diseases. Many of these technologies utilize microfluidics and fluorescent detection for diagnosis, but are limited in how many analytes they can detect at a single time.[2] Integrating multiple analyte detection schemes into a single device is a key technical challenge to overcome. The approach of detecting multiple analytes in a single platform is known as multiplexing. Developing microparticles with functionalized surfaces is a promising path to integrate multiplexing into point of care platforms.[8] Furthering advancements in biomedical technologies through the integration and use of acoustics and microparticle platforms is a potential contributor to the advancement of rapid, lower cost, early stage diagnosis for treatment.

Acoustics, in synergy with droplet technologies, also has potential for biomedical devices that can improve patient care and outcome. More recent methods of droplet synthesis and manipulation have integrated acoustic technologies. In the latter part of the 2000’s research was spurred in the field of droplet microfluidics.[9] Scientists developed micro-scale methods of generating monodisperse water droplets. Generating size-controlled volumes of a fluid is useful for the food industry, synthesis of drug tablets, bio-medicines or for three-dimensional hydrogels for cell culturing. Loading cells into microgels is a technology that holds promise for 3D printing of tissues and organs in the near future. These microgel cell cultures also hold promise for drug discovery lab studies. Most droplet systems are currently limited to generating these monodisperse drops using a water-oil emulsion. Water-in-oil emulsions lead to issues where researches need to administer water soluble nutrients and drugs to the cells encapsulated in these aqueous droplets and in denaturing of biological components that meet the oil/water interface.[10] Generating water-in-water droplets in these devices for biomedical application is a key challenge, and acoustics have excellent potential as an enabling technology.

1.2 Acoustofluidics

1.2.1 Primary acoustic radiation force

Acoustofluidics is defined by the principles of acoustophoresis and microfluidics in a single system. Acoustophoresis is the movement of a particle using sound waves.[11] The first observation of the phenomenon of manipulating particles with sound waves is credited to Kundt in 1868, who reported the concentration of dust in a cylindrical tube (Kundt's tube) acted upon by an acoustic standing wave.[12,13] The movement and position of a particle due to the acoustic standing wave is determined by the magnitude of the acoustic forces acting on the particle. From Kundt's initial published observations, the primary acoustic force has been derived for a spherical particle by L. P. Gorkov.[14] Gorkov's equations describe how the magnitude of the force (*F*) scales proportionally with the frequency (c/λ) of the acoustic energy, the pressure within the system (*P*), the size, or volume, of the particle (V_p) and its position (*x*) relative to the force (Equation 1.1). The second key factor in determining the magnitude of the acoustic force describes the relationship of the particle's physical properties, i.e. density and compressibility (ρ_p, β_p respectively) and those of the fluid medium (ρ_m, β_m).[15]

$$F = -\frac{(\pi P^2 V_p \beta_m)}{2\lambda} \phi(\beta,\rho) \sin 2kx \qquad \text{Equation 1.1}$$

where,

$$\phi(\beta,\rho) = \frac{5\rho_p - 2\rho_m}{2\rho_p + \rho_m} - \frac{\beta_p}{\beta_m}$$

The second term in this equation [$\phi(\beta,\rho)$], is the acoustic contrast factor. This term determines whether the particle(s) will migrate to the pressure node or pressure antinode of an acoustic standing wave. For a single node system, a negative value of the acoustic contrast factor means the particles will migrate to the antinodes, near the edges of a channel for a half-wave system (λ/2). A positive acoustic contrast factor means the particle will migrate to the node of the system, in the center of a chamber with a half-wave, where the reflecting wave overlaps. Biological solutions contain particles that exhibit both positive and negative acoustic contrast in water as seen in **Figure 1.1**.

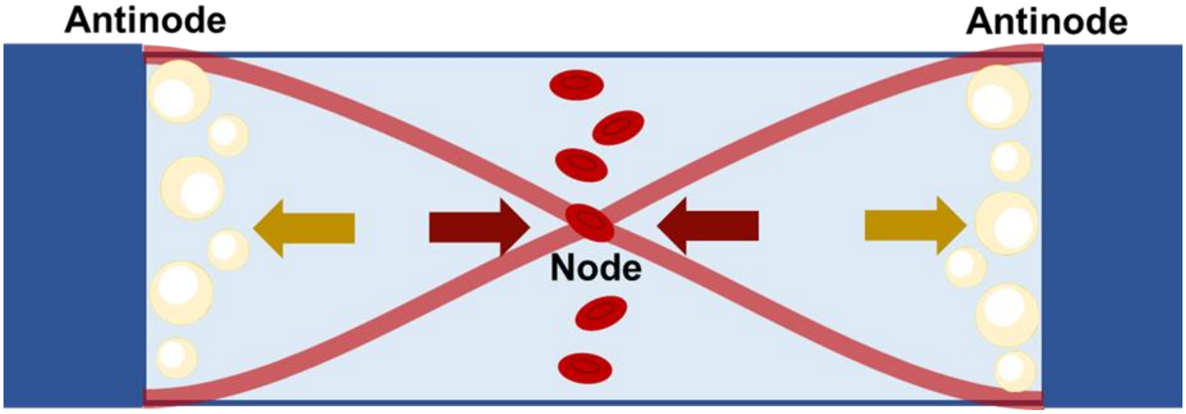

Figure 1.1. Particle positioning based on the acoustic contrast factor. Illustration of rectangular channel with a single node (half-wave) system (red), two antinodes, and arrows denoting the movement of specific acoustic contrast particles. Red blood cells, exhibiting a positive acoustic contrast factor, move to the node and lipid particles, exhibiting negative contrast, move to the antinodes.[11]

1.2.2 Microfluidic acoustic resonance

The position of particles acted on by the primary acoustic radiation force are determined by the acoustic standing wave. An acoustic standing wave is an oscillating wave generated by sound whose amplitude does not change in a confined geometric space.[16] For the topics herein, the standing wave is generated from the applied acoustic force radiating from the bulk surrounding material and reflecting off the opposite wall of acoustic energy propagation. The overlapping of the acoustic wave creates distinct pressure regions where the acoustic field forms a pressure node and pressure antinodes. When a harmonic is created (constructive interference between the incident and reflected wave) the result is a standing wave in the channel as depicted in **Figure 1.2.**[17] The chamber confining the standing wave is filled with a fluid medium. For this dissertation we define water as the fluid and designate the speed of sound that propagates through it as ~1490 m/s at room temperature. An acoustofluidic chamber material with high acoustic impedance will reflect most of the acoustic energy, while a low impedance material will absorb it. As an aside, low acoustic impedance materials are still useful for devices where a standing surface acoustic wave is desired. Standing surface acoustic wave technologies, or SSAWs, behave similarly to bulk acoustic standing wave systems (BAWs) but generally require complex sets of electrodes or wave guides in addition to the low acoustic impedance material, such as polydimethylsiloxane (PDMS), to construct. BAWs are simpler to construct, requiring only a piezoelectric transducer source that directly attaches to the high impedance material causing the entire device to resonate acoustic energy.

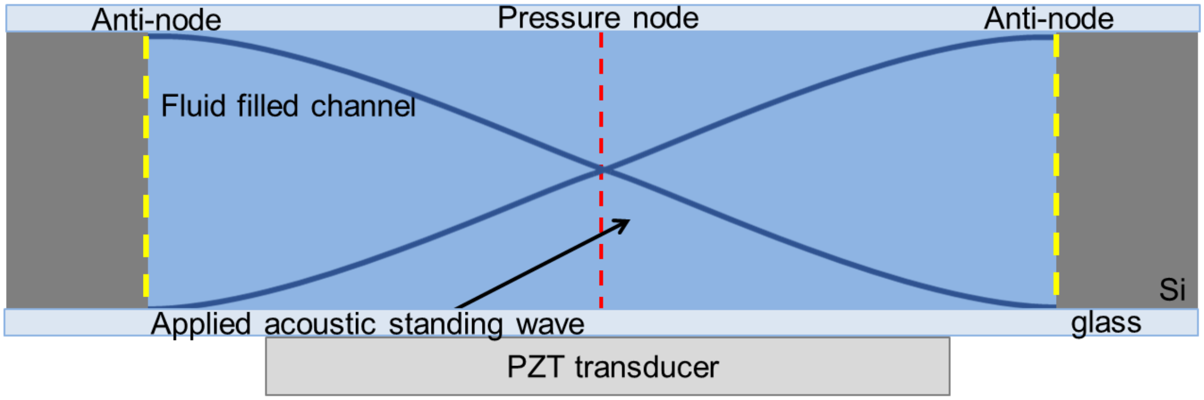

Figure 1.2. Acoustic standing wave in BAW device. Illustration of an acoustic standing wave is depicted within a high acoustic impedance material, silicon with glass caps (similar impedance values). The standing wave is generated from the surrounding materials resonance i.e. a bulk acoustic standing wave. The fluid filled channel illustrates that for a single half-wave resonance, a single pressure node is generated in the device and two pressure anti-nodes are generated at the channel walls.

Adjusting the frequency of the acoustic field, the fluid media that the sound wave travels though (affecting the speed of sound), or the channel dimensions, modulates the number of nodes present within a fluidic chamber. The expression in Equation 1.2 can be used to determine the number of nodes present within an acoustic chamber (*N*).

$$N = \frac{2lv}{C} \qquad \text{Equation 1.2}$$

Here, (*l*) is the width of the chamber, (υ) is the applied acoustic frequency, and (*C*) is the speed of sound in the fluid medium. A multi-node system is depicted schematically in **Figure 1.3**. This equation is important for designing the dimensions of acoustic focusing microfluidic flow chambers especially when engineering multiple-node configurations.[18]

For a BAW device, a piezoelectric transducer is attached directly to the channel material to generate resonance in the entire structure. Piezoelectric materials are crystalline structures that generate an acoustic force in the form of mechanical vibration after an alternating current electric field is applied. Conversely, these materials can generate an electrical current if a mechanical stress is applied to the transducer. An example of a common piezoelectric is a spark ignition integrated into most household grillers. The button pressed to generate an ignition in the grill, forces a mechanical impact to the piezoelectric crystal resulting in an electrical spark.

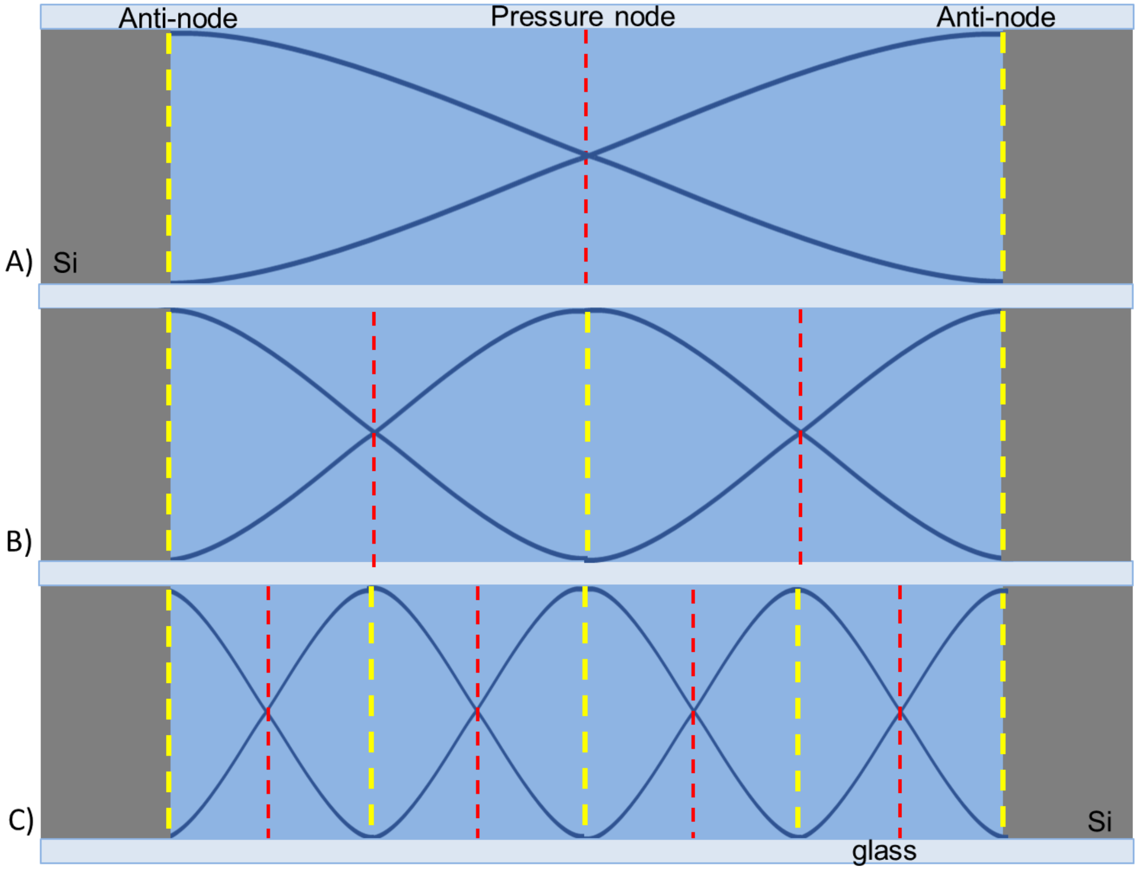

Figure 1.3 Multiple acoustic standing waves. (A) sinusoidal single-node (red dashed lines) standing wave system of a rectangular silicon flow chamber with two anti-node regions (yellow dashed lines). (B) two-node standing wave system in the same rectangular silicon flow chamber (C) four-node standing wave system in the same rectangular silicon flow chamber. As discussed, using Equation 1.2 allows a user to control how many nodes in a chamber they desire by adjusting the applied frequency to a transducer. For this illustration, the channel dimensions and fluid medium are fixed so frequency is the only parameter adjusted to generate multiple nodes.

1.2.3 Secondary acoustic radiation force

In addition to primary acoustic radiation forces acting on particles, secondary acoustic forces also explain particle behavior within an acoustofluidic chamber. It has been shown that acoustophoresis can be used to focus particles in microfluidic devices for various applications including lab on chip platforms. One of the earliest examples in the literature is by Yasuda et al. where their group focused red blood cells in a device and collected the concentrated downstream sample.[17,19] Red blood cells exhibit a positive acoustic contrast factor and therefore focus to the single node of their device. As microfluidic technologies sought to focus and separate different components in a biological sample, the interest in focusing small biological particles like bacteria arose. Microfluidic systems offer higher throughput and precision analytics capabilities when compared to culturing which can take up to 5 days to determine microbial species for certain cultures.[20–23] Small particles however, particularly those below 1µm in diameter, are notoriously difficult to acoustically focus.[23] As discussed previously, the primary acoustic force scales with the size of the particle and as the particle decreases in size, so does the magnitude of the primary acoustic force. This results in secondary forces becoming predominant and small particle samples undergo what is known as acoustic streaming.[24] Acoustic streaming is when acoustic boundary layer effects cause dissipation of the acoustic energy which results in a flow vortex near the, in our case, channel walls, a phenomena also called Rayleigh streaming.[24,25] The secondary acoustic radiation force is the primary factor responsible for acoustic streaming and has been derived by Bjerknes (Equation 1.3).[26–28]

$$F_s = 4\pi a^6 \left[\frac{(\rho_c-\rho_w)^2(3cos^2\theta-1)}{6\rho_w d^4}\right] v^2(x) - \frac{\omega^2 p_w(\beta_c-\beta_w)^2}{9d^2} p^2(x) \qquad \text{Equation 1.3}$$

Many of the terms in the secondary acoustic radiation force equation also appear in the primary acoustic radiation force (Equation 1.1). The terms represent the pressure *p(x)* of the acoustic wave, the velocity *v(x)* of the acoustic wave, the particle radius *a*, the angle between the intercepted acoustic wave and the direction of propagation *Θ*, and the distance between particles *d* in addition to the terms previously defined. One of the important contributing factors between the primary and secondary acoustic radiation force is the dependence on interparticle spacing (*d*). The secondary acoustic radiation force causes particles to migrate toward each other as an attractive force depending on the angle of acoustic wave propagation. This attraction increases in magnitude due to the inverse proportion of the interparticle spacing to the force. As the concentration of small particles increases, the inter particle distance decreases thus resulting in higher magnitude of the secondary acoustic radiation force. Due to the diminishing effects of the primary acoustic force as a direct correlation to size, secondary forces become predominant. Enrichment of sub-micron biological particles such as bacteria and microspheres for affinity capture both use the principles of secondary forces to spatially separate sample components in acoustofluidic devices.[29–31]

Integrating acoustophoresis technology with microfluidics allows for precise methods to be employed where biological sample component separation, enrichment, and analysis are desired. Acoustophoretic devices can be expanded from lab on chip applications to modern instrumentation platforms. Coupling acoustic technologies with flow cytometry allows for higher throughput, precision, and sorting capabilities. Manipulating particles with acoustophoresis has proven to be a gentle, non-contact method for biological media manipulation in developing state-of-the-art flow cytometry.

1.3 Microfluidic flow chambers for flow cytometry

1.3.1 Overview and sample focusing methods

Flow Cytometry is a modern expanding field in high throughput diagnostics and cellular analysis with integrated microfluidics. Flow cytometry is best described as a type of single cell analysis where large fluid sample sizes can be rapidly interrogated for qualitative and quantitative characterization.[4] One of the main advantages of using flow cytometry is that it has the capability to rapidly characterize multiple parameters simultaneously on single cells in a suspension.[6,32] These instruments have this capability through specialized optics to characterize how incident light is scattered off particles or to measure the intensity of various fluorescence signals.[4,6,32] The scatter detection capabilities allow the user to obtain physical properties such as size and cellular component density, whereas the fluorescence signaling enables information on particular components that can be dyed or labeled such as DNA, antigens, antibodies, or tumor cell markers.[33,34]

The general setup of a flow cytometer can be broken down into three main components, the optics and light source, the image/data collection scheme, and the flow chamber.[4] **Figure 1.4** schematically illustrates the main components of a flow cytometry instrument. This dissertation work focuses on the flow chamber component, sometimes referred to as a flow cell, and we will therefore describe only this component in detail.

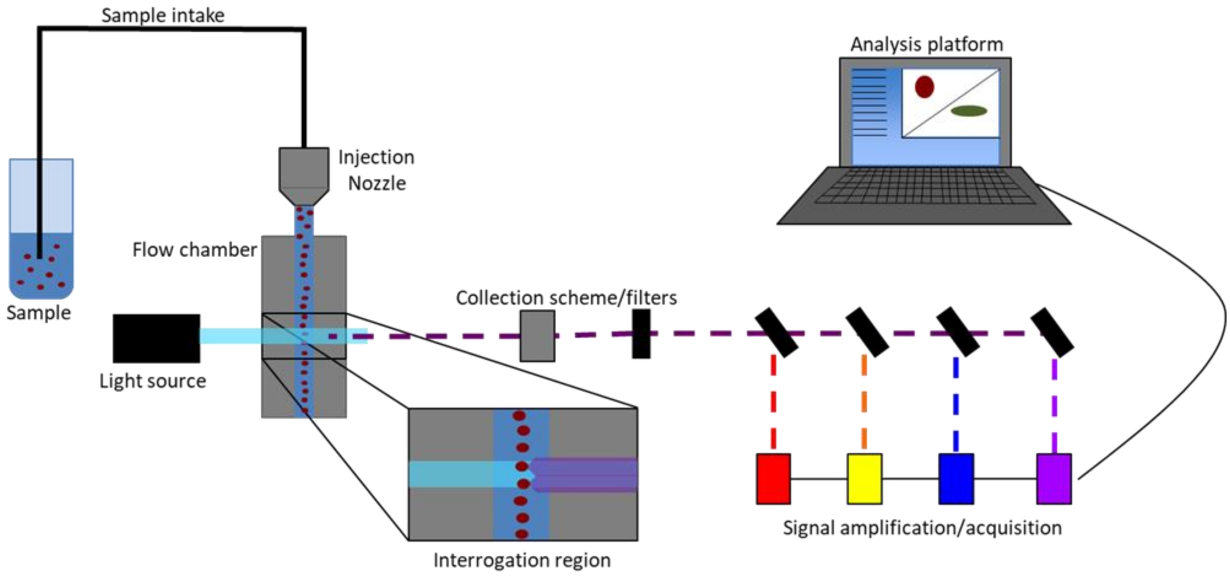

Figure 1.4. Schematic of a typical flow cytometry system. Sample fluid is aspirated into the intake and subsequently flowed through an injection nozzle where it is acoustically or hydrodynamically focused by a fluid sheath. The focused sample media then flows past the interrogation region where a laser light source excites and transmits through the sample followed by optical collection from detectors. The signal can then be split and amplified for downstream analysis.

Conventional flow cytometry focuses a sample's particles in the flow chamber through hydrodynamic focusing. Hydrodynamic focusing employs of a co-flowing fluid sheath to create a barrier that confines the sample fluid. The sheath is flowed at a higher velocity on either side of a "1-dimensional" flow chamber; coined by microfluidic systems studies.[4,35] This "1D" focusing creates vertical pressure boundaries on either side of a sample stream so that the particles can pass single file through the region of interest (ROI) where a laser can fluorescently excite and scatter off the particles within the sample stream. **Figure 1.5** illustrates a typical Y-channel flow chamber with 1D vertical focusing. Using microfluidic flow chambers for flow cytometry allow the fluids to flow in the chamber at laminar flow velocities which prevents mixing of the sample and sheath fluids. Laminar flow is a fluidic flow state commonly observed in microfluidics where fluid layers slide against each other in parallel layers like sheets.[36] This is a characteristic flow regime for microfluidics since the fluids typically exhibit a low Reynold's number.[36,37]

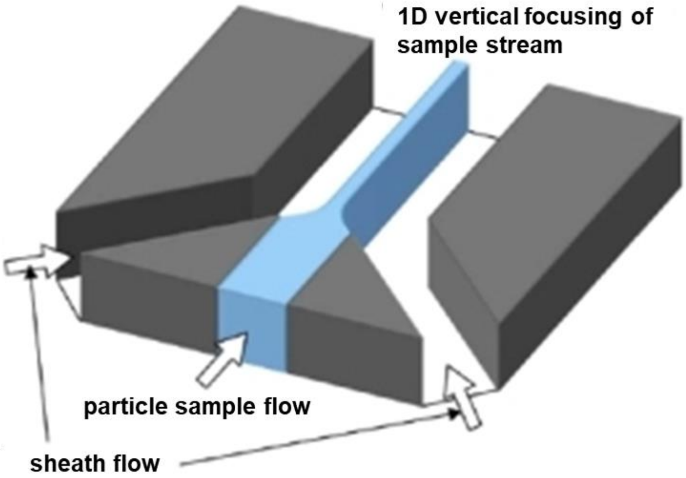

Figure 1.5. 1D hydrodynamic focusing in y-channel flow chamber. Illustration of typical Y-channel hydrodynamic focusing where two sheath fluid inlets intersect with a single sample stream resulting in vertical "1D" focusing (image modified from Derveaux et al., Synergism between particle-based multiplexing and microfluidics technologies may bring diagnostics closer to the patient).[35]

Hydrodynamic focusing has been shown to enable processing of tens of thousands of particles per second in conventional flow cytometry.[4,38] Some of the limitations of hydrodynamic focusing include undesired shear at the interface of the sheath and sample streams as well as limited rates of flow and volumetric throughput of the sample.[18,39] For example, biological cells at the sheath-sample interface may exhibit shear stresses that can damage or rupture cell membranes.[40] More modern techniques of sample fluid focusing have been introduced to lower the limitations of hydrodynamic focusing or replace it as a method to focus sample solutions.[41] Some of these methods include inertial flow focusing, dielectrophoresis, optical traps, and acoustic focusing.[4,38,39]

Acoustic focusing of particles in microfluidic flow chambers is another key method that obviates the need of fluidic sheath flow for sample focusing. In addition to the benefits of focusing without a sheath fluid, acoustophoresis has proven to be a gentle method for biological cell manipulation. Like hydrodynamic flow chambers, acoustic flow chambers can be constructed using conventional fabrication methods but require only a simple single channel design in contrast to the y-channel flow chambers commonly used for hydrodynamic focusing. Constructing specialized microfluidic flow chambers for flow cytometry utilize many of the same microfabrication techniques used in other micro electrical mechanical systems (MEMS) as in the semiconductor industry.

1.3.2 Flow chamber fabrication techniques

Microfluidic flow chambers used in flow cytometry are fabricated using a host of different methods and various materials.[6,42,43] Many commercial flow chambers are made of plastic from molds and are disposable, single-use devices.[44] Some flow chambers are fabricated through laser etching channels into a glass substrate material.[45,46] Other microfluidic devices are fabricated from photolithography molds and polydimethylsiloxane (PDMS) which is poured over a mold, cured, then peeled off and bonded to a glass slide via plasma-activated bonding techniques.[42] This method proves useful as a low-cost method to make the mold, which can be reused for multiple devices.[47] PDMS is an inexpensive silicone material that uses no harsh chemical substances or processes to cure into a rubbery, gel-like polymer.[48] As mentioned previously, this material is ideal for SSAW acoustofluidic devices because it exhibits higher acoustic attenuation and lower impedance as a material.[49]

MEMS methods alluded to at the end of the previous section are silicon chip microprocessing techniques that etch channels into silicon wafer substrates.[50] As these methods use multiple instruments and cleanroom procedures, it often involves the use of expensive equipment, but provides a robust, precise method to fabricate flow chambers. For the topics covered within this dissertation we will discuss the processes relevant to silicon MEMS device processing.

The process of making these devices begins by designing the flow chamber pattern for a soft lithography photomask using computer aided drafting. Soft lithography was introduced in the 1990's to lessen the expensive and lengthy requirements for semiconductor chip fabrication. Soft lithography allows for rapid prototyping for polymer designs on different substrate materials.[51] The pattern is printed onto a substrate, quartz or lime glass for industrial photolithography or a transparency material for more inexpensive techniques. A positive or negative photoresist (PR) polymer material is uniformly distributed over the surface of a substrate material like a silicon wafer. Positive photoresist is a polymer material that crosslinks in the presence of heat and can have its bonds scissioned/weakened when exposed to high energy ultra violet light. The exposed regions allow a developer solvent to remove the exposed pattern for further device processing.[52] By contrast, negative photoresist requires exposure to high energy ultra violet light to initiate crosslinking of the polymer, creating a more resistant surface during solvation development.[52] After the negative resist pattern is exposed, the wafer is developed in a solvent that removes the unexposed regions leaving a mold on the substrate surface as depicted schematically in **Figure 1.6**.

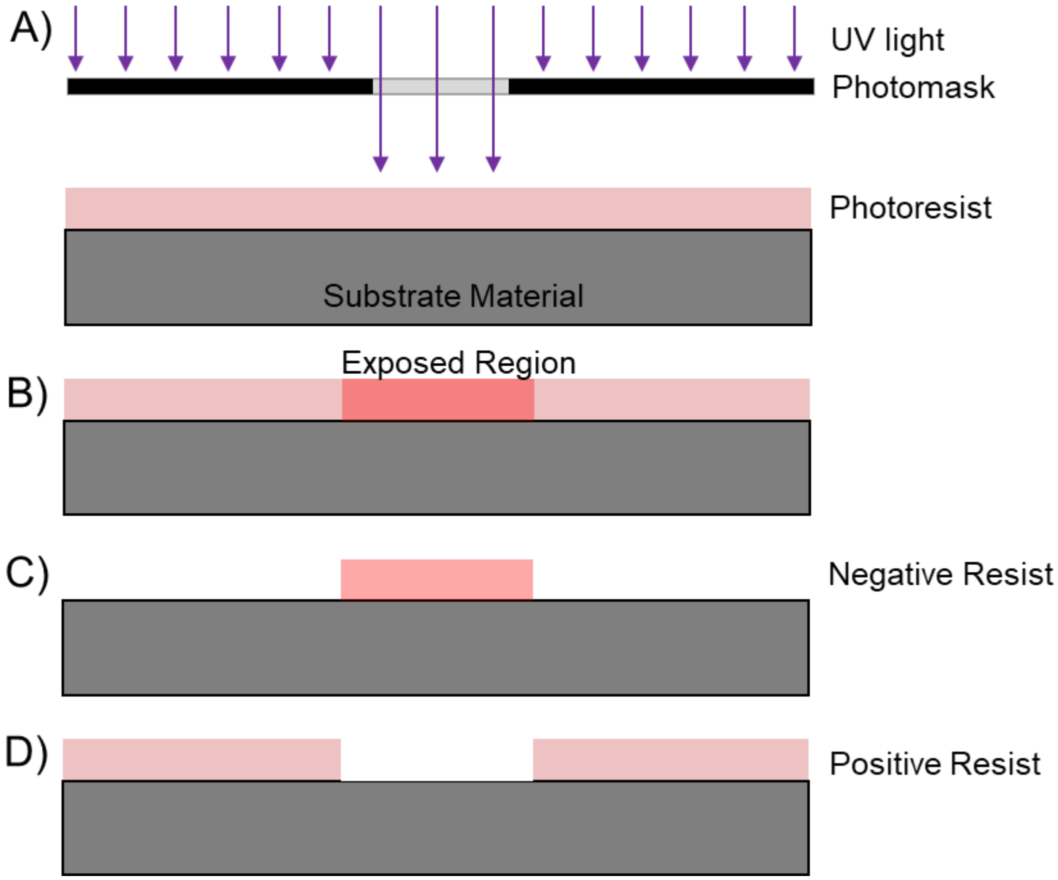

Figure 1.6. Soft lithography using negative and positive photoresist. (A) during exposure for soft lithography, a photomask transmits the high energy UV light specific to the pattern onto the photoresist covered surface of a substrate material. (B) The exposed sample is then baked for negative resist and developed using the specified developer solvent (C) leaving only the exposed pattern. (D) prior to exposure, the photoresist is baked for crosslinking, then developed after exposure and scission of the positive resist leaving only the unexposed regions of the photomask pattern.

Soft lithography is an ideal method for PDMS microfluidic devices. Fabricating PDMS-glass flow chambers for hydrodynamic focusing or for SSAW devices has proven to be a simple, robust, low-cost process. Soft lithography with negative photoresist allows the user to generate reusable micropattern molds for rapid PDMS device fabrication. Most photolithography processes are limited by the resolution of the UV exposure instrument and the photomask itself. For most research purposes involving microfluidic device fabrication, super high resolution (e.g. less than 10 micron features) is not required, thereby allowing the use of a photomask transparency. After the device pattern is formed with negative resist on a wafer, a 10:1 ratio of the PDMS pre-polymer to curing agent is mixed and poured over the mold and placed in ~60 ^{o}C oven to cure. Once cured, the PDMS is pulled off the micropattern mold and bonded to a glass slide via plasma-activated bonding. A plasma cleaner generates oxygen radicals that activate glass and PDMS surface reactivity, which can then be pressed together under moderate pressure to create a tight seal between the two surfaces.[53] The resulting device is a microchannel comprising PDMS capped with a glass slide.

There are two primary methods we employ for processing of silicon devices following lithography patterning. Lithography results in micropatterned regions on a silicon substrate material, as depicted in **Figure 1.6**. The first method discussed regarding etching a channel into a silicon substrate for microfluidics is wet etching. Wet etching is an inexpensive etch process of solid crystalline substrates in a chemical solution.[54] This process works selectively for silicon oxide (silica) or silicon surfaces depending on the chemical etchant. Prior to etching, a layer of oxide (SiO_2) or nitride (SiN_3) is required as a protective layer from KOH etching (**Figure 1.7 A**). After lithography, the patterned substrate is immersed in a buffered solvent such as hydrofluoric acid (HF) to remove the oxide/nitride (sacrificial) layer on the patterned surface (**Figure 1.7 B**).[54-56] The buffered oxide etch is followed by removal of the PR polymer using organic solvents and/or ashing (**Figure 1.7 C**).[54-56] Potassium hydroxide (KOH) is used to etch the exposed silicon surface (**Figure 1.7 D**).[54–56]

Following KOH etching, the remainder of the sacrificial layer is once again removed using the buffered oxide etch. The wet etching process can take up to several minutes depending on the desired depth of the channel. The resulting pattern is an isotropic profile, or equal etch in all directions (**Figure 1.7 E**). An anisotropic profile can be achieved with wet etching when different substrate layers, inert to the chemical etchants, are exposed.[57] An anisotropic profile is when the direction of the etching is not equal in all directions, generally resulting in a more rectangular profile.

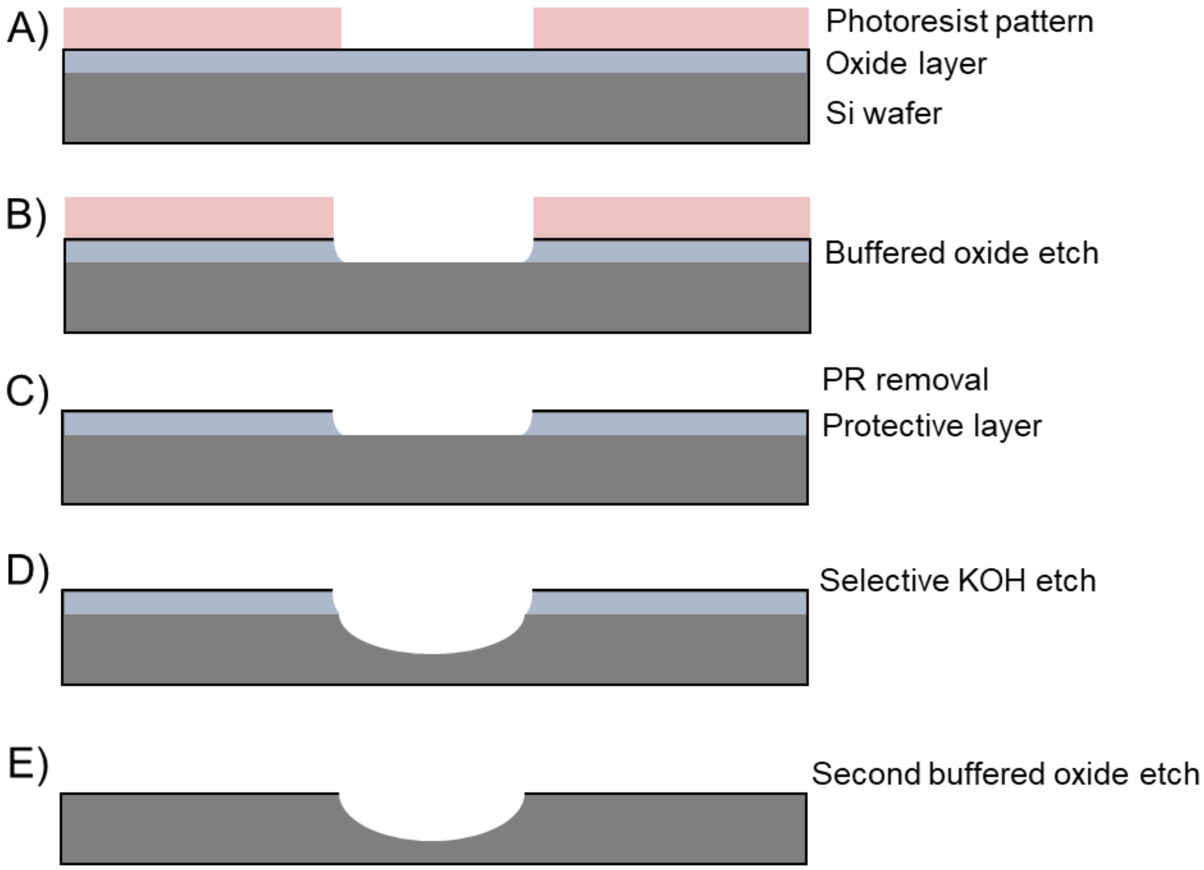

Figure 1.7. Wet etch process. (A) An oxide layer is grown (blue) to desired etch depth via thermal oxidation prior to soft lithography. (B) the oxide layer is etched using a buffered oxide etch, e.g. HF and buffering agent, leaving an isotropic profile with overhang of the chemically resistant photoresist. (C) Photoresist is removed using solvating agents. (D) The exposed surface, following buffered oxide etch, is etched with KOH isotropically. (E) Following desired etch depth, the remaining oxide layer is removed with an additional buffered oxide etch.

For a more direct approach to etching an anisotropic channel in silicon, reactive ion etching (RIE) or deep reactive ion etching (DRIE) via the Bosch process can be employed. The Bosch process is named after the German company Robert Bosch GmbH which developed and patented this silicon processing method.[58,59] This method of anisotropically etching silicon cycles between two phases in a reactive ion etcher or deep reactive ion etcher. The first phase bombards the surface of the substrate, in the presented case silicon, with heavy ionized particles typically Sulfur hexafluoride (SF_6) in an isotropic manner (**Figure 1.8 A, B**). The second phase involves the deposition of a passivation (or chemically inactive) layer, Octafluorocyclobutane (C_4F_6) which coats the silicon walls and comes off as poly(tetrafluoroethylene) or Teflon (**Figure 1.8 C, D**).[58,59] Each phase results in its own isotropic etch but due to the addition of the passivation layer which coats the side walls and the repeated orthogonal ion bombardment, the overall profile becomes anisotropic (**Figure 1.8 E**). To achieve less of a scalloped side-wall profile, each phase in the process can be changed to have a shorter or longer etch time, depending on the desired depth of etch. Further processing to smooth off the scallops includes thermal oxidation of a small depth and a buffered oxide etch to remove the oxidized layer.

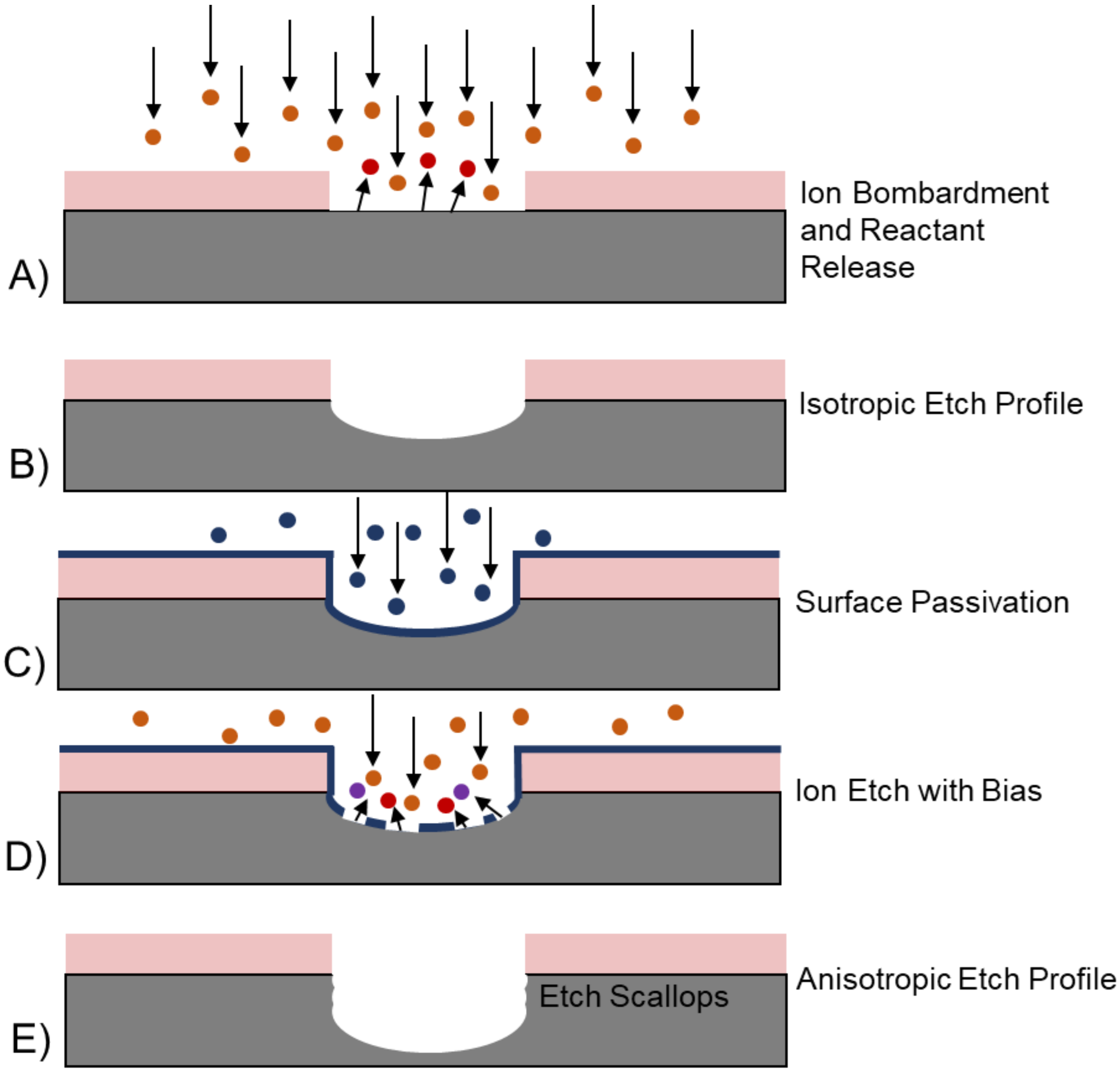

Figure 1.8. DRIE Bosch process. (A) SF_6 ions (orange) bombard the surface orthogonally to the bare silicon surface and the silicon-SF_6 reactants (red) are volatilized. (B) each etch step in the process leaves a shallow isotropic profile. (C) C_4F_6 (blue) is then added as a passivating polymer over the surface of the device. D) the surface passivation step is followed by another SF_6 etch step reacting with the C_4F_6 (violet) and then the exposed silicon surface (red). (E) These steps are done in succession until the desired depth is achieved resulting in an anisotropic profile with scalloped side walls.

The etched silicon wafer devices are diced to a desired size and cleaned by submersion in an organic solvent to remove the polymerized positive resist. To further clean the silicon device surface, a plasma asher can be used to burn off excess resist. After ashing, the devices are further cleaned with piranha solution to remove any residual polymer resist. Piranha solution is a 70:30 mixture of sulfuric acid (H_2SO_4) to hydrogen peroxide (H_2O_2) which is commonly used to remove organic compounds from surfaces.[60] At this stage the device can be capped with glass slides to seal the chamber for microfluidics. Anodic bonding is a high temperature (500 ^oC) process that allows glass to be bonded to a hydrophobic or hydrophilic surface by causing sodium ions to diffuse out of amorphous glass to a cathodic interface.[61] A high voltage of around 300 V causes singlet oxygen ions to bond directly from the glass to the silicon on the exposed surface of the etched device creating permanent SiO_2 bonded interface with the silicon substrate as seen in **Figure 1.9**. The glass slide can have inlet/outlet ports for fluidics drilled or otherwise created prior to bonding.

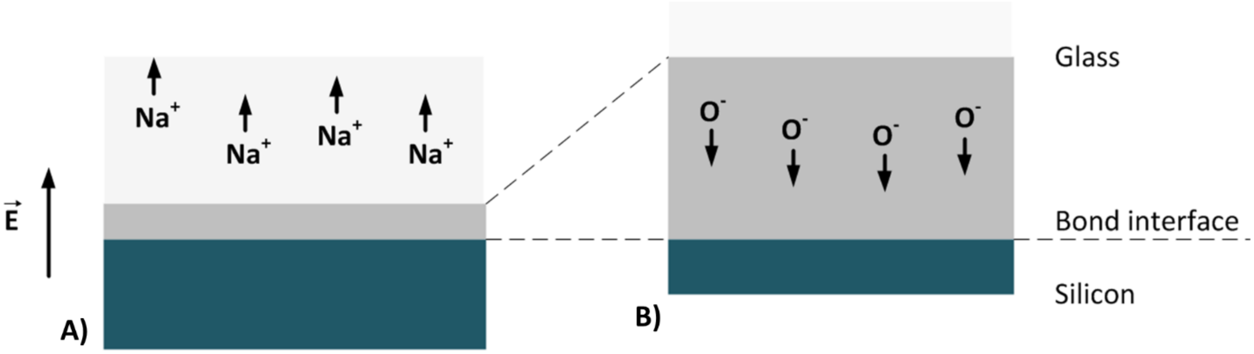

Figure 1.9. Anodic bonding. A) Sodium ions move with the electric field through the glass B) Oxygen ions move to the silicon surface creating SiO_2 bonds with the wafer substrate. (Figure modified from Mack, S., "A comparative investigation of physico-chemical processes at the boundary layer of directly and anodically bonded solids").[62]

In addition to MEMS device processing for microfluidics, a low-cost alternate method for three-dimensional geometry flow devices can be constructed. Glass microcapillary devices provide a low cost and rapid method of fabricating droplet generating microfluidic devices. This microfluidic device is considered 3D because dimnsions of the channels vary radially. As seen in **Figure 1.10**, a typical microcapillary microfluidic device has three primary components; an injection capillary, a collection capillary, and an outer housing capillary. The injection capillary delivers an inner phase fluid that flows at a lower flow rate than an outer phase fluid delivered from the outer capillary housing. While these devices are typically not used for flow cytometry they do serve as ideal devices for droplet synthesis.

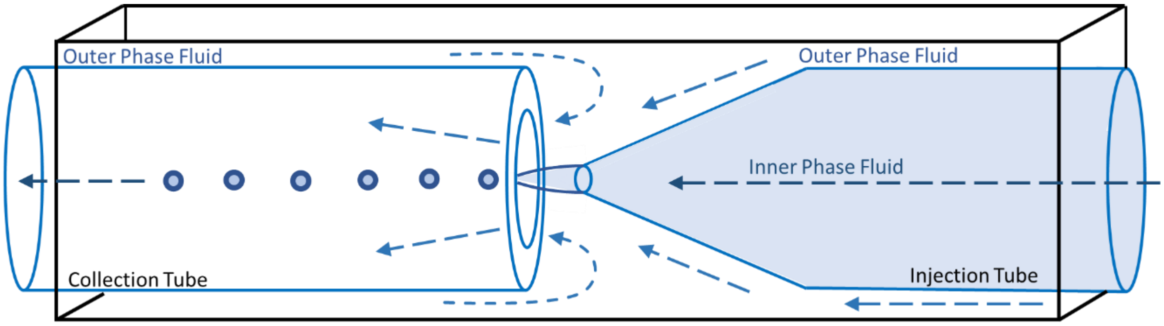

Figure 1.10. Microcapillary device. A schematic of a typical microcapillary microfluidic device where an injection capillary tube delivers an inner phase fluid which is hydrodynamically focused by the outer phase fluid entering from the surrounding square capillary volume. The shear forces of the faster moving outer phase will cause micro drops to be formed from the slower moving inner phase if there is enough interfacial tension between the two fluidic states.

A group out of Loughborough University used a glass capillary device to synthesize oil in water and water in oil monodispersed polymer microparticles which serve as a scaffold for particles used in biotechnological or pharmaceutical applications.[63] Kim and coworkers from Harvard used a glass microcapillary device for double emulsion droplet synthesis.[64] Their method involved injecting an emulsified dispersed (inner) fluid phase into an aqueous continuous (outer) phase which resulted in the synthesis of an oil outer shell encapsulating an aqueous core. The same group used this method to encapsulate various cargo illustrating the robust characteristics of microcapillary synthesized emulsion microdropets.[65] These devices are not limited to oil in water emulsions but do require fluids with a high interfacial tension or an external physical force for low interfacial tension systems to generate droplets. We will discuss this in further detail in section 1.4 of this chapter. While these devices have limited capability in their modular design compared to MEMS fabricated devices, their low-cost, ease of construction, and role in droplet synthesis is unmatched. Chapter 7 of this dissertation details our approach for deployment of acoustic-enabled glass capillary devices for aqueous two-phase systems for cell encapsulating hydrogels.

1.3.2 Biological applications for acoustic flow chambers

As mentioned previously, silicon-based microfluidic devices are an ideal material for acoustofluidic devices. The high acoustic impedance of silicon (19.79 x 10^6) kg m^{-2} s, compared to PDMS (1.04 x 10^6) kg m^{-2} s, means that a large amount of resonating acoustic wave energy is conserved after reflecting off the channel walls.[66] In addition to the impedance value of silicon, the capability to etch vertical channel walls is attractive for acoustophoresis applications.[66] Capping these etched channels with a borosilicate glass slide via anodic bonding allows the user to image clearly into the channel for particle analysis.

Piyasena et al. from the University of New Mexico used these MEMS fabrication methods for silicon based microfluidic flow chambers for wide-channel parallel acoustic flow cytometry.[67] The work described how acoustofluidic flow chambers can be designed to generate multiple parallel streams that focus positive acoustic contrast particles. An instrument was later developed by Kalb et al. around the principles of parallel stream acoustic flow cytometry.[68] One postulate asserts that an etched flow chamber with an opaque bottom may trap light from an incident laser beam (used for particle stream interrogation). This absorbance of light energy may lead to the generation of heat in silicon flow chambers, which can disrupt the microfluidic laminar flow profiles. This light absorbing characteristic of etched silicon structures is widely used for solar cell semiconductor materials.[69,70] As excess heat is not desired for microfluidic devices, this motivates further iterations of the flow chamber which can be made to be optically transparent, reducing the excess heat generated from light absorption.

As discussed previously, different biological particles exhibit a positive or negative acoustic contrast factor depending on their relative density and compressibility compared to the surrounding fluid medium. Grenvall et al. developed an acoustophoretic device at Lund University that separated white blood cells from other cells due to their dissimilar acoustic contrast.[71] The microfluidic device separates biological components to five different outlets using size-based flow characteristics in conjunction with their acoustic contrast properties. The group also used acoustophoresis to separate lipids from proteins in milk using the same methods since lipids exhibit negative acoustic contrast.[72] The flow chamber designs allow the separated solution components to be collected separately for analysis or further studies.

Developing affinity capture microparticles that exhibit negative acoustic contrast (NAC) has been achieved from Cushing et al. at the University of New Mexico.[73] The NAC particles were synthesized using an emulsion technique with PDMS in an aqueous surfactant solution. The group describes a simple process to biofunctionalize the surface of the NAC particles that can be used for affinity capture of antigens in solution with dilute blood. The NAC particles separate to the anti-node regions of the device while the red blood cells in solution focus to the single pressure node region and are filtered out of solution. The NAC particles are then collected after the acoustic field is turned off and analyzed with flow cytometry. Chapter 6 of this dissertation improves upon the concepts developed by this work in order to provide basis for a handheld lab in a syringe assay.

1.4 Acoustofluidics for hydrogel microsphere synthesis

1.4.1 Cell encapsulation and acoustic droplet generation studies

Soft materials are characterized by energy levels around room temperature kT, and can be easily altered or deformed by small physical or thermal fluctuations.[74] The study of liquids polymers, gels and biological materials all fall under this category. Hydrogel synthesis for cell culturing studies is of current interest in soft materials science. Three-dimensional hydrogel synthesis has proven to be a robust method for cell culture and has great promise for 3D tissue printing platforms. Many of the synthetic strategies in the literature involve microfluidic processes of oil-in water emulsion. Workman et al. from Cardiff University published a method for immortalizing human cells in alginate hydrogels.[75] Their work involves a microfluidic chip with a T-junction that pinches off an alginate solution into monodispersed droplets containing human cells. The alginate aqueous phase forms droplets in a co-flowing sunflower seed oil. Faulkner-Jones et al. out of Heriot-Watt University illustrated bio-printing of alginate drops with stem cells that were controllably differentiated into liver tissue. Their group uses alginate as the printer ink that is crosslinked by a co-flowing calcium solution.[76] Sodium alginate is a biocompatible polysaccharide polymer extracted from brown seaweed algae commonly used as a biocompatible gelling material. The three-dimensional structure of alginate hydrogels recapitulates the native extra cellular matrix environment for cells to differentiate into and have proven to be ideal for stem cell proliferation and growth.[77]

Within the last decade, researchers have integrated acoustics for droplet generation. Some of these constructs integrating acoustics span from single cell capture into monodisperse droplets to subpicoliter droplet generation using integrated PZT transducers.[78,79] One key study incorporated an acoustically generated cell encapsulation and patterning construct. Fang et al. out of the University of Michigan use acoustic droplet ejection and the principles of aqueous two-phase systems for automated cell patterning.[80] The group constructed a device that ejects cell laden dextran (DEX) droplets onto a destination plate suspended above the PDMS source plate where the patterned DEX drops are collected and immersed in a polyethylene glycol (PEG) solution for culturing. The PEG solution then had a second cell type added which did not diffuse into the DEX droplet phase. The resulting fluorescent cell patterns were striking, illustrating the precision and capability of their cell patterning method. ATPS will be discussed in greater detail in the following section.

Water-in-air and water-in-oil systems are convenient platforms to generate droplets but have some limitations. Delivering water soluble drugs or nutrients to study cell behavior is limited for these systems. Organic solvents and oils can degrade or denature certain water-soluble biological components, which are better suited to exist in aqueous native-like solutions. Additionally, the oil of the outer fluid phase can be cytotoxic to the cells present within the hydrogels. We present a method to synthesize monodisperse alginate hydrogels enabled by acoustics in Chapter 7 of this dissertation.

1.4.2 Aqueous two-phase systems

Aqueous two-phase systems (ATPS) provide a promising platform for cell culturing studies. ATPS comprise aqueous polymers whose thermodynamic properties inhibit mixing. This phenomenon results in liquid/liquid phase separation of the water-soluble polymers, causing partition into distinct regions of an aqueous volume at concentrations determined by their equilibrium phase diagram. Mace et al. out of Harvard University published a comprehensive body of work describing the phase separation of two-component mixtures of 23 aqueous polymers and 11 aqueous surfactant solutions.[81] Their work includes a table of observed miscibility between each of the possible combinations. Their group observed the separation of mixtures by step-gradients in solution component densities.

Phase separation at various component volume fractions and temperature is predicted by a binodal curve on a phase diagram. The binodal can be determined, as explained in a review by Igbal et al. and by Kaul in ATPS, by turbidometric titration, cloud point, and node determination.[82,83] The binodal determines at what specific concentrations (or volume fractions) two components are immiscible. The relationship of two aqueous phases is described by the partition coefficient K as seen in Equation 1.4.

$$K = \frac{Conc._{AT}}{Conc._{AB}} \qquad \text{Equation 1.4}$$

K is the partition coefficient of the fluid in the top phase (A_T) and in the bottom phase (A_B) at equilibrium. For ATPS there is always a small amount of polymer in each phase. The polymers PEG and DEX are ideal for ATPS applications as they are inexpensive, readily available, and the binodal for PEG and DEX in water has been measured by several groups, as exemplified by **Figure 1.11.**

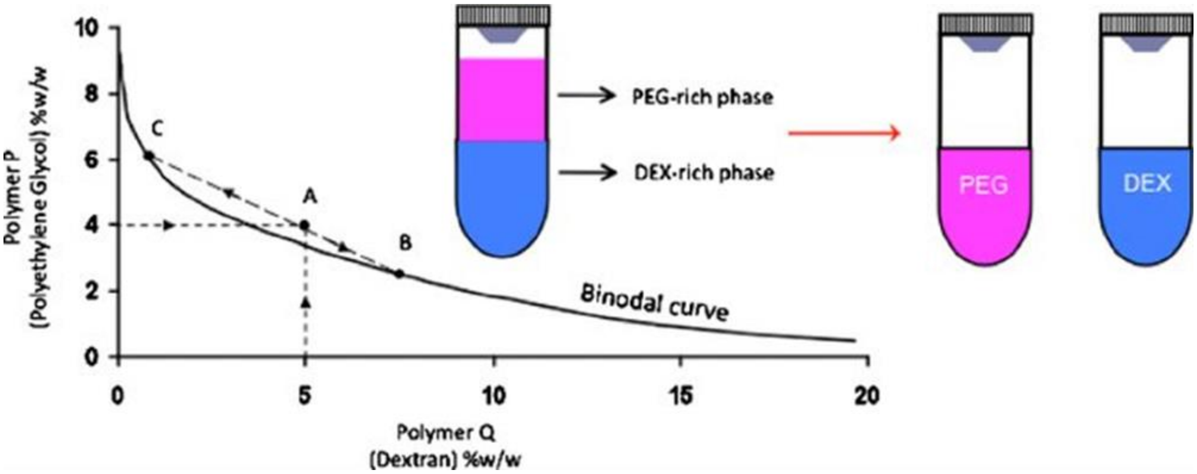

Figure 1.11. ATPS of PEG and DEX. Phase diagram of PEG and DEX at varying weight percentage concentrations. Points above the binodal curve will exhibit phase separation like that of an oil in water phase. (Figure taken from Tavana, H. et al. “Aqueous biphasic microprinting approach to tissue engineering”).[84]

As there is no all-encompassing theory on liquid-liquid demixing, certain models are used to describe the factors involved in phase partitioning.[82] Professor

Per-Ake Albertsson's model is commonly used since it incorporates many of the hypothesized physical parameters involved in aqueous two-phase systems.[85] These parameters include, electrochemical properties, hydrophobicity, biological affinity, molecular size, and physical conformation of the molecule. Albertsson's model has largely been incorporated in ATPS studies and was originally used to describe purification of chloroform from other cell products.[85,86]

One of the limiting factors involved in processing ATPS into drops is the low interfacial tension (~0.1 mN/m) between the two aqueous phases. Interfacial tension is a form of surface tension where the quantity defines the force that holds the surface of a component phase together in the presence of a different phase (i.e. a line tension). For water-in-oil systems, the interfacial tension is measured on the order of ten mN/m, whereas ATPS are on the order of 0.1 mN/m.[87,88] Because of low interfacial tension, ATPS droplet breakup does not occur spontaneously due to viscous flow, in stark contrast to large interfacial tension water-in-oil systems. The narrow frequency ranges where droplet formation can occur and the small growth rates, as predicted by Raleigh-Plateau theory, greatly limits ATPS drop formation in microfluidic droplet generators.

Ziemecka et al. out of Delft University of Technology published a method to force droplet breakup of low interfacial tension ATPS.[10] The group presented a method to form monodisperse droplets in a microfluidic device for ATPS. The group incorporated a piezoelectric disk over a DEX inner phase fluid reservoir which delivered a pulsing jet into a PEG intercepted T-junction PDMS microfluidic device. The additional force of the piezoelectric disc provided the necessary external physical force to drive droplet breakup for the ATPS. This method holds promise for further research in generated monodisperse hydrogels for biological studies. Incorporating alginate into the dispersed phase of DEX-PEG ATPS method may provide a useful tool for encapsulating cells and other biological components into hydrogel microspheres.

1.5 References

(1) United Nations Department of Economic and Social Affairs. *World Population Prospects: The 2017 Revision*; 2017.

(2) St John, A.; Price, C. P. Existing and Emerging Technologies for Point-of-Care Testing. *Clinica Biochemistry Reviews.* 2014, *35* (3), 155–167.

(3) Centers for Medicare & Medicaid Services. National health expenditures 2016 highlights https://www.cms.gov/Research-Statistics-Data-and-Systems/Statistics-Trends-and-Reports/NationalHealthExpendData/downloads/highlights.pdf.

(4) Shapiro, H. *Practical Flow Cytometry Fourth Edition*; John Wiley & sons, inc. 2004, 166-178.

(5) Edwards, B. S.; Sklar, L. A. Flow Cytometry: Impact on Early Drug Discovery. *Journal of Biomolecular Screening.* 2015, *20* (6), 689–707.

(6) Yang, R. J.; Fu, L. M.; Hou, H. H. Review and Perspectives on Microfluidic Flow Cytometers. *Sensors and Actuators B: Chemical*. 2018, 266, 26–45.

(7) Edwards, B. S.; Oprea, T.; Prossnitz, E. R.; Sklar, L. A. Flow Cytometry for High-Throughput, High-Content Screening. *Current Opinion in Chemical Biology*. 2004, 8 (4), 392–398.

(8) Carregal-Romero, S.; Caballero-Díaz, E.; Beqa, L.; Abdelmonem, A. M.; Ochs, M.; Hühn, D.; Suau, B. S.; Valcarcel, M.; Parak, W. J. Multiplexed Sensing and Imaging with Colloidal Nano- and Microparticles. *Annual Review Analytical Chemistry.* 2013, *6* (1), 53–81.

(9) Shang, L.; Cheng, Y.; Zhao, Y. Emerging Droplet Microfluidics. *Chemical Reviews*. 2017, 117 (12) 7964–8040.

(10) Ziemecka, I.; van Steijn, V.; Koper, G. J. M.; Rosso, M.; Brizard, A. M.; van Esch, J. H.; Kreutzer, M. T. Monodisperse Hydrogel Microspheres by Forced Droplet Formation in Aqueous Two-Phase Systems. *Lab on a Chip.* 2011, *11*

(4), 620–624.

(11) Lenshof, A.; Laurell, T. Continuous Separation of Cells and Particles in Microfluidic Systems. *Chemical Society Reviews.* 2010, *39* (3), 1203.

(12) Kundt, A. III. Acoustic Experiments. *London, Edinburgh, Dublin Philosophy Magazine and Journal of Science.* 1868, *35* (234), 41–48.

(13) Bassindale, P. G.; Phillips, D. B.; Barnes, A. C.; Drinkwater, B. W. Measurements of the Force Fields within an Acoustic Standing Wave Using Holographic Optical Tweezers. *Applied Physics Letters.* 2014, *104* (16), 163504.

(14) Gor'kov, L. P. Forces Acting on a Small Particle in an Acoustic Field within an Ideal Fluid. *Doklady Akademii Nauk SSSR.* 1961, *140* (1), 88–91.

(15) Bruus, H. Acoustofluidics 7: The Acoustic Radiation Force on Small Particles. *Lab on a Chip.* 2012, *12* (6), 1014.

(16) Kozuka, T.; Yasui, K.; Tuziuti, T.; Towata, A.; Iida, Y. Acoustic Standing-Wave Field for Manipulation in Air. *Japanese Journal of Applied Physics.* 2008, *47* (5 PART 2), 4336–4338.

(17) Yasuda, K.; Kiyama, M.; Umemura, S.; Takeda, K. Deoxyribonucleic Acid Concentration Using Acoustic Radiation Force. *Journal of Acoustical Society of America.* 1996, *99* (2), 1248–1251.

(18) Piyasena, M. E.; Austin Suthanthiraraj, P. P.; Applegate, R. W.; Goumas, A. M.; Woods, T. A.; López, G. P.; Graves, S. W. Multinode Acoustic Focusing for Parallel Flow Cytometry. *Analytical Chemistry.* 2012, *84* (4), 1831–1839.

(19) Yasuda, K.; Haupt, S. S.; Umemura, S.; Yagi, T.; Nishida, M.; Shibata, Y. Using Acoustic Radiation Force as a Concentration Method for Erythrocytes. *Journal of Acoustical Society of America.* 1997, *102* (c), 642–645.

(20) Morgenthaler, N. G.; Kostrzewa, M. Rapid Identification of Pathogens in Positive Blood Culture of Patients with Sepsis: Review and Meta-Analysis of the Performance of the Sepsityper Kit. *International Journal of Microbiology*. 2015, 2015 (827416), 10.

(21) Gracias, K. S.; McKillip, J. L. A Review of Conventional Detection and Enumeration Methods for Pathogenic Bacteria in Food. *Canadian Journal of Microbiology.* 2004, *50* (11), 883–890.

(22) Lagier, J. C.; Edouard, S.; Pagnier, I.; Mediannikov, O.; Drancourt, M.; Raoult, D. Current and Past Strategies for Bacterial Culture in Clinical Microbiology. *Clinical Microbiology Reviews.* 2015, *28* (1), 208–236.

(23) Antfolk, M.; Muller, P. B.; Augustsson, P.; Bruus, H.; Laurell, T. Focusing of Sub-Micrometer Particles and Bacteria Enabled by Two-Dimensional Acoustophoresis. *Lab on a Chip.* 2014, *14* (15), 2791–2799.

(24) Lighthill, S. J. Acoustic Streaming. *Journal of Sound Vibrations.* 1978, *61* (3), 391–418.

(25) Boluriaan, S.; Morris, P. Acoustic Streaming: From Rayleigh to Today. *International Journal of Aeroacoustics.* 2003, *2* (3), 255–292.

(26) Leighton, T. G.; Walton, A. J.; Pickworth, M. J. W. Primary Bjerknes Forces. *European Journal of Physics.* 1990, *11* (1), 47–50.

(27) Crum, L. A. Bjerknes Forces on Bubbles in a Stationary Sound Field. *Journal of Acoustical Society of America.* 1975, *57* (6), 1363–1370.

(28) Dayton, P. A.; Morgan, K. E.; Klibanov, A. L.; Brandenburger, G.; Nightingale, K. R.; Ferrara, K. W. A Preliminary Evaluation of the Effects of the Primary and Secondary Radiation Forces on Acoustic Contrast Agents. *IEEE Transactions on Ultrasonics, Ferroelectrics, and Frequency Control.* 1997, *44* (6), 1264–1277.

(29) Destgeer, G.; Ha, B. H.; Jung, J. H.; Sung, H. J. Submicron Separation of Microspheres via Travelling Surface Acoustic Waves. *Lab on a Chip.* 2014, *14* (24), 4665–4672.

(30) Collins, D. J.; Ma, Z.; Ai, Y. Highly Localized Acoustic Streaming and Size-Selective Submicrometer Particle Concentration Using High Frequency Microscale Focused Acoustic Fields. *Analytical Chemistry.* 2016, *88* (10), 5513–5522.

(31) Ohlsson, P.; Evander, M.; Petersson, K.; Mellhammar, L.; Lehmusvuori, A.; Karhunen, U.; Soikkeli, M.; Seppä, T.; Tuunainen, E.; Spangar, A.; et al. Integrated Acoustic Separation, Enrichment, and Microchip Polymerase Chain Reaction Detection of Bacteria from Blood for Rapid Sepsis Diagnostics. *Analytical Chemistry.* 2016, *88* (19), 9403–9411.

(32) Brown, M.; Wittwer, C. Flow Cytometry: Principles and Clinical Applications in Hematology. *Clinical Chemistry.* 2000, *46* (8 II), 1221–1229.

(33) Olempska, M.; Eisenach, P. A.; Ammerpohl, O.; Ungefroren, H.; Fandrich, F.; Kalthoff, H. Detection of Tumor Stem Cell Markers in Pancreatic Carcinoma Cell Lines. *Hepatobiliary and Pancreatic Diseases International.* 2007, *6* (1), 92–97.

(34) Barlogie, B.; Raber, M. N.; Schumann, J.; Johnson, T. S.; Drewinko, B.; Swartzendruber, D. E.; Göhde, W.; Andreeff, M.; Freireich, E. J. Flow Cytometry in Clinical Cancer Research. *Cancer Research.* 1983, *43* (9), 3982–

3997.

(35) Derveaux, S.; Stubbe, B. G.; Braeckmans, K.; Roelant, C.; Sato, K.; Demeester, J.; De Smedt, S. C. Synergism between Particle-Based Multiplexing and Microfluidics Technologies May Bring Diagnostics Closer to the Patient. *Analytical and Bioanalytical Chemistry*. 2008, 2453–2467.

(36) Munson, B. R., et al. Fluid mechanics, Wiley Singapore. 2013, 278-303.

(37) Whitesides, G. M. The Origins and the Future of Microfluidics. *Nature*. 2006, 442, 368–373.

(38) Edwards, B. S.; Sklar, L. A. Flow Cytometry. *Journal of Biomolecular Screening.* 2015, *20* (6), 689–707.

(39) Oakey, J.; Applegate, R. W.; Arellano, E.; Carlo, D. Di; Graves, S. W.; Toner, M. Particle Focusing in Staged Inertial Microfluidic Devices for Flow Cytometry. *Analytical Chemistry.* 2010, *82* (9), 3862–3867.

(40) Rooney, J. A. Hydrodynamic Shearing of Biological Cells. *Journal of Biological Physics.* 1974, *2* (1), 26–40.

(41) Piyasena, M. E.; Graves, S. W. The Intersection of Flow Cytometry with Microfluidics and Microfabrication. *Lab on a Chip.* 2014, *14* (6), 1044–1059.

(42) Sia, S. K.; Whitesides, G. M. Microfluidic Devices Fabricated in Poly(Dimethylsiloxane) for Biological Studies. *Electrophoresis*. 2003, 24 (21), 3563.

(43) Andersson, H.; Van den Berg, A. Microfluidic Devices for Cellomics: A Review. *Sensors and Actuators, B: Chemical*. 2003, 92 (3), 315-325.

(44) Yager, P.; Edwards, T.; Fu, E.; Helton, K.; Nelson, K.; Tam, M. R.; Weigl, B. H. Microfluidic Diagnostic Technologies for Global Public Health. *Nature*. 2006, 442: 412.

(45) Sugioka, K.; Cheng, Y.; Midorikawa, K. Three-Dimensional Micromachining of Glass Using Femtosecond Laser for Lab-on-a-Chip Device Manufacture. *Applied Physics A: Materials Science and Processing.* 2005, 81 (1), 1-10.

(46) Queste, S.; Salut, R.; Clatot, S.; Rauch, J. Y.; Khan Malek, C. G. Manufacture of Microfluidic Glass Chips by Deep Plasma Etching, Femtosecond Laser Ablation, and Anodic Bonding. *Microsystem Technologies*. 2010, 16 (8-9), 1485-1493.

(47) Ng, J. M. K.; Gitlin, I.; Stroock, A. D.; Whitesides, G. M. Components for Integrated Poly(Dimethylsiloxane) Microfluidic Systems. *Electrophoresis*. 2002, 23 (20), 3461–3473.

(48) Friend, J.; Yeo, L. Fabrication of Microfluidic Devices Using Polydimethylsiloxane. *Biomicrofluidics.* 2010, 4 (2), 026502.

(49) Lenshof, A.; Evander, M.; Laurell, T.; Nilsson, J. Acoustofluidics 5: Building Microfluidic Acoustic Resonators. *Lab on a Chip.* 2012, *12* (4), 684.

(50) E. Verpoorte and N. F. De Rooij, Microfluidics Meets MEMS, *Proceedings of the IEEE*. 2003, 91 (6), 930-953.

(51) Xia, Y. N.; Whitesides, G. M. Soft Lithography. *Annual Review of Materials Science.* 1998, *37* (5), 551–575.

(52) Reichmanis, E.; Thompson, L. F. Polymer Materials for Microlithography. *Chemical Reviews.* 1989, *89* (6), 1273–1289.

(53) Owen, M. J.; Smith, P. J. Plasma Treatment of Polydimethylsiloxane. *Journal of Adhesion Science Technology.* 1994, *8* (10), 1063–1075.

(54) Buehler, J., Steiner, F.-P., & Baltes, H. Silicon Dioxide Sacrificial Layer Etching in Surface Micromachining. *Journal of Micromechanics and Microengineering*. 1997, (1), R1-R13.

(55) Wu, B., et al. High Aspect Ratio Silicon Etch: A Review. *Journal of Applied Physics.* 2010, 108 (5): 051101.

(56) Toofan, M.; Toofan, J. A Brief Review of the Cleaning Process for Electronic Device Fabrication. *Developments in Surface Contamination and Cleaning*. 2015, Ch. 5, 185-212.

(57) Mu, X.; Liang, Q.; Hu, P.; Ren, K.; Wang, Y.; Luo, G. Laminar Flow Used as “Liquid Etch Mask” in Wet Chemical Etching to Generate Glass Microstructures with an Improved Aspect Ratio. *Lab on a Chip.* 2009, *9* (14), 1994–1996.

(58) S. Linder, H. Baltes, F. Gnaedinger and E. Doering, Photolithography in Anisotropically Etched Grooves, *Proceedings of Ninth International Workshop on Micro Electromechanical Systems*. San Diego, CA, USA, 1996, 38-43.

(59) Laerme, F.; Schilp, A.; Funk, K.; Offenberg, M. Bosch Deep Silicon Etching: Improving Uniformity and Etch Rate for Advanced MEMS Applications. In *Technical Digest. IEEE International MEMS 99 Conference. Twelfth IEEE International Conference on Micro Electro Mechanical Systems (Cat. No.99CH36291)*. 1999, 211–216.

(60) Williams, K. R.; Muller, R. S. Etch Rates for Micromachining Processing.Pdf. *Journal of Microelectromechanical Systems.* 1996, *7157* , 256–269.

(61) Khan, M. F.; Ghavanini, F. A.; Haasl, S.; Löfgren, L.; Persson, K.; Rusu, C.;

Schjølberg-Henriksen, K.; Enoksson, P. Methods for Characterization of Wafer-Level Encapsulation Applied on Silicon to LTCC Anodic Bonding. *Journal of Micromechanics Microengineering.* 2010, *20* (6), 10.

(62) Mack, S. A Comparative Investigation of Physico-Chemical Processes at the Boundary Layer of Directly and Anodically Bonded Solids, Zugl.: Halle-Wittenberg, Univ, Diss. 1997.Wikipedia Image

(63) Vladisavljević, G. T.; Shahmohamadi, H.; Das, D. B.; Ekanem, E. E.; Tauanov, Z.; Sharma, L. Glass Capillary Microfluidics for Production of Monodispersed Poly (Dl-Lactic Acid) and Polycaprolactone Microparticles: Experiments and Numerical Simulations. *Journal of Colloid Interface Science.* 2014, *418*, 163–170.

(64) Kim, S.-H.; Kim, J. W.; Cho, J.-C.; Weitz, D. A. Double-Emulsion Drops with Ultra-Thin Shells for Capsule Templates. *Lab on a Chip.* 2011, *11* (18), 3162–3166.

(65) Zieringer, M. A.; Carroll, N. J.; Abbaspourrad, A.; Koehler, S. A.; Weitz, D. A. Microcapsules for Enhanced Cargo Retention and Diversity. *Small.* 2015, *11* (24), 2903–2909.

(66) Lenshof, A.; Evander, M.; Laurell, T.; Nilsson, J. Acoustofluidics 5: Building Microfluidic Acoustic Resonators. *Lab on a Chip.* 2012, *12* (4), 684.

(67) Piyasena, M. E.; Suthanthiraraj, P. P. A.; Applegate, R. W.; Goumas, A. M.; Woods, T. A.; López, G. P.; Graves, S. W. Multinode Acoustic Focusing for Parallel Flow Cytometry. *Analytical Chemistry.* 2012, *84* (4), 1831–1839.

(68) Kalb, D. M.; Fencl, F. A.; Woods, T. A.; Swanson, A.; Maestas, G. C.; Juárez, J. J.; Edwards, B. S.; Shreve, A. P.; Graves, S. W. Line-Focused Optical Excitation of Parallel Acoustic Focused Sample Streams for High Volumetric and Analytical Rate Flow Cytometry. *Analytical Chemistry.* 2017, 89 (18), 9967–9975.

(69) Eyderman, S.; John, S.; Hafez, M.; Al-Ameer, S. S.; Al-Harby, T. S.; Al-Hadeethi, Y.; Bouwes, D. M. Light-Trapping Optimization in Wet-Etched Silicon Photonic Crystal Solar Cells. *Journal of Applied Physics.* 2015, *118* (2).

(70) Yahaya, N. A.; Yamada, N.; Kotaki, Y.; Nakayama, T. Characterization of Light Absorption in Thin-Film Silicon with Periodic Nanohole Arrays. *Optics Express.* 2013, *21* (March), 5924–5930.

(71) Grenvall, C.; Magnusson, C.; Lilja, H.; Laurell, T. Concurrent Isolation of Lymphocytes and Granulocytes Using Prefocused Free Flow Acoustophoresis. *Analytical Chemistry.* 2015, *87* (11), 5596–5604.

(72) Grenvall, C.; Augustsson, P.; Folkenberg, J. R.; Laurell, T. Harmonic

Microchip Acoustophoresis: A Route to Online Raw Milk Sample Precondition in Protein and Lipid Content Quality Control. *Analytical Chemistry.* 2009, *81* (15), 6195–6200.

(73) Cushing, K. W.; Piyasena, M. E.; Carroll, N. J.; Maestas, G. C.; López, B. A.; Edwards, B. S.; Graves, S. W.; López, G. P. Elastomeric Negative Acoustic Contrast Particles for Affinity Capture Assays. *Analytical Chemistry.* 2013, *85* (4), 2208–2215.

(74) S. Mytnyk, A. G. L. Olive, F. Versluis, J. M. Poolman, E. Mendes, R. Eelkema, J. H. van Esch, *Angewandte Chemistry.* 2017, 129, 15119.

(75) Workman, V. L.; Dunnett, S. B.; Kille, P.; Palmer, D. Microfluidic Chip-Based Synthesis of Alginate Microspheres for Encapsulation of Immortalized Human Cells. *Biomicrofluidics.* 2007, *1* (1). 014105

(76) Shu, A. F.-J. and C. F. and D.-J. C. and J. G. and J. K. and A. C. and W. Bioprinting of Human Pluripotent Stem Cells and Their Directed Differentiation into Hepatocyte-like Cells for the Generation of Mini-Livers in 3D. *Biofabrication.* 2015, *7* (4), 44102.

(77) Tasoglu, S.; Demirci, U. Bioprinting for Stem Cell Research. *Trends in Biotechnology*. 2013, 10–19.

(78) Demirci, U.; Montesano, G. Single Cell Epitaxy by Acoustic Picolitre Droplets. *Labon a Chip.* 2007, *7* (9), 1139–1145.

(79) Lee, C. Y.; Pang, W.; Yu, H.; Kim, E. S. Subpicoliter Droplet Generation Based on a Nozzle-Free Acoustic Transducer. *Applied Physics Letters.* 2008, *93* (3), 034104.

(80) Fang, Y.; Frampton, J. P.; Raghavan, S.; Sabahi-Kaviani, R.; Luker, G.; Deng, C. X.; Takayama, S. Rapid Generation of Multiplexed Cell Cocultures Using Acoustic Droplet Ejection Followed by Aqueous Two-Phase Exclusion Patterning. *Tissue Engineering Part C Methods.* 2012, *18* (9), 647–657.

(81) MacE, C. R.; Akbulut, O.; Kumar, A. A.; Shapiro, N. D.; Derda, R.; Patton, M. R.; Whitesides, G. M. Aqueous Multiphase Systems of Polymers and Surfactants Provide Self-Assembling Step-Gradients in Density. *Journal of American Chemical Society.* 2012, *134* (22), 9094–9097.

(82) Iqbal, M.; Tao, Y.; Xie, S.; Zhu, Y.; Chen, D.; Wang, X.; Huang, L.; Peng, D.; Sattar, A.; Shabbir, M. A. B.; et al. Aqueous Two-Phase System (ATPS): An Overview and Advances in Its Applications. *Biological Procedures Online*. 2016, 1–18.

(83) Hatti-kaul, R. Aqueous Two-Phase Systems. *Molecular Biotechnology.* 2001, *19* (3), 697–713.

(84) Tavana, H.; Takayama, S. Aqueous Biphasic Microprinting Approach to Tissue Engineering. *Biomicrofluidics.* 2011. 5 (1), 013404.

(85) Albertsson, P.-Å. Aqueous Biphasic Systems. Properties and Applications in Bioseparation. In *Aqueous Biphasic Separations: Biomolecules to Metal Ions*. 1995, 21–30.

(86) Grilo, A. L.; Aires-Barros, M. R.; Azevedo, A. M. Partitioning in Aqueous Two-Phase Systems: Fundamentals, Applications and Trends Partitioning in Aqueous Two-Phase Systems: Fundamentals, Applications and Trends. *Seperation and Purification Reviews.* 2016, *45* (45), 68–80.

(87) Peters, F.; Arabali, D. Interfacial Tension between Oil and Water Measured with a Modified Contour Method. *Colloids Surfaces A: Physicochemical and Engineering Aspects.* 2013, *426*, 1–5.

(88) Jian, C.; Poopari, M. R.; Liu, Q.; Zerpa, N.; Zeng, H.; Tang, T. Reduction of Water/Oil Interfacial Tension by Model Asphaltenes: The Governing Role of Surface Concentration. *Journal of Physical Chemistry B.* 2016, *120* (25), 5646–5654.

Chapter 2: Goals and Overview of this Work

Incorporating acoustic technologies to existing platforms will aid in the efficiency, reduction of cost, and fidelity to various technologies in the biomedical field. As described in the previous section, acoustic integration has illustrated its utility across multiple fields of study. The ability of acoustic standing waves to precisely separate components within a sample media has already shown its applications for biological samples, namely in blood cell enrichment, flow cytometry platforms, and affinity capture studies. While these cases have shown promise in integrating acoustophoretic technologies, the field still has many avenues to explore and refine. The goal of this work is to exploit the benefits of acoustic integration into flow cytometry platforms as well as in assay development for point-of-care testing platforms and in acoustically assisted synthesis of hydrogel microspheres for 3D cell culture. We also seek a better understanding of acoustics in some of these emerging fields. Acoustic flow cytometry shows potential as an exceptional method to focus particles without the need of a fluid sheath, but its incorporation into automated platforms has been less studied. Our goal is to provide methods to fabricate optically clear flow chambers for high throughput flow cytometry applications. Apart from flow cytometry, we aim to engineer a simple syringe device with an acoustic actuator attached to a capillary “needle” towards creation of a point-of-care affinity capture device. In addition to sample focusing and separation studies, we seek to employ acoustics to create a microfluidic device to breakup co-flowing ATPS solutions into monodisperse drops for synthesis of hydrogels for 3D cell culture.

In **Chapter 3** of this dissertation, we introduce a method of fabricating optically clear, silicon core flow chambers for acoustic flow cytometry. The device fabrication method yields flow chambers with properties optimal for their use in diverse application, as exemplified by the two subsequent chapters in this dissertation (Chapters 4 and 5) focusing on flow cytometry applications. This chapter provides detailed fabrication steps including clean room procedures and post etching steps necessary for the construction of these flow chambers. We show that etching completely through a silicon wafer at various widths provides a simple approach to parallel stream acoustic focusing, while providing a transparent device for optical interrogation. Depending on the desired number of nodes and the applied acoustic frequency, multiple streams are tightly focused in parallel for these flow chambers with no back scatter from an incident laser source onto an etched opaque bottom channel. This work is being prepared as a methods article for *PLOS One*.

One of the fabricated acoustic flow chambers from the previous chapter have been integrated into a custom high throughput parallel acoustic flow cytometer in **Chapter 4** of this dissertation. This collaborative work in its entirety has been published in *Analytical Chemistry.* The platform we developed uses parallel acoustic sample stream focusing to split sample contents in up to 16 streams that are interrogated in parallel, greatly increasing the analytical rates and throughput capabilities for flow cytometry. I fabricated the 2.3 mm optically transparent acoustic flow chamber responsible for focusing the various microparticles investigated to assess the sensitivity and throughout efficiency of the instrument. Additionally, I characterized the flow chamber dimensions through image J analysis for calculations on the theoretical number of nodes generated at our working input transducer frequencies. These calculations are critical in the subsequent particle stream analysis. I was involved, as well as the other authors, in constructing and adjusting the optical layout of the flow cytometer. Daniel Kalb tested fluorescent standard beads as a proof of principle to demonstrate its efficacy in comparison to state-of-the-art flow cytometry while increasing volumetric rates up to 10 mL/min. Daniel Kalb also performed the extensive laser line profile characterization and subsequent analysis of increasing sensitivity across the various laser intensity regions. The submitted manuscript represents our collaborative work for this chapter and is shown here in full to be appreciated in context. The formatting matches that of this dissertation.

Chapter 5 describes how acoustic focusing is affected by an automated sampling system, where intermittent air bubbles are introduced. Our investigation details acoustic focusing of particles at the air water interface for several sample boluses flowing through an acoustic flow chamber. Many medical reference laboratories have automated systems where hundreds or thousands of individual patient samples are processed via automation. For samples requiring flow cytometry, a robotic arm aspirates samples at a constant rate taking in air between wells. We explore if acoustic flow cytometry systems could be used in automated processes while assessing if the introduction of air would be too disruptive in acoustic focusing. Our results show that, while air briefly disrupts acoustic focusing, the sample media almost immediately focuses back to the node of an acoustic standing wave and minimal particle counts are lost in the process. We are incorporating a quantifier for the exact amount of time it takes for sample streams to recover across various flow rates and particle sizes after an air bubble passes through the system. We are submitting this work as a full article to *Analytical Chemistry*.

Chapter 6 details a simple low-cost device towards a point-of-care testing platform using acoustics and biofunctionalized elastomeric microparticles for affinity capture assays in blood samples. We demonstrate the ability to capture fluorescently labeled antibodies on the surface of NACs in the presence of dilute porcine whole blood. The outcome of our work illustrates that a specific target ligand can be captured, trapped, and separated via acoustics from background components to help diagnose the early onset of an infection. These NACs migrate and trap to the antinode of an acoustic standing wave generated by a piezoelectric transducer coupled to a simple glass capillary-syringe device. While the transducer is powered, the NACs remain clustered in regions throughout the capillary, while positive acoustic contrast particles (blood cells or polystyrene particles) focus to the node and are extruded from the device as effluent. The purified NACs with captured fluorescent antibodies can then be extruded and interrogated by fluorescence microscopy or standard flow cytometry. This work is being prepared for submission to *Lab on a Chip*.

As another demonstration of acoustofluidic technology coupled to soft materials, **Chapter 7** details construction of a microfluidic device with an acoustic actuator, comprising an audio speaker, to generate 3D hydrogels from ATPS drops. This work is motivated by the limitations of current technologies for the generation of hydrogel microspheres for cell culture. Common methods involve microfluidics to generate water-in-oil emulsions to create hydrogels via crosslinking of the drop polymer solution. The primary disadvantage of these systems is that oils can be toxic and prevents delivery of nutrients to cells. Synthesizing hydrogels in water systems provides a biocompatible and bioinspired environment for cell culturing and enables delivery of hydrophilic nutrients to the encapsulated cells. I incorporated an audio speaker to the acoustofluidic device to provide the necessary external physical force to drive fluidic jet breakup into monodisperse droplets. I studied the reproducibility and droplet synthesis characterization over three devices and one case of droplet synthesis with cells present. The resulting hydrogel-cell constructs were collected and cultured by Jacqueline De Lora for up to 9 days, during which time they form cancer spheroid-like assemblies. Jacqueline De Lora also performed the flow cytometry live/dead assay in this chapter. This collaborative work is being prepared for submission as a communication to *Nature Methods*.

This body of work highlights the benefits of integrating acoustic technologies to various platforms in the biomedical field. We present methods of developing instrumentation components and microfluidic devices integrated with acoustics to separate sample components, develop technology towards point-of-care testing platforms, and generate 3D hydrogels for cell culturing. Conclusions from this work and future directions are presented in **Chapter 8**. The need to develop remotely accessible testing platforms and rapid sample interrogation is an ongoing effort and must continue to balance the biomedical needs of a growing human population. This dissertation illustrates the versatility of acoustic technology integration and its impact on future growth of these platforms.

Chapter 3: Methods for Fabricating Optically Clear Silicon Core Flow Chambers for Parallel Acoustic Flow Cytometry

Frank A. Fencl[1], Gayatri P. Gautam[2], Daniel M. Kalb[3], Travis A. Woods[1], Loreen R. Stromberg[4], Menake E. Piyasena[2], Steven W. Graves[1]

[1] Department of Chemical and Biological Engineering, Center for Biomedical Engineering, University of New Mexico, Albuquerque, NM

[2] Department of Chemistry, New Mexico Institute of Mining and Technology, Socorro, NM

[3]Los Alamos National Labs, Los Alamos, NM

[4] Department of Mechanical Engineering, Iowa State University, Ames, IA

3.1 Abstract

We present a rapid and cost-effective method of silicon device processing techniques for the construction of silicon core, double glass-capped, optically clear microfluidic flow chambers (SCGFC) for acoustofluidic applications. It is well known that silicon-glass capped microfluidic devices are a promising material for acoustic devices due to high characteristic acoustic impedance values of silicon and glass. Many of these devices are fabricated in clean rooms using semiconductor silicon processing techniques. The precision and control of these methods allows for production of etched silicon channels with high feature resolution. The resulting rectangular channel profiles are excellent for acoustofluidics where a resonant acoustic standing wave is required for microparticle focusing. However, these devices may experience increased operating temperatures due to localized heating from an incident laser beam directed into the channel for interrogating the sample contents. Etched silicon also has reflective and scatter properties which can interfere with optics and image collection. Our group hypothesized that opaque-bottomed silicon etched microfluidic flow chambers experience additional excess heat generation by laser transmittance into the channel. To address this issue and minimize optical scatter and reflectance off the opaque bottom, we employ standard MEMS etching techniques to etch wide channels completely through a thin silicon (200 and 500 µm thickness) wafer and bond borosilicate glass slides on either side to cap the channel so that a light source may transmit through the device.

3.2 Introduction

Acoustofluidics is emerging as an effective tool for analysis of blood and other biological matrices. Microfluidics combined with acoustophoresis, the movement of a particle using sound waves, are the defining principles of acoustofluidics. The use of acoustics to manipulate biological media has proven to be a gentle non-contact method of interrogation.[1–4] This area of research has largely been used for blood component separations and affinity capture studies on microparticle-based assays as in flow cytometry.[5–9] Recent advancements in flow cytometry have incorporated acoustics for multi stream focusing and high-throughput analysis.[10–13] The microfluidic flow chamber is a key component in acoustic flow cytometry where the separation of sample components is determined by the flow rate, channel geometry, applied resonant acoustic frequency, and physical properties of the particle.[5,14]

The primary acoustic force acting on the particle has been derived and explained by L. P. Gorkov.[2,5,15–20] Important factors to consider are that the acoustic force, largely responsible for particle positioning within an acoustic standing wave, is dependent on the speed of sound within the medium, particle size, and the fluid density and compressibility in relation to the particles suspended in the medium.[21] The material choice for acoustic resonators is critical for generating standing waves.[22] Silicon and glass microfluidic devices are considered critical tools for acoustofluidic applications.[23]

For the contents herein, we refer to bulk acoustic standing wave resonators as opposed to standing surface acoustic wave resonators. Bulk acoustic standing wave (BAW) resonators are devices where a piezoelectric transducer is attached to the device causing the entire material to resonate with acoustic energy.[22,24] This bulk material resonance creates an acoustic standing wave within a channel in the device, where the acoustic force is transferred into the channel space and reflected within the geometry of the channel walls.[18,21,22,25] BAW devices are simpler to construct as they only require the high acoustic impedance device and an attached piezoelectric transducer compared to standing surface acoustic wave devices (SSAW) that require a material with low acoustic impedance in addition to a material with high acoustic impedance. This acoustic impedance mismatch is what creates a standing wave over the area where the acoustic force is being applied. Optically clear SSAW devices are also possible but require a transparent polymer such as polydimethylsiloxane (PDMS) in addition to the complex set of electrodes or interdigital transducers required to generate the surface acoustic standing wave.[26]

For BAW devices, the amount of energy reflected is dependent on materials with high characteristic acoustic impedance. A material with high acoustic impedance results in a more robust acoustic standing wave which translates to better particle focusing. This value can be expressed numerically with the equation:

$$Z = \rho c \qquad \text{Equation 1}$$

where, Z is the characteristic acoustic impedance, ρ is the density of the device material, and c is the speed of sound within the material. Silicon and glass have characteristic acoustic impedance values between 13 and 20 (10^6) kg/m^{2}s, making them good candidates for acoustofluidic applications. Metals can exhibit higher impedance values but are typically more difficult to pattern with channels because of requisite precision milling techniques.[27] In contrast, polymer materials like polystyrene or PDMS have low impedance values, between 1 and 2 (10^6) kg/m^{2}s, making them less applicable due to low material density and acoustic wave transduction.[22]

In addition to the high impedance values of silicon and glass, the materials are readily available, cost effective, and have a wide array of processing methods, that have continued to expand since the 1960's. Silicon as a semiconductor, is patterned and etched using many methods. Microfluidic etched channels in silicon are etched to specific depths by varying the exposure time to etchant. The Bosch process for example has well characterized etching steps, so controlling the number of steps results in a desired depth.[28] Wet etching methods with strong acids are harder to control the etched depth, but the length of exposure to the etchant and growth of an oxide layer can be adjusted to better control the etching process.[29]

Microfluidic channels etched into silicon are typically only etched to a depth that is less than the thickness of the material and are capped with an optically transparent borosilicate glass cover slide for imaging and interrogation of the channel contents. We hypothesize that a laser light source, for media interrogation within the channel, may cause localized heating that can disrupt the laminar flow profiles in microfluidic devices; a critical component of acoustic focusing. The property to absorb light onto silicon is commonly used for IR detection as well as for photovoltaic systems which is known to cause heating.[30–32]

To reduce etched silicon light scatter and reflection as well as eliminate the potential heat generated from a light source, our group developed a method using standard silicon processing techniques with additional post processing steps to construct optically clear flow chambers ideal for high throughput acoustic flow cytometry. We present here a method to fabricate a rectangular geometry etched channel for an optically clear silicon core flow chamber, double-capped with borosilicate glass cover sides (SCGFC).

3.3 Materials and methods

3.3.1 Photolithography

Specifications for five transparency photomasks were designed using AutoCAD 2013 (Autodesk ® Inc.) and transparency printing was outsourced to CAD/Art Services, Inc. at a resolution of approximately 10,000 dpi. Photomasks were designed in house to produce an image the size of a standard microscope slide (2.5 x 7.5 cm), with varying sizes and shapes of microchannels. The channel widths for the six devices were 0.6 mm, 1 mm, 2 mm, 5 mm, 10 mm, and 20 mm. Examples of two masks can be seen in Figure 3.1. All fabrication steps were performed under class 100 clean room conditions at the Center for Intergrated Nano Technologies (CINT) in Albuquerque NM or class 1000 clean room conditions at the Manufacturing Training and Technology Center (MTTC) at the University of New Mexico. Silicon wafers (200 and 500 µm thick, double-sided polish, University Wafer Inc.) were pretreated with heat and hexamethyldisilazane (HMDS) for 5 minutes. AZ 9250 positive photoresist polymer was applied onto the silicon wafer surface prior to spin coating. Wafers were spin-coated (Clariant. Cee® 200X, Brewer Science) for 40 seconds at 2000 rpm, followed by a 10-minute soft bake at 110 ˚C, and subsequent cooling to room temperature (23 ˚C). The mask and wafer were placed in a mask aligner (Karl Suss MA6, SUSS MicroTec AG) and exposed to a high-energy ultraviolet radiation source for 45 seconds. Full illustration can be seen in supporting information for this chapter (Appendix A). Following exposure, the wafer was placed in AZ 400K series developer solution (Clariant) for 2 minutes, then rinsed 3 times with de-ionized water (>18.0 MΩ) and dried with pressurized nitrogen. The wafer was placed in the spin washer/dryer for 10 minutes to thoroughly clean and dry the surfaces prior to etching.

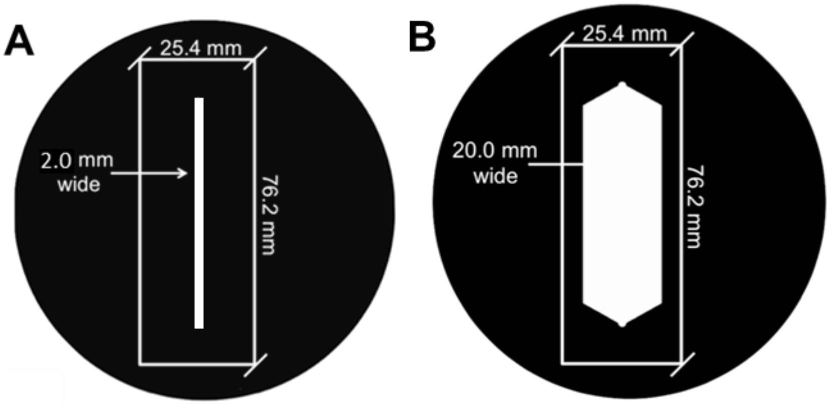

Figure 3.1. Photomask designs. (A) 2 mm channel pattern, (B) 20 mm channel pattern, Photomasks were printed on transparencies. White areas are transparent on the mask, while black areas are opaque. Thickness of lines for outer dimensions (25.4 x 76.2 mm) of the device have been exaggerated for clarity.

3.3.2 Bosch deep reactive ion etching (DRIE)

To etch the 200 or 500 µm deep microchannel completely through the silicon wafer, DRIE (1 min intervals of SF6 with 3 min passivation periods; Alcatel AMS 100, Alcatel Micro Machining Systems) via the Bosch process was initially carried out for 80 minutes for the thicker 500 µm wafer but was reduced to 50 minutes for 200 µm thick wafers.[28]

3.3.3 Photoresist removal

After DRIE, remaining photoresist (PR) was removed with acetone, after which the wafer was rinsed with deionized water and blown dry with nitrogen gas. To remove organic residues, devices were ashed in a “LOLA” Down Stream Plasma Ash (Plasmatherm Batchtop with Low Frequency Plasma Source) – Organic, BCB strip and device cleaning, for 60 minutes. The PR ash rate is approximately 2500-3000Å/min. The processing temperature was 150 ^{o}C. Process gasses included CO_2, O_2, N_2O and CF_4.

3.3.4 Thermal oxidation

A diffusion/annealing furnace (Tystar Titan 4600 – Room 1532) was used to initialize the removal of the etched scallop features remaining from Bosch DRIE. The oxidizer used thermal oxidation to grow a 200 nm silicon dioxide (SiO_2) layer onto the surface of the channel through a steam wet oxidation process. The oxide layer was grown at 1100 ^{o}C over a 2hr:52min:45sec period at an O_2 flow rate of 3 slm (standard liters per minute). Oxide growth was visually determined by the rainbow luster left after the oxidation process.

3.3.5 Buffered oxide etch

Removal of the oxide layer was achieved through buffered oxide etching. This process required devices to be submerged in a dilute solution of premixted 6:1 ammonium fluoride (NH_4F) and hydrofluoric acid (HF). Final concentration was 30-40% NH_4F, 5-10% HF, balance water for 3-5 minutes. After etching, the wafer was thoroughly rinsed with deionized H_2O. To determine whether the oxide layer was completely removed the degree of surface wettability using DI H_2O, was observed. If water was repelled from the surface (i.e. the observation of water beading rather than fully wetting), this indicated that the oxide layer had been removed. The devices were dried with pressurized N_2 and stored until assembly and testing.

3.3.6 SEM images.

The etched Si-substrates were thoroughly cleaned with deionized water followed by a methanol, acetone, and isopropyl alcohol rinse to remove any particles and dried with nitrogen. The surface roughness of the channel was investigated by using scanning electron microscopy (SEM) imaging (Nova NanoSEM 45) at Center for Integrated Nanotechnologies (CINT). SEM images were taken at the channel or near the two opposite ends of the main channel along the longitudinal direction. A tilt angle of 30 degree was used to image the edge profile as seen in Figure 3.2.

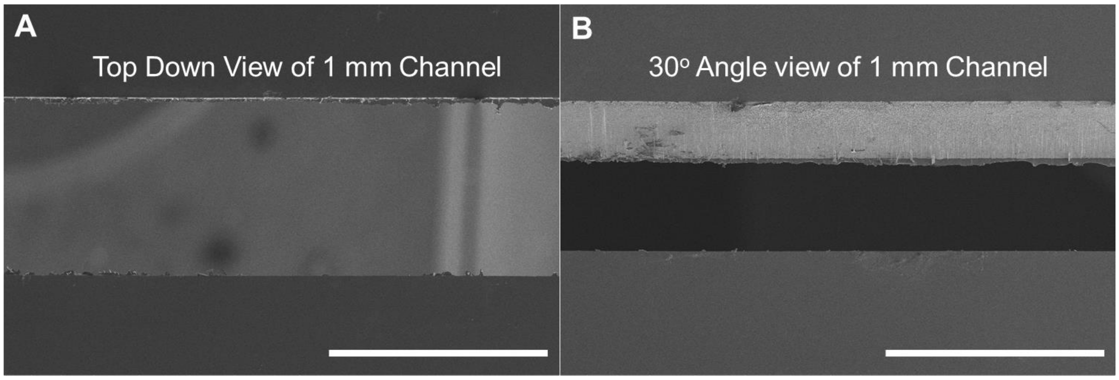

Figure 3.2. SEM Images of 1 mm x 0.5 mm x 50 mm channel microfluidic device. (A) Top down image, scale bar = 1 mm. (B) 30° angle image showing the edge and side-wall profiles. This angle illustrates the clean edges of the etched channel, scale bar = 1 mm.

3.3.7 Glass slide cleaning and preparation

Two holes (inlet and outlet), as seen in Figure 3.3 A, were drilled in a borosilicate microscope cover slide using a hand drill (Dremel Rotary 300 series, Dremel) with a diamond bit to approximately 1.5 mm in diameter. The silica wafer, a drilled glass cover slide, and an intact cover slide were cleaned using a piranha solution of sulfuric acid and hydrogen peroxide (7:3, respectively) for a maximum of 20 min then rinsed thoroughly with de-ionized water and dried under nitrogen gas prior to being anodically bonded together.

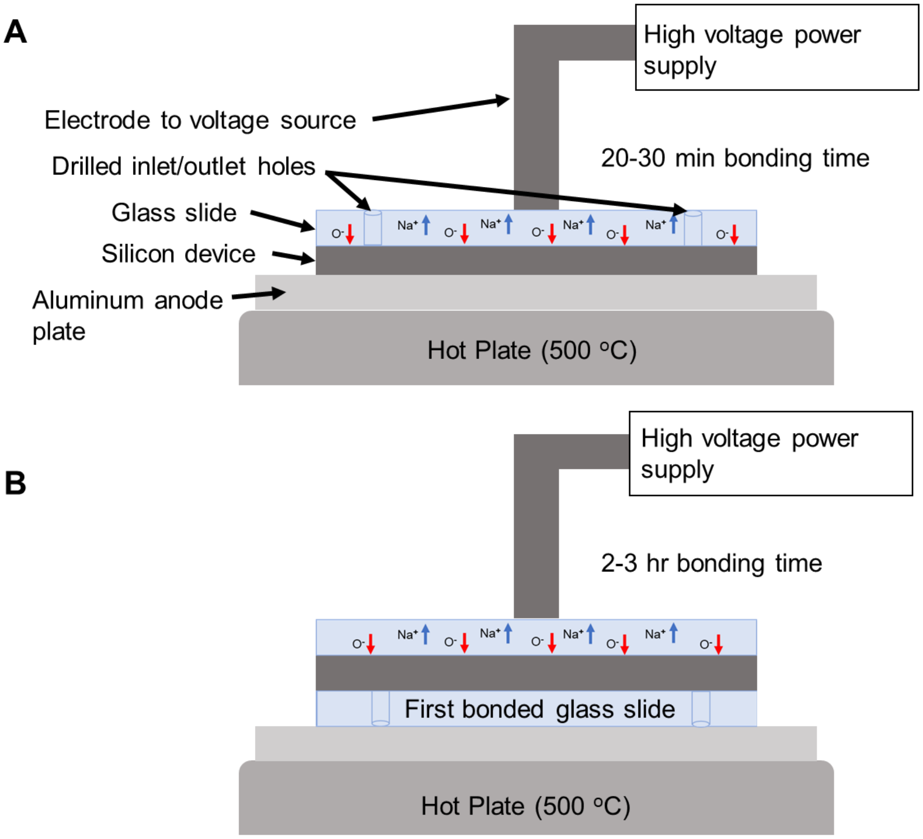

Figure 3.3. Schematic of two-sided anodic bonding. (A) First glass slide anodic bonding with electrode probe connected to voltage leads attached to high voltage source, and illustrating diffusion of Sodium (Na^+, blue arrows) and Oxygen (O^-, red arrows) ions due to applied electrical potential and high applied temperature (500 °C). (B) Second side bonding illustrating longer length of time for bonding with drilled first bonded glass slide shown underneath.

3.3.8 Anodic bonding

Anodic bonding is the process by which glass can be bonded to a substrate (e.g. silicon) using high temperatures (~500 ^oC) and an externally applied electric field. To achieve a high integrity bond between the two materials, the surfaces of both materials must have a roughness of less than 0.1 µm and be contaminant free. The piranha cleaned glass is placed atop cleaned silicon and the assembly is placed on a heating plate with an aluminum ground. A positive lead is set to the silicon and the negative lead is set to the glass for the D.C. power supply. The power supply itself is set from between 100 to 1000 volts. The bond between the two surfaces occurs due to the diffusion of sodium ions away from the glass, while oxygen radicals diffuse towards the interface between the glass and the silicon. Once the bond occurs, the process is considered irreversible, and is therefore an ideal way to achieve a tightly sealed, long-lasting microfluidic device.[33,34]

A schematic of the anodic bonding setup for both sides can be seen in Figure 3.2. To perform anodic bonding, the device and drilled cover slide were aligned and placed silica side down on an aluminum grounding plate sitting on a 500˚C (A). Lead wires were connected to the aluminum plate and negative voltage connected to the probe stand. The voltage was initially set to 100V and increased by 100V every 30 sec until a maximum of 500 V was reached. The time to fully bond the slide to the silicon surface took approximately 20-30 minutes for the first side and 2-3 hours for the second. To attach the intact glass cover slide to the other side of the device, the anodically bonded wafer and drilled glass cover slide were re-cleaned in sulfuric oxides as described above and then dried and aligned with the cleaned intact cover slide to perform anodic bonding of the second glass slide (B). The bonding can be observed to completion when the appearance of the glass to silicon interface is dark.

3.3.9 Interfacing PDMS and inlet/outlet tubing

To make the PDMS pads for attaching the inlet and outlet PEEK (polyether ether ketone) tubing, PDMS was mixed at a ratio of 10:1 pre-polymer to curing agent (respectively) and poured into the lid of a plastic petri dish to depth of 5 mm then vacuumed to remove gas bubbles and polymerized in a 100 ^{o}C oven for 5 minutes. Small squares (~1.2 x 0.75 x 0.3 cm) were cut from the PDMS layer and a 1.5 mm biopsy punch was used to form small holes in the PDMS. The assembled device and PDMS squares were then placed in a plasma cleaner (PDC-32G, Harrick Plasma) for 2 minutes. After plasma-activated bonding, the pieces were removed and the holes in each PDMS square were aligned with the drilled holes on the coverslide and stuck together. PEEK tubing was inserted into the holes on each side and the seal reinforced with epoxy resin and allowed to cure according to manufacturer’s instructions. Completed devices can be seen in Figure 3.4. Additional fabricated devices can be viewed in the supporting information for this chapter (Appendix A).

3.3.10 Unstained polystyrene acoustic particle focusing

To illustrate that acoustically focusing a sample media is possible within the widest device, we ran an initial proof of principle experiment with unstained 10 µm polystyrene particles in water (10^{6} particles/mL) in the widest device (20 mm). A 1.5 MHz transducer was attached to the device and turned on to observe how robust the acoustic focusing is. As seen in Figure 3.4, 31 discrete acoustically focused particle streams can be seen in the 20 mm device. We integrated the 2 mm wide channel device into a custom high throughput acoustic flow cytometer.[12] Written in Chapter 4 of this dissertation, we demonstrate robust signal to noise detection of fluorescent calibration beads acoustically focused in multiple parallel streams within the device.

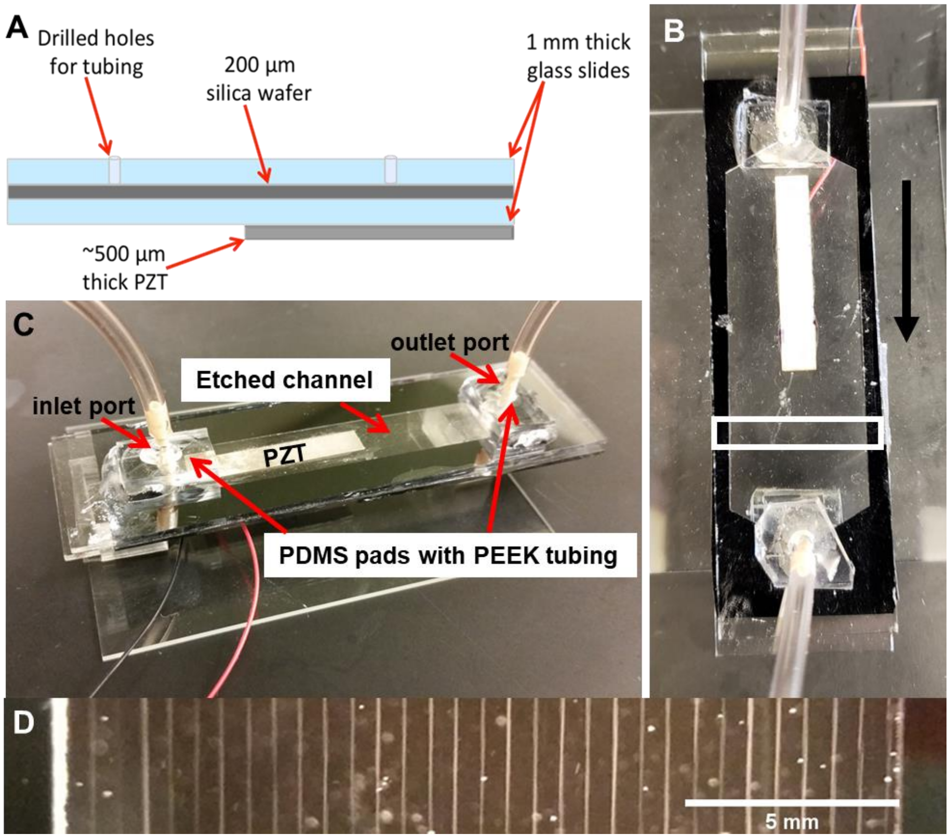

Figure 3.4. SCGFC devices and focused sample. (A) Side view illustration of the bonded borosilicate glass slide - etched silicon - borosilicate glass slide layered device with PZT and fluidic ports. (B) Top down image of 20 mm wide channel device with arrow denoting direction of flow and inset of imaging location for (D). (C) Constructed microfluidic device with 10.0 mm channel. (D) Inset region of 20 mm channel with unstained 10 µm polystyrene microspheres acoustically focused at a frequency of 1.48 MHz giving 31 discrete streams. Scale bar = 5 mm.

3.3.11 Fluorescent particle acoustic focusing and analysis

To demonstrate the efficacy of particle focusing within one of our SCGFC devices, we mixed a sample solution of ~1.0 x 10^5 particles/mL deionized water. The control run consisted of a test with no acoustic focusing while an additional experimental run recorded data during PZT actuation. This was done to compare particle positions during acoustic focusing versus free flow. The sample solution was flowed in the 2 mm wide channel device at flow rate of 2.5 mL/min and analyzed without PZT actuation. For acoustic focusing analysis, the sample solution was flowed at a rate of 2.5 mL/min with PZT actuation frequency of 4.83 MHz yielding a theoretical node count of 15. This number correlates to the number of observed acoustically focused particle streams. Results of experimental runs can be seen in Figure 3.5. Video images were collected by a sCMOS sensor in a Hamamatsu Orca flash 4.0 v2 high-speed camera (frame rate 25,655 frames/sec) and analyzed using custom Kytos Data Acquisition system, built by DarklingX (Los Alamos, NM). Each event is recorded by the brightest x-pixel position across the 2 mm channel.

For signal enhancement, 15 regions were manually input to the image analysis platform. As seen in Figure 3.5 B, the edges of each region within the unfocused experiment had an increase in particle detection due to the signal processing of the brightest pixel being edges of flowing particles in this regime. This resulted in an increased number of recorded events in edge pixels. For focused particle stream data, the number of streams correlated to the 15 generated nodes as denoted by the brightest x-pixel for each recorded event. While we observed some variation in position within the particle streams, the acoustic focusing clearly results in 15 positioned focused regions across the flow cell.

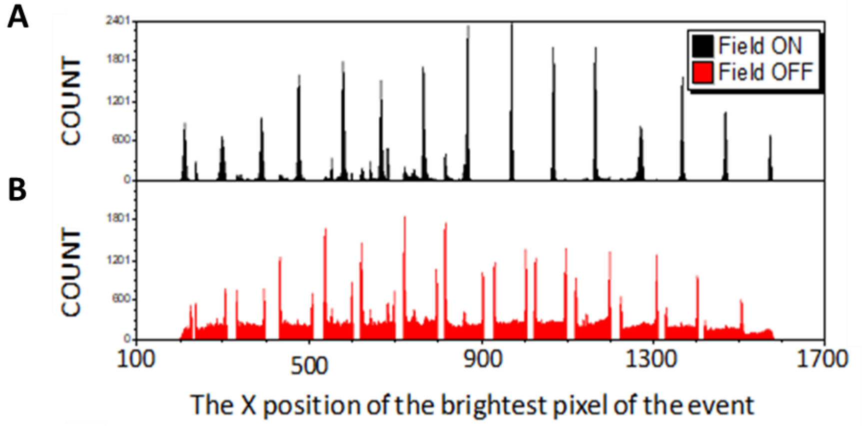

Figure 3.5. Focused and unfocused particles flowing across 2mm wide channel device. (A) Upper panel shows focused particle positions flowing through the channel at 2.5 mL/min while the acoustic field is applied. (B) lower panel is of the same region as panel A but without a resonant acoustic standing wave applied. Positions of 6 µm Nile Red particles are reported by the brightest x-pixel of each event.

3.3.12 Surface temperature measurements during laser transmittance

We measured device surface temperature of an opaque bottom channel device and compared it to an optically transparent device in 15-minute intervals over 3 hours during laser transmittance. We conclude that no measurable temperature difference was measured at the surface of the device. The hypothesis of device heating may occur as a localized effect on the channel surface or in the fluid, but more work needs to be done to better investigate this case. Further details on this component of our work can be seen in supporting information for this chapter (Appendix A).

3.4 Conclusions

There is a growing need for rapid diagnostic tools in the medical field. The development of improved acoustofluidic devices for accurate and sensitive particle analysis is critical because cells and multiplex microparticles are important for early diagnosis and treatment of diseases. Here, we illustrate the processes required to fabricate silicon core, double-glass capped, optically clear flow chambers for high volume acoustofluidic applications. The devices presented here experienced no visible light scatter, as the light transmits through the device, and even though the opaque bottom devices exhibited negligible temperature change over 3 hr. (Appendix A), the optically transparent channels did not as well. In addition to the optical transparency of our devices, we demonstrate the capability to acoustically focus multiple parallel streams at high volumetric flow rates (2.5 ml/min versus conventional 25 µL/min). Therefore, we conclude that this rapid and cost-effective method for fabricating optically clear wide channel devices is an excellent tool for acoustofluidic applications where optics are required for media interrogation.

3.5 Acknowledgements

We gratefully acknowledge funding from the National Institutes of Health award number R21GM107805. We would like to thank John Nogan and the staff at the Center for Integrated Nano Technologies as well as Harold Madsen at the Manufacturing Training and Technology Center at UNM for their training and assistance in the clean room techniques for silicon device processing.

3.6 References

(1) Hammarström, B.; Evander, M.; Barbeau, H.; Bruzelius, M.; Larsson, J.; Laurell, T.; Nilsson, J. Non-Contact Acoustic Cell Trapping in Disposable

Glass Capillaries. *Lab on a Chip.* 2010, *10* (17), 2251–2257.

(2) Lenshof, A.; Evander, M.; Laurell, T.; Nilsson, J. Acoustofluidics 5: Building Microfluidic Acoustic Resonators. *Lab on a Chip.* 2012, *12* (4), 684.

(3) Ueha, S.; Hashimoto, Y.; Koike, Y. Non-Contact Transportation Using near-Field Acoustic Levitation. *Ultrasonics.* 2000, *38* (1), 26–32.

(4) Clark, M.; Sharples, S.; Somekh, M. Non-Contact Acoustic Microscopy. *Measurement Sciences Technology.* 2000, *11* (12), 1792–1801.

(5) Lenshof, A.; Magnusson, C.; Laurell, T. Acoustofluidics 8: Applications of Acoustophoresis in Continuous Flow Microsystems. *Lab on a Chip.* 2012, *12* (7), 1210.

(6) Yasuda, K.; Haupt, S. S.; Umemura, S.; Yagi, T.; Nishida, M.; Shibata, Y. Using Acoustic Radiation Force as a Concentration Method for Erythrocytes. *Journal of Acoustical Society of America.* 1997, *102* (c), 642–645.

(7) Johnson, L. M.; Gao, L.; Shields IV, C.; Smith, M.; Efimenko, K.; Cushing, K.; Genzer, J.; López, G. P. Elastomeric Microparticles for Acoustic Mediated Bioseparations. *Journal of Nanobiotechnology.* 2013, 11 (1), 22.

(8) Nilsson, A.; Petersson, F.; Jönsson, H.; Laurell, T. Acoustic Control of Suspended Particles in Micro Fluidic Chips. *Lab on a Chip.* 2004, *4* (2), 131–135.

(9) Williams, P. S.; Martin, M.; Hoyos, M. Acoustophoretic Mobility and Its Role in Optimizing Acoustofluidic Separations. *Analytical Chemistry.* 2017, *89* (12), 6543–6550.

(10) Shapiro, H. *Practical Flow Cytometry Fourth Edition*; John Wiley & sons, inc. 2004, 166-178.

(11) Piyasena, M. E.; Austin Suthanthiraraj, P. P.; Applegate, R. W.; Goumas, A. M.; Woods, T. A.; López, G. P.; Graves, S. W. Multinode Acoustic Focusing for Parallel Flow Cytometry. *Analytical Chemistry.* 2012, *84* (4), 1831–1839.

(12) Kalb, D. M.; Fencl, F. A.; Woods, T. A.; Swanson, A.; Maestas, G. C.; Juárez, J. J.; Edwards, B. S.; Shreve, A. P.; Graves, S. W. Line-Focused Optical Excitation of Parallel Acoustic Focused Sample Streams for High Volumetric and Analytical Rate Flow Cytometry. *Analytical Chemistry.* 2017, 89 (18), 9967–9975.

(13) Goddard, G.; Martin, J. C.; Graves, S. W.; Kaduchak, G. Ultrasonic Particle-Concentration for Sheathless Focusing of Particles for Analysis in a Flow Cytometer. *Cytometry Part A.* 2006, *69* (2), 66–74.

(14) Di Carlo, D. Inertial Microfluidics. *Lab on a Chip*. 2009. 9(21), 3038-46

(15) Gor’kov, L. P. Forces Acting on a Small Particle in an Acoustic Field within an Ideal Fluid. *Doklady Akademii Nauk SSSR.* 1961, *140* (1), 88–91.

(16) Shi, J.; Ahmed, D.; Mao, X.; Lin, S. C. S.; Lawit, A.; Huang, T. J. Acoustic Tweezers: Patterning Cells and Microparticles Using Standing Surface Acoustic Waves (SSAW). *Lab on a Chip.* 2009. 9, 2890-2895

(17) Shi, J.; Mao, X.; Ahmed, D.; Colletti, A.; Huang, T. J. Focusing Microparticles in a Microfluidic Channel with Standing Surface Acoustic Waves (SSAW). *Lab on a Chip.* 2008. 8, 221-223.

(18) Liu, S.; Yang, Y.; Ni, Z.; Guo, X.; Luo, L.; Tu, J.; Zhang, D.; Zhang, and J. Investigation into the Effect of Acoustic Radiation Force and Acoustic Streaming on Particle Patterning in Acoustic Standing Wave Fields. *Sensors.* 2017, *17* (7), 1664.

(19) Torr, G. R. The Acoustic Radiation Force. *American Journal of Physics.* 1984, 52 (5), 402.

(20) Verbeni, R., et al. Quantum Effects in the Dynamics of He Probed by Inelastic X-ray Scattering. *Physical Reviews*. 2001, E 64(2): 021203.

(21) Bruus, H. Acoustofluidics 7: The Acoustic Radiation Force on Small Particles. *Lab on a Chip.* 2012, *12* (6), 1014.

(22) Lenshof, A.; Evander, M.; Laurell, T.; Nilsson, J. Acoustofluidics 5: Building Microfluidic Acoustic Resonators. *Lab on a Chip.* 2012, *12* (4), 684.

(23) Lenshof, A., et al. Acoustofluidics 8: Applications of Acoustophoresis in Continuous Flow Microsystems. *Lab on a Chip*. 2012, 12 (7), 1210-1223.

(24) Ruby, R. Review and Comparison of Bulk Acoustic Wave FBAR, SMR Technology. In *Proceedings - IEEE Ultrasonics Symposium*. 2007, 1029–1040.

(25) Kundt, A. III. Acoustic Experiments. *London, Edinburgh, Dublin Philosophical Magazine and Journal of Science.* 1868, *35* (234), 41–48.

(26) Piyasena, M. E.; Graves, S. W. The Intersection of Flow Cytometry with Microfluidics and Microfabrication. *Lab on a Chip.* 2014, *14* (6), 1044–1059.

(27) Gautam, G. P.; Burger, T.; Wilcox, A.; Cumbo, M. J.; Graves, S. W.; Piyasena, M. E. Simple and Inexpensive Micromachined Aluminum Microfluidic Devices for Acoustic Focusing of Particles and Cells. *Analytical and Bioanalytical Chemistry.* 2018, *410* (14), 3385–3394.

(28) Laerme, F.; Schilp, A.; Funk, K.; Offenberg, M. Bosch Deep Silicon Etching: Improving Uniformity and Etch Rate for Advanced MEMS Applications. In *Technical Digest. IEEE International MEMS 99 Conference. Twelfth IEEE International Conference on Micro Electro Mechanical Systems (Cat.*

No.99CH36291). 1999, 211–216.

(29) Rajiv Kohli, K. L. M. Developments in Surface Contamination and Cleaning, Vol. 1: Fundamentals and Applied Aspects. *William Andrew*. 2015, 354.

(30) Campbell, P.; Green, M. A. Light Trapping Properties of Pyramidally Textured Surfaces. *Journal of Applied Physics.* 1987, *62* (1), 243–249.

(31) Yahaya, N. A.; Yamada, N.; Kotaki, Y.; Nakayama, T. Characterization of Light Absorption in Thin-Film Silicon with Periodic Nanohole Arrays. *Optics Express.* 2013, *21* (March), 5924–5930.

(32) Eyderman, S.; John, S.; Hafez, M.; Al-Ameer, S. S.; Al-Harby, T. S.; Al-Hadeethi, Y.; Bouwes, D. M. Light-Trapping Optimization in Wet-Etched Silicon Photonic Crystal Solar Cells. *Journal of Applied Physics.* 2015, *118* (2). 023103.

(33) Wallis, G.; Pomerantz, D. I. Field Assisted Glass-Metal Sealing. *Journal of Applied Physics.* 1969, *40* (10), 3946–3949.

(34) Wallis, G. Field Assisted Glass Sealing. *Electrocomponent Science and Technology.* 1975, *2* (1), 45–53.

Chapter 4: Line-focused Optical Excitation of Parallel Acoustic Focused Sample Streams for High Volumetric and Analytical Rate Flow Cytometry

Daniel M. Kalb,[1] Frank A. Fencl,[1] Travis A. Woods, [1] August Swanson,[2] Gian C. Maestas,[1] Jaime J. Juárez,[3] Bruce S. Edwards,[4] Andrew P. Shreve,[1] and Steven W. Graves[1]

[1] Department of Chemical and Biological Engineering, Center for Biomedical Engineering, MSC01 1141 1 University of New Mexico, Albuquerque, NM 87131

[2]DarklingX, Los Alamos National Laboratory, MS J567, C-PCS, Los Alamos, NM 87545, USA

[3]Iowa State University, Mechanical Engineering, 2020 Black Engr, Ames IA 50011

[4]Center for Molecular Discovery, Innovation Discovery and Training Center, Health Sciences Center, University of New Mexico, Albuquerque, New Mexico, 87131-0001 United States

Author contributions

The primary author of this work is Daniel M. Kalb. My contribution here as the second author is in the design, fabrication and testing of the optically clear acoustic flow chamber. I did extensive image analysis to ascertain the dimensions of the channel necessary for the theoretical calculation of acoustic pressure nodes present which correlate to the number of acoustically focused streams. I also assisted in the optics setup for the custom flow cytometer and in development of the publication accepted in *Analytical Chemistry*. With the approval of Dr. Steven W. Graves (the corresponding author) and my dissertation committee, we have decided this body of work should be included in my dissertation.

4.1 Abstract

Flow cytometry provides highly sensitive multi-parameter analysis of cells and particles but has been largely limited to the use of a single focused sample stream. This limits the analytical rate to ~50K particles/s and the volumetric rate to ~250 µl/min. Despite the analytical prowess of flow cytometry, there are applications where these rates are insufficient, such as rare cell analysis in high cellular backgrounds (e.g. circulating tumor cells and fetal cells in maternal blood), detection of cells/particles in large dilute samples (e.g. water quality, urine analysis), or high throughput screening applications. Here we report a highly parallel acoustic flow cytometer that uses an acoustic standing wave to focus particles into 16-17 parallel analysis points across a 2.3-mm wide optical flow cell. A line focused laser and wide-field collection optics are used to excite and collect the fluorescence emission of these parallel streams onto a high-speed camera for analysis. With this instrument format and fluorescent microsphere standards, we obtain analysis rates of 100K/s and flow rates of 10 mL/min, while maintaining optical performance comparable to that of a commercial flow cytometer. The results with our initial prototype instrument demonstrate that the integration of key parallelizable components, including the line focused laser, particle focusing using multi-node acoustic standing waves, and a spatially arrayed detector, can increase analytical and volumetric throughputs by orders of magnitude in a compact, simple and cost-effective platform. Such instruments will be of great value to applications in need of high throughput yet sensitive flow cytometry analysis.

4.2 Introduction

A typical flow cytometer sensitively measures up to twenty optical parameters from individual cells on a cell-by-cell basis at analytical rates as high as ~50,000 cells/s and volumetric rates of up to 250 µl/min.[1, 2] This analytical power makes it the technology of choice for many applications including cellular phenotyping (e.g. CD4+ T-cell counts), cell cycle analysis, and apoptosis measurements.[1, 2] Additionally, flow cytometry is valuable for rare cell detection,[3-6] high throughput screening for pharmaceutical lead compounds,[7-9] analysis of environmental samples for algae, plankton, other microbes,[10-12] and as a method of process monitoring for food safety.[13] However, use of flow cytometry for high throughput applications is limited by the analytical and volumetric rates. Increasing these rates would reduce the need for cell enrichment strategies for rare cell applications, improve the rate of high throughput screening, and increase the likelihood of detection of microbes or algae of interest in both food safety and environmental applications.

Analytical and volumetric rate limitations in conventional flow cytometers are largely due to the analytical paradigm that uses a tightly focused laser to interrogate a single focused stream of particles or cells.[2] In a conventional flow cytometer the laser spot is focused to an elliptical spot (~10 µm high by 50 µm wide) that interrogates a sample stream that is focused by a high velocity sheath fluid to a core diameter of only a few microns.[2, 14] This approach allows a cell or particle to occupy most of the interrogation volume (~ 1 pL) as it passes through the focused spot of the laser. This enables a wash-free sensitive measurement, which is a critical analytical advantage for flow cytometry compared to other techniques. The high analytical rate of a flow cytometer is achieved in part by flowing sample at linear velocities up to 10 m/s. The onset of turbulence precludes higher linear velocities.[14]

These limitations on linear velocity and the width of the sample stream restrict the volumetric throughput of a hydrodynamic focusing flow cytometer. However, the volumetric throughput of a cytometer can be increased by means other than increasing the overall velocity of the system if tight particle focusing can be achieved using a different approach. One such approach uses acoustic standing waves to focus particles in a cylindrical capillary upstream of the analysis point. Acoustic focusing enables sample delivery rates of about 1 ml/min, while maintaining the precision measurements typical of a flow cytometer.[15-17] Much like a conventional flow cytometer, this method analyzes the particles in a single stream, therefore the analytical rate of both these methods is limited by coincident events occurring due to the stochastic arrival of cells in the interrogation volume.[14, 16, 17]

The limitations of single sample stream flow cytometers have led to the development of parallel stream flow cytometers to increase volumetric and analytical event rates. Most parallel flow cytometer systems rely on hydrodynamics or tight microfluidic channels to create parallel focused streams of particles for analysis. Modestly parallel systems have been constructed using simple multiplexing of conventional fluidics and optics to create systems of up to 4 flow streams with overall analysis rates of ~250,000 particles/s.[18] Alternatively, microfluidic approaches have led to hydrodynamically focused flow cytometers with 24 parallel sample streams that have sample delivery rates of up 830 μl/min and analytical rates of 240,000 cells per second.[19] Though these systems, which are commercially available, do show improved throughput compared to a conventional flow cytometer they are very large, relatively expensive, and significantly more complex than standard flow cytometers.[19] Additional work has demonstrated parallel analysis through the use of up to four inexpensive flow cytometers operating in parallel to increase the sampling rate of high-throughput screening (HTS) flow cytometry systems.[20] This technique shows promise, but it demonstrates the need to decrease the cost per analysis point/cytometer (currently ~$50K) to maximize the effectiveness of this approach.[20]

As much of the bulk and complexity of parallel cytometer systems is due to the hydrodynamic focusing, inertial focusing in parallel microfluidic channels may also offer a path to highly parallel flow cells.[21] However, this approach requires channels only slightly wider than the particles, which requires care to prevent clogging and limited volumetric throughput.

By contrast, multinode acoustic standing waves offer a highly parallel and high throughput method to tightly focus flowing particles for analysis or separations without the use of microfluidic channels.[2, 22] At a resonant frequency condition, an integer number of half-wavelengths are excited across the focusing plane of the channel. The superposition of the reflecting waves within the focusing chamber creates an acoustic standing wave. The magnitude of the primary acoustic force on a particle within an acoustic standing wave system depends upon the pressure of the standing wave, the applied frequency, the position within the wave, the volume of the particle and the relative properties of the media and particle described by an acoustic contrast factor. Prior results using such standing waves demonstrate the ability to create highly parallel acoustic flow cells that support up to 37 discrete focused streams in a single channel[23] and up to 300 focused streams in a multichannel microfabricated flow cell.[24] Additionally, the wide aspect ratio and correspondingly large cross-sectional area of these flow cells reduces clogging and allows for sheathless, precise, and highly parallel focusing of particles at low linear velocities, but high volumetric throughputs (25 mL/min).[24]

Based on these considerations, we present here a fundamentally new methodology for parallelizing high throughput flow cytometry analysis. Integrating a highly parallel acoustic focusing flow cell, a line focused excitation laser, wide field collection optics, and a spatially arrayed detector creates a relatively simple, high performance instrumentation platform with both high volumetric delivery rates and high analytical rates. We discuss the scalability of this approach and the value of this work for flow cytometry applications requiring high volumetric sample delivery rates or high analytical rates.

4.3 Materials and methods

4.3.1. Multinode acoustic flow cell

Device design. The acoustic flow cell used for this study is fabricated in house. A 200 μm thick silicon wafer is etched completely through across an area of ~2,300 μm width by 5 cm length and anodically bonded with glass on both sides to create a 2,300 μm x 200 μm x 5 cm transparent channel (W x H x L) (Figure 4.1 A, B). The transparent flow chamber minimizes excess heat and optical scatter that would otherwise occur due to absorption and scattering from an opaque silicon background.

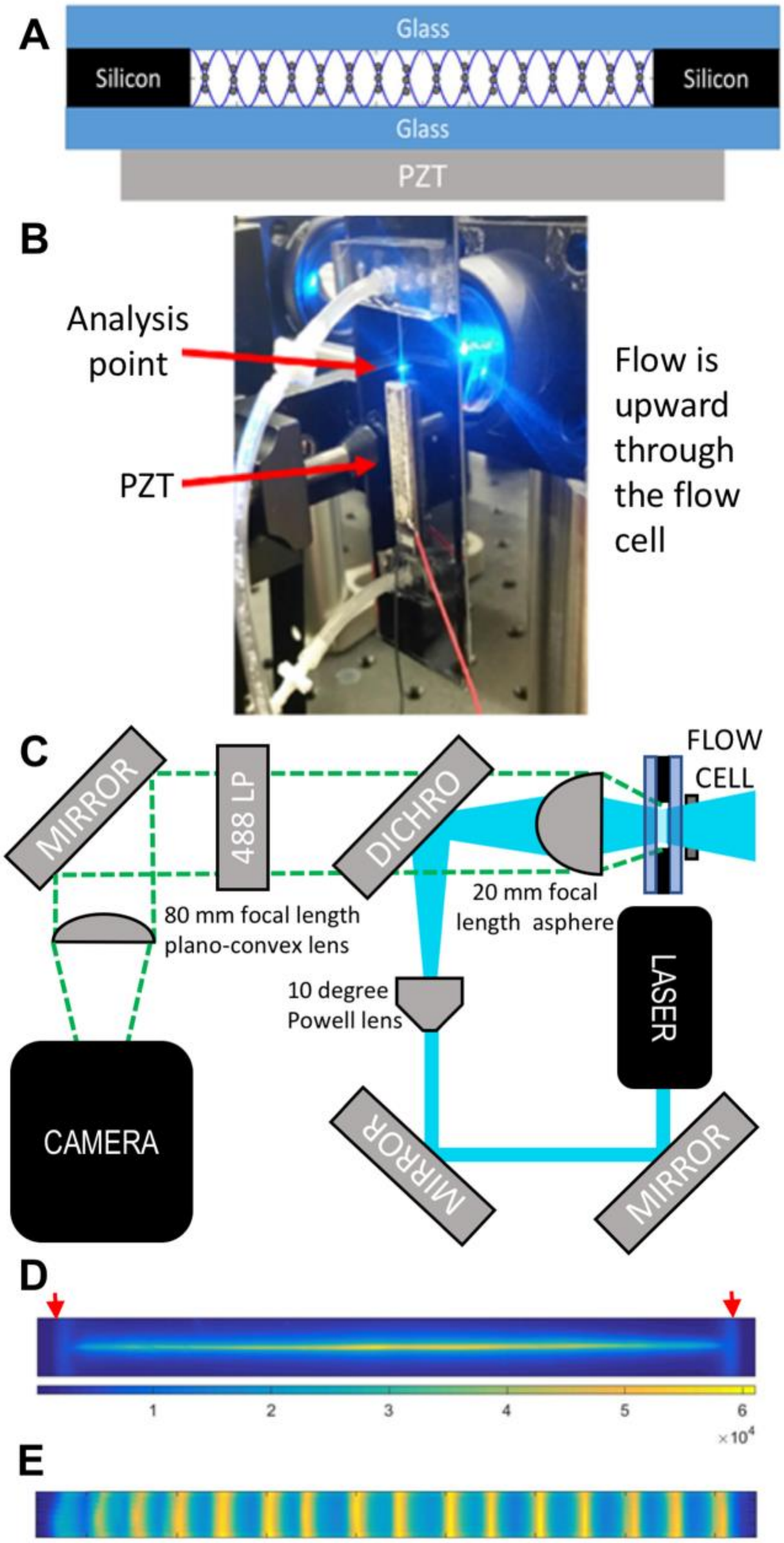
A
Glass
Silicon
Silicon
Glass
PZT
B
Analysis point
PZT
Flow is upward through the flow cell
C
MIRROR
488 LP
DICHRO
FLOW CELL
80 mm focal length plano-convex lens
20 mm focal length asphere
10 degree Powell lens
LASER
CAMERA
MIRROR
MIRROR
MIRROR
D
1
2
3
4
5
6
×10⁴
E

Figure 4.1. System description. (A) Cross-sectional schematic of the acoustic focusing flow cell. The standing acoustic pressure wave (sine wave) focuses particles to the 16 pressure nodes across the width of the flow cell. (B) Image of the mounted flow cell. (C) Schematic of optics. (D) Laser excitation profile. The red arrows show the positions of the walls, that were 2.3 mm apart. (E) Stacked image of acoustically focused fluorescent particles.

Photolithography and deep reactive-ion etching (DRIE). Using a 10 cm silicon substrate wafer, AZ 4620 positive photoresist is spin coated to form a uniform 6-10 µm layer. The spin-coated wafer is developed and washed before etching. A 90-minute Bosch process is used to etch through the device. Once the device is processed through the DRIE, it is left in acetone for 1-2 hours (or as needed) to dissolve the remaining photoresist, rinsed with DI water and dried with N_2. The etched silicon is then piranha-cleaned prior to the anodic bonding process.

Anodic-bonding. The cleaned silicon device is placed on an aluminum plate on top of a ceramic hot plate. A piranha cleaned glass slide is placed flush on top of the silicon device. The silicon wafer is connected to the (-) output and the glass slide is connected to the (+) output of a DC power supply. The hot plate is set to 500^0C. After temperature equilibration, the voltage is increased from 100V to 800V over ~4 minutes. Successful bonding is indicated by a color change of the glass to silicon contact area. Once bonding is complete, the procedure is repeated on other side of the device. Each side takes 3-6 hours to bond, resulting in a sandwiched silicon etched device between two borosilicate glass slides (Figure 4.1A). Punctured polydimethylsiloxane (PDMS) seals the fluidic connections made via polyether ether ketone (PEEK) tubing.

Transducer selection and attachment. A 4.48 MHz PZT (30 x 5 mm, APC

International, Mackeyville, PA) is superglued under the channel and driven at 5.08 or 5.32 MHz, to create 16 or 17 pressure nodes (Figure 4.1A). This agrees with the predicted number of nodes (n) using a half-wavelength resonance condition $n = 2Lf/c$, where c is the speed of sound (~1490 m/s), L is the width of the flow cell (2.3 mm), and f is the drive frequency.

4.3.2. Optical setup

The flow cell is placed in front of the aspheric lens that serves as both the collection lens and focusing lens in an epifluorescent configuration (Figure 4.1B). The full optical schematic is shown in Figure 4.1C. Excitation is provided by a beam from 150 mW 488 nm laser (Mini-WhisperIT, Pavilion Integration Corporation, San Jose CA) steered by two mirrors through a 10 degree Powell lens (Laserline Optics Canada Inc, Canada) onto a reflective 488 nm dichroic beamsplitter (Semrock, Rochester, NY) to create a line-shaped excitation beam that is focused into the acoustic flow cell using a 25 mm diameter aspheric lens with a 20 mm focal length (AL2520-A, ThorLabs, Inc. Newton, NJ) (Figure 4.1C). The analysis position is just above the PZT (Figure 4.1B). The emitted light is collected back into the aspheric lens, passed through the beamsplitter, filtered with a 488 nm long-pass filter (488nm Edge Basic, Semrock, Rochester, NY), and imaged onto an sCMOS sensor (Hamamatsu Orca flash 4.0 v2) using a 25 mm diameter plano-convex lens with an 80-mm focal length. At the sample illumination point, the line-shaped excitation beam, detected via emission of Fluorescein dye solution in the flow cell, (Figure 4.1D) has dimensions of ~2.3 mm width and ~10-20 μm height, matching both the width of the flow cell and the active area (8 x 2048 pixels) of the camera’s field of view when the camera is operated at it maximum acquisition rate of 25,655 frames per second. To visually display the streams in flow, 75K frames were taken over 3 seconds of acoustically focused fluorescent particles flowing through active region of the camera. The frames were summed and averaged into a single 8 x 2048 aggregate frame. This aggregate frame has been stretched 20x vertically to more easily visualize focused positions of particles in the flow cell (Figure 4.1E).

4.3.3. Analysis of frames data

Two data collection methods are used for the high-speed camera data from the Hamamatsu Orca Flash 4.0 v2 (operated at 25,655 frames/s or ~39 μs exposure). The full uncompressed raw data from the camera (6.7 Gb/s) is stored either on the hard drive for post processing in MATLAB or analyzed in real-time using a custom data acquisition package (Kytos Data Acquisition system, built by DarklingX, Los Alamos, NM). The stored raw data files allow for detailed analysis and a means of testing image analysis algorithms, while the Kytos acquisition system provides substantial real-time information compression of the data to generate standard flow cytometry data sets.

Figure 4.2 (panels A & B), shows stored image data acquired by the sCMOS detector after post-experiment processing. In panel A, the long axis of the detector is presented along the vertical figure axis, while sequential frames of pixels 2 through 7 of the short axis of the detector window are presented from left to right. Only pixel rows 2-7 were used for analysis of the frame data indicated due to increased noise in pixel rows 1 and 8. Each bright streak corresponds to a particle traversing the excitation beam. In the magnified image shown in panel B, one can see sequential frames 1 through 18. The particle enters the detection window from the right in frame 3, traverses through, and exits to the left in frame 16. In the real-time acquisition mode (Figure 4.2C), the user first defines regions of interest (typically 50 - 100 pixels wide) corresponding to the position of the 16 or 17 focused streams. To create 16 or 17 discreet detection areas, each region of interest is monitored individually in each frame, and event triggering in each region occurs by comparison with a user-defined threshold level in one of two possible modes. In a peak intensity mode, the largest single pixel value, averaged with its eight nearest neighbors, must exceed the user-defined threshold. In an integrated mode, the integral of all pixels in the region of interest must exceed the user-defined threshold. Around each event trigger, several frames of the region of interest are analyzed to provide signal parameters in real time. Several measurement parameters are collected. The parameters used primarily for this work were the peak intensity parameter, which is the single brightest pixel from a particle's traverse through the laser beam and the peak integrated intensity parameter, which is defined as the maximum integrated pixel value of a single frame within a particle's time of flight through the laser beam. Additional parameters extracted include the column or X position of the brightest pixel of an event (BPX), the time of flight (number of frames) through the laser, the frame number, and the event number. Beyond these values, the integrated fluorescent intensity for each event is stored as a waveform across several frames (Figure 4.2C). The frames included are all frames in which signals are above the chosen threshold value described above, as well as several pre-event frames extracted from buffered data and several post-event frames. While not used here, waveforms fit to a Gaussian can be used to eliminate irregular events such as doublets and the fit parameters (Amplitude, R^2, and standard deviation) used to further quantify the fluorescent parameters. Singlet waveforms have a high R^2 and outliers (doublets) can be excluded based on R^2 values.

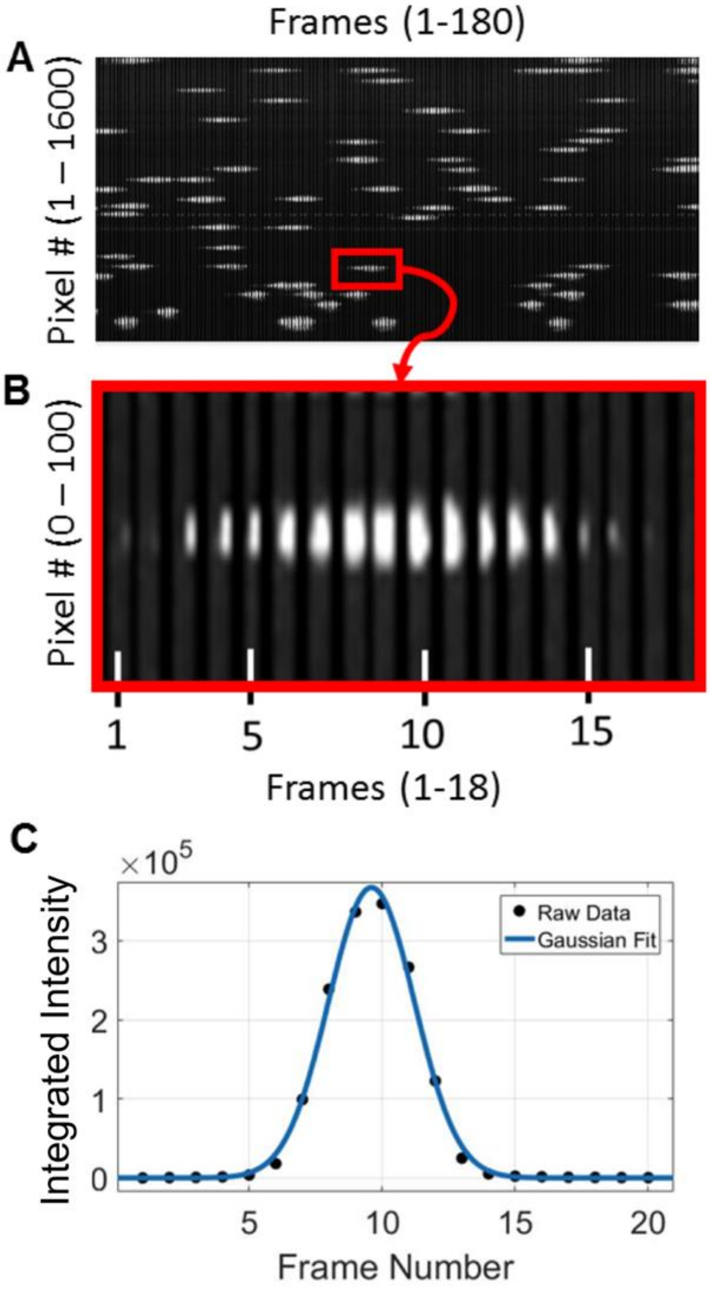

Figure 4.2. Image analysis of camera data. (A) Pseudo image of fluorescent intensity of particles traveling across the entire camera width. Data displayed are a sequence of ~180 frames presented along the horizontal axis. Each of these ~180 sequential frames displays a single image. Only rows 2-7 of each frame's 8 pixel height are shown. (B) Intensity pseudo-image showing a single particle going through the laser excitation. Each of the 18 frames consists of a 6 by 100 pixel image. A small width spacing (completely black in color) is introduced between each of these frames to make them individually distinguishable. (C) Waveform and Gaussian fit of the integrated fluorescent intensity of a single particle going through the laser excitation.

Notably, our approach does not require precise flow control or optical tracking approaches used in image cytometry approaches.[25, 26] Rather, we are simply using the sCMOS detector as an approximate 1D array that simplifies direct collection of data across a wide field of view.

4.3.4. FCS data analysis

After acquisition, data are stored in flow cytometry format and analyzed using a commercial software package (FCS Express, De Novo Software, Glendale, CA).

4.4 Results

4.4.1. Acoustic focusing ON/OFF

Like all flow cytometers, the performance of our system depends upon having a consistent interaction between the particle and the interrogating laser. Thus, the use of acoustic focusing within the flow cell greatly improves the system's performance, leading to very predictable and consistent particle/laser interactions across all of the focused streams. Figure 4.3A shows the variation observed in the positioning of the particles across one stream of a multinode parallel acoustic flow cell with the acoustic focusing field OFF and ON. It is clear that focusing provides tight lateral positioning within a given sample stream, as the X position of the brightest pixel (BPX) is much more tightly distributed when the acoustic field is on. Similar performance is seen across all streams in a parallel flow cell (Supporting information for this chapter can be seen in Appendix B). For data analysis purposes, the data acquisition system defines a range of pixels as a stream, e.g. from 1020 to 1090 for stream 10 in Figure 4.3A. The large number of events on the edge of the window results from any partial event at the edge of window being recorded with a BPX value of the edge pixel value, which biases the histogram data as any event in the unfocused data that just clips the window is recorded as the last pixel of the window. For the data in Figure 4.3, 16 streams were defined and each event is assigned both a BPX value, based on where its brightest pixel occurred on the sensor, and a stream number based on which stream window it appeared in (Appendix B). As each event within a stream window is identified with a stream number, it is simple to correlate events based on the stream and for events in each stream to be analyzed separately. Our results show that a similar number of particles are found in each of the 16 focused streams (Appendix B).

Using standard flow cytometry gating approaches on the stream parameter, we can analyze the fluorescence peak intensity of events from a given stream in focused and unfocused states (Figure 4.3B). There is a large increase in system performance in terms of both fluorescence precision (unfocused 76% CV, focused 6% CV) and optical collection (mean intensity is brighter for focused particles) when the acoustic field tightly focuses the particles. Within a given stream, the particle positions clearly differ in focused and unfocused scenarios (Figure 4.3A). As such, much of the broadening of the optical collection of the unfocused beads population might be due to the variation across the 1D width of the laser excitation profile.

The non-uniform laser excitation (Figure 4.1D) and the difficulty of efficiently collecting light over a wide field of view creates variation in the fluorescent intensity profile across the 16 focusing regions. Nonetheless, it can be seen that unfocused particles have significantly lower precision (Figure 4.3C) as compared to focused particles (Figure 4.3D), regardless of stream position. Though there is variation in optical excitation and collection efficiency, the benefit of focusing is clear. In future work, a per-channel gain could be applied to normalize across streams. On an optimized system where the laser profile and the Powell lens are fully matched, it is expected that ~5% variation along the focused laser line could be achieved.

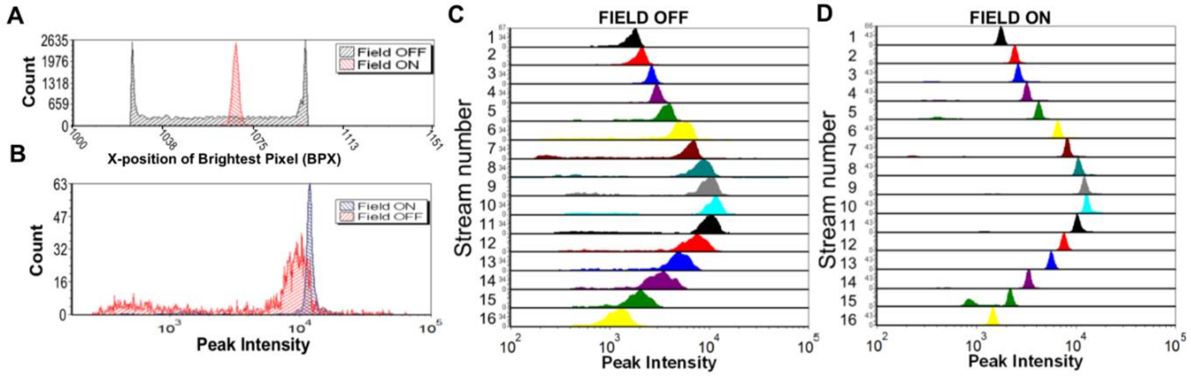

Figure 4.3. Acoustic focusing increases system performance. (A) Histogram of the position of particles across stream 10 of a flow cell supporting 16 acoustic focusing nodes. When the field is on (red) the focusing is clear as particles appear in a tight Gaussian distribution, whereas when the focusing is off (black) the particles are broadly distributed across the collection window (B) Histogram of the fluorescence peak intensity for a single focusing stream (stream 10), with the focusing field on (blue) and off (red). (C & D) Stacked histogram of the peak intensity of the particles across all 16 focusing regions with the acoustic focusing field off (C) and on (D).

4.4.2. Evaluation of optical sensitivity and resolution

Eight peak ultra-rainbow calibration beads (3μm diameter, RCP-30-5A Spherotech, Lake Forest, IL) are used as a calibration standard to characterize the performance of the parallel cytometer. Figure 4.4A shows the optical performance across 17 focusing nodes. While full resolution of the calibration beads is seen in the center of the channel where both the laser excitation and optical collection efficiency are highest, only the brightest 4-5 populations are seen at the edges where the laser excitation is lowest and the optical collection is least efficient. Looking at the highest performing stream (stream 10), seven fluorescent peaks are clearly visible with good population separation and CV's comparable to those acquired on a commercial cytometer (~3-6%) (Figure 4.4B). An observed eighth population might correspond to blank beads, but further work is needed to confirm this conclusion. Similar performance was seen with 6 μm Rainbow calibration beads (Appendix B).

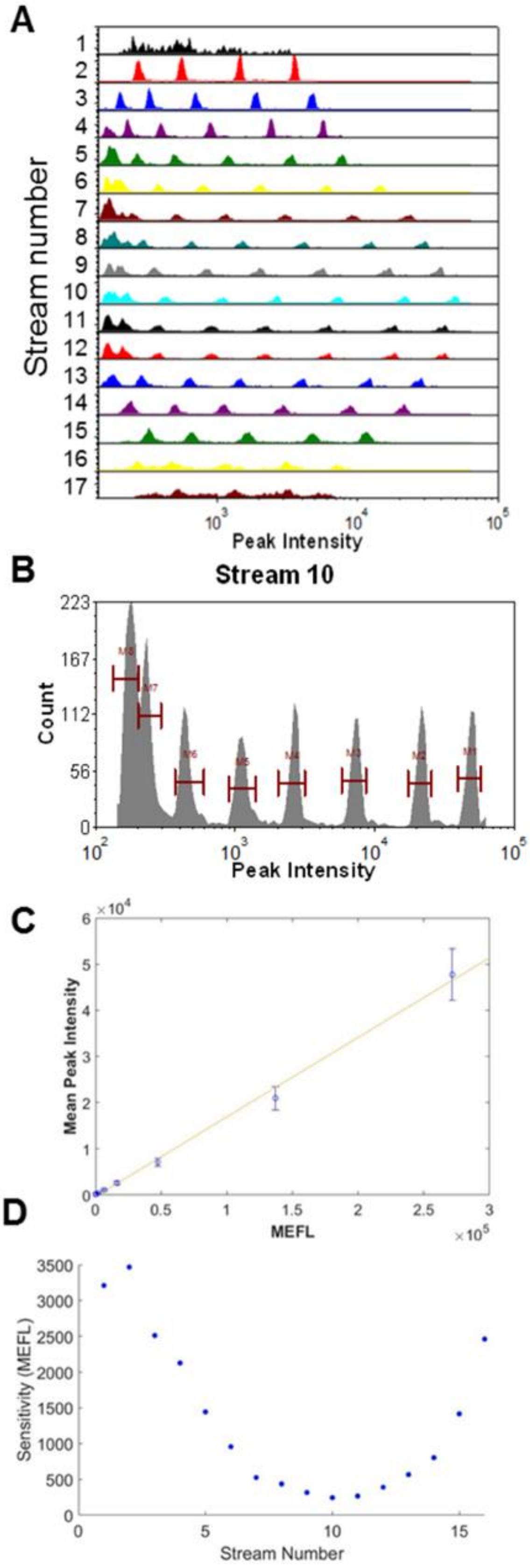
A
Stream number
1
2
3
4
5
6
7
8
9
10
11
12
13
14
15
16
17
10^3
10^4
10^5
Peak Intensity
B
Stream 10
Count
223
167
112
56
0
M8
M7
M6
M5
M4
M3
M2
M1
10^2
10^3
10^4
10^5
Peak Intensity
C
$\times 10^4$
6
5
4
3
2
1
0
Mean Peak Intensity
0
0.5
1
1.5
2
2.5
3
MEFL
$\times 10^5$
D
3500
3000
2500
2000
1500
1000
500
0
Sensitivity (MEFL)
0
5
10
15
Stream Number

Figure 4.4. Eight peak rainbow beads. (A) Histogram of the peak intensity for all 17 streams. (B) Histogram of peak intensity for a stream 10 (C) Mean peak intensity of each bead population in stream 10 plotted vs. the estimated mean equivalent number of Fluorescein molecules per bead. Error bars are the standard deviation of each bead population. (D) Current maximum sensitivity to a threshold that is two standard deviations above the background noise of the system.

In this study, we also find that increasing the applied laser power increases the sensitivity across the entire channel width (Appendix B). Our current laser power per area (150 mW over 20 μm x 2000 μm) is ~5X less than that used by a typical flow cytometer (20 mW over 20μm x 50 μm). This observation suggests that we are far from any power saturation effects, so fluorescence sensitivity should increase with higher applied laser power. Thus, full resolution of all bead populations in all streams may be possible with a higher power laser well matched to the Powell lens.

Using the microsphere standards, we see that our system has a linear response when plotted as estimated Molecules of Equivalent Fluorescein (MEFL) vs fluorescence peak intensity. It is important to point out that these commercial beads are stained with various dyes, across the spectra such that that our optical system (488 nm long pass) is not directly comparable to a standard FITC channel on a cytometer (530/30 Bandpass). Thus, any quantities estimates of MEFL at this point would potentially overestimate the sensitivity of the system. Despite this fact, the standard curve of peak intensity vs. estimated MEFL shows high linearity that demonstrates the quantitative potential of the system (Figure 4.4C). At the center of our system we can clearly resolve the dimmest fluorescently tagged bead, giving us a sensitivity of 792 MEFL or better. An interpolation of the sensitivity down to a level limited by the background signal plus system noise (background level plus 2 times the standard deviation of the background) suggests the sensitivity for the highest performing stream is a few hundred MEFL (243 MEFL), while at the system edges the sensitivity is a few thousand MEFL (~3000 MEFL) (Figure 4.4D).

4.4.3. Performance vs. flow rate

The performance of our parallel system depends on a consistent interaction between the interrogating laser and the particles of interest. For smaller particle sizes and higher flow rates with larger linear velocities, it becomes increasingly difficult for the acoustic field to tightly focus the particles. Additionally, as the linear velocity through the excitation region increases, the transit time decreases, so the absolute number of photons collected, and the sensitivity is reduced. Therefore, we investigated the system performance with varying bead sizes and flow rates.

Three sizes of rainbow calibration beads are analyzed for volumetric flow rates of 250 µl/min up to 10 mL/min. As expected, with a constant camera frame rate (~25 k/s), the peak intensity and the system sensitivity decrease with increasing linear velocity (Figure 4.5). In addition, the acoustic focusing width of the particles across each of the 16 focusing nodes increases at the highest flow rates and linear velocities (Appendix B). With this increase in focusing width, the laser/particle interactions broaden, and we see increased CVs of the fluorescent parameters of each bead population.

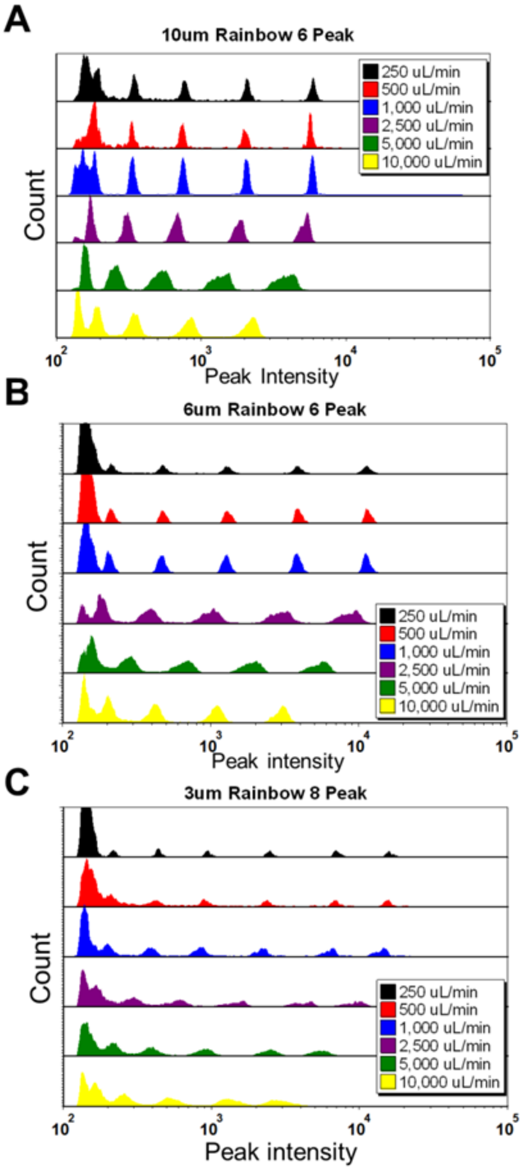

Figure 4.5. Standard calibration beads vs. flow rate (Stream 10). Peak intensity histograms of (A) six peak 10um beads verses flow rate, (B) six peak 6um beads verses flow rate, and (C) 8 peak 3 um beads vs. flow rate.

Despite these two effects (fewer total photons and wider acoustic focusing widths) we still observe strong system performance across a wide range of flow rates and particle sizes. Although the CVs are higher at high flow rates, we see all five fluorescently tagged bead populations for the 10 μm and 6 μm beads at 10 mL/min and achieve moderate performance for the 3 μm 8-peak beads at this flow rate. Additionally, for the constant sample concentration used in these experiments, we observe a linear relationship between event rate and input flow rate (Appendix B). This result suggests that we detect most beads at all flow rates. Given that linear sensitivity increases with laser power (Appendix B), performance sufficient for ~500 MEFL sensitivity may be possible even at 10 mL/min flow rates.

4.4.4. High analysis rates

The ability of the cytometer to run at high analytical event rates is characterized by running 6 μm Nile Red beads at 10 mL/min (Appendix B). At these high flow rates, 957,366 particles are analyzed within 9.4 seconds, yielding a minimal digital processing rate of ~102k/s. The imperfect acoustic focusing of 6 μm particles at these flow rates may lead to some particles being missed, but this study demonstrates that the data system can process at least ~100k events/s in this proof-of-principle implementation.

4.5 Discussion

We demonstrate that line-focused optical excitation of parallel acoustically focused streams provides optical sensitivity and precision comparable to a traditional flow cytometer. While the optical performance is complicated by issues of even light delivery and challenges in high numerical aperture wide-field optical collection, our approach offers the advantage of highly increased volumetric sample delivery rates and the potential to greatly increase analytical collection rates. Our current cytometer design uses three key components: 1) a multi-node acoustic focusing flow cell, 2) a wide line laser excitation profile, and 3) a high-speed imaging detector, all of which are inherently parallelizable. Combining these components into a single platform yields a compact and cost-effective instrument for highly parallel analysis. The high event rates and volumetric throughputs of this platform will allow parallel flow cytometry to be applied to a number of traditional areas, as well as new application spaces where throughput is critical or desirable.

Notably, the optical system described here could also be used with any approach that produces parallel streams of flowing particles. There are many excellent examples of such systems using inertial focusing,[21] surface acoustic waves,[27] dielectrophoresis,[28, 29] and microfluidics.[30,31] Additionally, while other approaches to parallel optics have been developed, which include micro-lens arrays and fiber optic methods, [32, 33] the simplicity of our optical system, both in terms of optical alignment and number of components, makes it a compelling choice to include in an instrument.

It is also useful to consider this work in context of excellent examples of image flow cytometry,[25,26] where the highest speed imaging cytometer, which uses acoustic focusing to maintain a single node in the focal plane,[26] can use offline analysis to analyze low magnification images of samples at analytical rates of ~200k events/s at reduced volumetric rates of ~1 mL/min. While the low magnification images may offer some ability to examine particle morphology, this approach requires image analysis paradigms that are performed offline. Other image cytometers employ higher resolution optics to extract greater morphological details as well as the location of probes within the cell,[23,] and flow cam, although the throughputs of such higher resolution optical systems are generally limited to < 5,000 events/s.

Comparatively, our approach offers real time data processing, higher volumetric throughput, and simpler optical hardware. While our approach can give parameters such as event width and time of flight, these can be correlated to particle morphology using established approaches.[34] Given the factors discussed above, our system is anticipated to be more amenable to future efforts to create sorting systems and for applications requiring higher throughput analysis.

Applications using large sample volumes containing dilute cell concentrations are already addressable using our approach. As our system can analyze samples at 10 mL/min and process data at rates of 100K events/s, simple sample dilution might already allow our system to analyze some rare cell samples. However, applications such as CTCs and fetal cells in maternal blood are more difficult as they require high volumetric and high analytical rate analysis. For example, CTCs can be present at less than 10 cells/mL in a background of ~10^8 cells/mL in whole blood.[35] Therefore, increasing the analytical rate of our platform will make it a more compelling solution for rare cell analysis. Most current approaches use a combination of lysis, centrifugation, and antibody based pull down approaches; however, such steps can result in the loss of rare cells, which has led to many alternative approaches.[35] Our platform would provide a comparative advantage as it would provide a method for direct high throughput analysis for rare cells in blood, in the absence of any separations step, which may provide more accurate and affordable assays.

To increase cellular analysis rate, we will explore increasing the number of streams in our system and the data acquisition rate. Each approach poses specific challenges. Increasing the stream number in the flow cell will require either a higher drive frequency or a wider flow cell. A higher frequency drive will result in tighter spacing between streams, which may affect future work on multicolor systems, but will linearly increase the potential analysis rates as the number of streams increase. A wider flow cell could also analyze more streams but would require optical excitation and collection across a wider field of view. Based upon our experience, the current width of high-NA optical collection is limited to ~4 mm using 25 mm optics and an 8 mm field of view is possible using 50 mm optics.

Beyond the acoustic and optical limits, the detector technology is a key factor. Despite our high volumetric and analytical throughputs, linear velocities through the interrogating laser beam are still about an order of magnitude smaller than typical cytometers (0.04m/s at 1mL/min, 0.42 m/s at 10 mL/min: compared to a typical cytometer at 1-10 m/s). Given the current system geometry, these parameters result in ~5 frames collected for every particle, even at the highest flow rates. To increase analytical rates, we are exploring use of as few as 3 frames per event to provide accurate data. Clearly, faster cameras or array detectors would improve performance.

In addition to increased analytical rates, multicolor detection is needed to enable typical flow cytometry assays. To that end, we can either explore the use of multiple detectors (1 per detection color) or methods that discriminate multiple colors on a single detector. Due to the acoustic focusing, there is a significant amount of free space on the camera’s chip that is currently unused (e.g., dark regions adjacent to each stream in Figure 4.1E). Applying additional optical filters and a small spatial displacement, we can use this chip space to acquire multiple optical parameters simultaneously on a single array detector.

In summary, using multi-node acoustic standing waves to precisely focus particles for analysis, we demonstrate the ability to analyze 16 streams in real time at high event rates (100k/s) and flow rates (10 mL/min). Without complex fluidic or optical designs, this system allows high throughput analysis in a robust, compact and relatively inexpensive platform. This new approach to parallel flow cytometry has the potential to open new applications for flow cytometry including extremely rare cell analysis and inherently dilute large volume samples.

4.6 Conclusion

Using the above approaches, our goal is to construct very high throughput flow cytometry systems based on the new analysis paradigm demonstrated here. Although we have demonstrated an analytical rate of ~100k/s, truly rare blood cell applications would benefit from analytical rates greater than 1M events/s. Within the optical and acoustic bounds described above, we see potential pathways leading to such rates. For example, using a 50 mm optical system, we could drive our standing wave at 5 MHz 128 nodes across an 8 mm field of view to achieve 640k/s. Given this, a simple two-fold increase in detector speed would enable our approach to reach 1.28M events/s, providing a transformational advance in flow cytometry.

Author Information

Corresponding Authors

* Steven Graves, graves@unm.edu

* Andrew Shreve, shreve@unm.edu

Present Addresses

†Daniel Kalb, Los Alamos National Laboratory, Los Alamos, NM 87545. †Gian Maestas, Eta Diagnostics, Inc., 3100 Menaul Blvd. NE, Albuquerque, NM 87107 †Jaime Juarez, Iowa State University, Mechanical Eng., 2020 Black Engr, Ames IA 50011

Author Contributions

The manuscript was written via contributions of all authors. DJK performed experimentation and data collection. FAF constructed flow cells. TAW, GCM, and JJJ assisted in experiments. AS and BSE developed data acquisition systems. APS and SWG planned the project, and guided writing.

Notes

TAW, GCM, APS, and SWG declare financial interest in this technology as it is licensed by Eta Diagnostics, Inc., a company they have a financial stake in. GCM, BSE, APS, and SWG declare they are working with Eta Diagnostics, Inc., to commercialize the technology. AS has financial interest in DarklingX, LLC, which develops data systems.

4.7 Acknowledgments

We thank Alireza Goudarzi for his assistance. This research was supported by the National Institute of General Medical Sciences of the National Institutes of Health under award number R21GM107805 and the NSF under award OCE 1131134. JJJ was supported by the Academic Science Education & Research Training (ASERT) program, NIH K12GM088021. Some data were generated in the UNM Shared Flow

Cytometry & High Throughput Screening Resource Center supported by the UNM Health Sciences Center and the UNM Cancer Center with funding from NCI 2P30 CA118100-11 "UNM Cancer Center Support Grant".

4.8 References

(1) A. L. Givan, *Flow cytometry: first principles*, John Wiley & Sons, 2013.

(2) M. E. Piyasena and S. W. Graves. The Intersection of Flow Cytometry with Microfluidics and Microfabrication. *Lab on a Chip*. 2014, 14 (6) 1044 1059.

(3) P. Bacher and A. Scheffold. Flow-Cytometric Analysis of Rare Antigen-Specific T cells. *Cytometry Part A*. 2013, 83 (8), 692-701.

(4) C. Alix-Panabières and K. Pantel. Circulating Tumor Cells: Liquid Biopsy of Cancer. *Clinical chemistry*. 2013, 59 (1), 110-118.

(5) D. L. Jaye, R. A. Bray, H. M. Gebel, W. A. C. Harris and E. K. Waller. Translational Applications of Flow Cytometry in Clinical Practice. *The Journal of Immunology*. 2012, 188 (10), 4715-4719.

(6) B. D. Hedley and M. Keeney. Technical Issues: Flow Cytometry and Rare Event Analysis. *International Journal of Laboratory Hematology*. 2013, 35, 344-350.

(7) M. J. Saunders, S. W. Graves, L. A. Sklar, T. I. Oprea and B. S. Edwards. High-Throughput Multiplex Flow Cytometry Screening for Botulinum Neurotoxin Type A Light Chain Protease Inhibitors. *Assay and Drug Development Technologies*. 2010, 8 (1), 37-46.

(8) F. W. Kuckuck, B. S. Edwards and L. A. Sklar, High Throughput Flow Cytometry. *Cytometry*. 2001, 44 (1), 83-90.

(9) B. S. Edwards and L. A. Sklar. Flow Cytometry: Impact On Early Drug Discovery. *Journal of Biomolecular Screening*. 2015, 20 (6), 689-707.

(10) R. J. Olson and H. M. Sosik. A Submersible Imaging-In-Flow Instrument to Analyze Nano-and Microplankton: Imaging FlowCytobot. *Limnology and Oceanography Methods*. 2007, 5, 195-203.

(11) G. B. J. Dubelaar, P. L. Gerritzen, A. E. R. Beeker, R. R. Jonker and K. Tangen. Design and First Results of CytoBuoy: a Wireless Flow Cytometer for in situ Analysis of Marine and Fresh Waters. *Cytometry*. 1999, 37 (4), 247-254.

(12) C. K. Sieracki., M. E. Sieracki., and C. S. Yentsch. An Imaging-In-Flow System For Automated Analysis Of Marine Microplankton. *Marine Ecology Progress Series*. 1998, 168: 285-296.

(13) P. K. Mandal, A. K. Biswas, K. Choi and U. K. Pal. Methods for Rapid Detection of Foodborne Pathogens: An Overview *American Journal Of Food Technology*. 2011, 6 (2), 87-102.

(14) H. M. Shapiro, *Practical flow cytometry*, John Wiley & Sons, 2005.

(15) G. Goddard, J. C. Martin, S. W. Graves and G. Kaduchak. Ultrasonic Particle-Concentration for Sheathless Focusing of Particles for Analysis in a Flow Cytometer. *Cytometry Part A*. 2006, 69 (2), 66-74.

(16) G. R. Goddard, C. K. Sanders, J. C. Martin, G. Kaduchak and S. W. Graves. Analytical Performance of an Ultrasonic Particle Focusing Flow Cytometer. *Analytical Chemistry*. 2007, 79 (22), 8740-8746.

(17) M. Ward, P. Turner, M. DeJohn and G. Kaduchak. Fundamentals of Acoustic Cytometry. *Current Protocols in Cytometry*. 2009, 49, 1-22.

(18) J. Picot, C. L. Guerin, C. L. V. Kim and C. M. Boulanger. Flow Cytometry: Retrospective, Fundamentals and Recent Instrumentation. *Cytotechnology*. 2012, 64 (2), 109-130.

(19) D. Wlodkowic and Z. Darzynkiewicz, in *Recent Advances in Cytometry, Part a: Instrumentation, Methods, Fifth Edition*, eds. Z. Darzynkiewicz, E. Holden, A. Orfao, W. Telford and D. Wlodkowic, Elsevier Academic Press Inc, San Diego, 2011, vol. 102, 105-125.

(20) B. S. Edwards, J. S. Zhu, J. Chen, M. B. Carter, D. M. Thal, J. J. G. Tesmer, S. W. Graves and L. A. Sklar. Cluster Cytometry for High-Capacity Bioanalysis *Cytometry Part A*. 2012, 81A (5), 419-429.

(21) S. C. Hur, H. T. K. Tse and D. Di Carlo. Sheathless Inertial Cell Ordering for Extreme Throughput Flow Cytometry. *Lab on a Chip*. 2010, 10 (3), 274-280.

(22) A. Lenshof and T. Laurell. Continuous Separation of Cells and Particles in Microfluidic Systems. *Chemical Society Reviews*. 2010, 39 (3), 1203-1217.

(23) M. E. Piyasena, P. P. A. Suthanthiraraj, R. W. Applegate, A. M. Goumas, T. A. Woods, G. P. Lopez and S. W. Graves. Multinode Acoustic Focusing for Parallel Flow Cytometry. *Analytical Chemistry*. 2012, 84 (4), 1831-1839.

(24) P. P. A. Suthanthiraraj, M. E. Piyasena, T. A. Woods, M. A. Naivar, G. P. Lopez and S. W. Graves. One-Dimensional Acoustic Standing Waves in Rectangular Channels for Flow Cytometry. *Methods*. 2012, 57 (3), 259-271.

(25) D. A. Basiji, *Imaging Flow Cytometry: Methods and Protocols*. 2016, 13-21.

(26) R. Zmijan, U. S. Jonnalagadda, D. Carugo, Y. Kochi, E. Lemm, G. Packham, M. Hill and P. Glynne-Jones. High Throughput Imaging Cytometer with Acoustic

Focussing. *RSC Advances*. 2015, 5 (101), 83206-83216.

(27) J. Shi, X. Mao, D. Ahmed, A. Colletti and T. J. Huang. Focusing Microparticles in a Microfluidic Channel with Standing Surface Acoustic Waves (SSAW). *Lab on a Chip*. 2008, 8 (2), 221-223.

(28) L. Wang, L. A. Flanagan, N. L. Jeon, E. Monuki and A. P. Lee. Dielectrophoresis Switching with Vertical Sidewall Electrodes for Microfluidic Flow Cytometry. *Lab on a Chip*. 2007, 7 (9), 1114-1120.

(29) D. Holmes, J. K. She, P. L. Roach and H. Morgan. Bead-Based Immunoassays using a Micro-Chip Flow Cytometer. *Lab on a Chip*. 2007, 7 (8), 1048-1056.

(30) B. K. McKenna, J. G. Evans, M. C. Cheung and D. J. Ehrlich. A Parallel Microfluidic Flow Cytometer for High-Content Screening. *Nature Methods*. 2011, 8 (5), 401-403.

(31) D. A. Ateya, J. S. Erickson, P. B. Howell, L. R. Hilliard, J. P. Golden and F. S. Ligler. The Good, the Bad, and the Tiny: a Review of Microflow Cytometry. *Analytical and Bioanalytical Chemistry*. 2008, 391 (5), 1485-1498.

(32) J.-N. Kuo, C.-C. Hsieh, S.-Y. Yang and G.-B. Lee. An SU-8 Microlens Array Fabricated by Soft Replica Molding for Cell Counting Applications. *Journal of Micromechanics and Microengineering*. 2007, 17, 693.

(33) J. R. Gilbert, E. Sinofsky and M. Deshpande. Optical detector for a particle sorting system. Patent, *Journal*. 2008.

(34) V. P. Maltsev. Scanning Flow Cytometry for Individual Particle Analysis. *Review of Scientific Instruments*. 2000, 71 (1), 243-255.

(35) S. Nagrath, L. V. Sequist, S. Maheswaran, D. W. Bell, D. Irimia, L. Ulkus, M. R. Smith, E. L. Kwak, S. Digumarthy and A. Muzikansky. Isolation of Rare Circulating Tumour Cells in Cancer Patients by Microchip Technology. *Nature*. 2007, 450 (7173), 1235-1239.

Chapter 5: Acoustic Focusing in the Presence of Sample Separating Bubbles for High Throughput Flow Cytometry

Frank A. Fencl,[1] Aurora Fabry-Wood,[1] Alireza Goudarzi,[1] Daniel M. Kalb,[1] Travis A. Woods,[1,2] Bruce S. Edwards,[2] Andrew P. Shreve,[1] and *Steven W. Graves[1]

[1]Department of Chemical and Biological Engineering, Center for Biomedical Engineering, University of New Mexico, Albuquerque, NM 87131

[2]Center for Molecular Discovery, Innovation Discovery and Training Center, Health Sciences Center, University of New Mexico, Albuquerque, New Mexico, 87131-0001 United States

5.1 Abstract

Acoustic flow cytometry is growing as an effective clinical and research tool for cellular analysis and diagnostics. With the growth of automated systems in clinical labs, state of the art instruments such as flow cytometers have been integrated as viable platform technologies. Many of these automated platforms require multi-well plate sampling to handle large amounts of patient sample throughput. To model an automated system with acoustic flow cytometry as the testing platform, we couple our custom high throughput parallel acoustic flow cytometer and auto sampler to investigate particle behavior during multi-well sampling where air is introduced into the system between sample volumes. Introducing air between samples is used as a regular method to track each individual sample as well as to "scrub" the interstitial space between sample boluses. This intermittent introduction of air is hypothesized to affect particle focusing at the air-water interface in an acoustic focusing flow chamber. Characterizing the behavior at the sample bolus level allows us to observe potential focusing disruption while giving us a better understanding of how acoustic particle focusing behaves for an automated platform. Here we will study sample focusing at the air-water interface in an acoustic focusing flow chamber on select particle sizes and volumetric flow rates to assess whether acoustic flow cytometers can effectively be integrated into such automated platforms.

5.2 Introduction

Flow cytometry is widely used for cellular analysis and as a diagnostic tool.[1–4] Conventional hydrodynamic focusing flow cytometers have been shown to integrate an auto-sampler with air bubble sample separation techniques to achieve automated high throughput analysis.[5] Most flow cytometers use hydrodynamic focusing to compress a sample volume in the flow chamber to the interrogation width of the probing laser's optical diameter.[3,4,6] With this conventional method, sampling up to tens of thousands of cells per second has been achieved.[4] Research in advancing sample throughput for flow cytometry considers ways of improving hydrodynamic focusing or replacing it as a method to focus sample contents altogether.[6–9] Acoustic flow cytometry is an alternate way of focusing sample particles without the requirement of a hydrodynamic focusing sheath fluid. This method of flow cytometry is expanding as an effective method of high throughput sheathless sample stream focusing.[10,11] Removing the need for a hydrodynamic sheath fluid results in lowered reagent costs and in eliminating shear stress on biological media. With this method, the number of particles sampled per second can be increased by an order of magnitude.[12]

Acoustic flow cytometry has become a useful tool for cell sorting, media separations. and high-volume sampling in flow cytometry assays.[7,13] These instruments are widely used for their unparalleled ability to quickly analyze large volumes of sample and characterize multiple parameters of the sample.[12] With the increasing development of flow cytometers for high throughput screening, more assays are being developed around these technologies.[14,15] Some limitations and fundamental information are still being investigated as assays developed for these acoustic focusing systems are increasing in complexity and quantity. Among these assays, multi-well sampling with automated systems is being explored for integration with these instruments.

Acoustic focusing technology for these platforms, or acoustophoresis, is the practice of moving particles using ultrasonic standing waves. This method of sample media manipulation works based on intrinsic physical properties of the particles. The basic principle is based on the primary acoustic radiation force equation given below.[16,17]

$$F = -\frac{(\pi P^2 V_p \beta_m)}{2\lambda} \phi(\beta, \rho) \sin 2kx \tag{1}$$

where,

$$\phi(\beta, \rho) = \frac{5\rho_p - 2\rho_m}{2\rho_p + \rho_m} - \frac{\beta_p}{\beta_m} \tag{2}$$

Particles with a higher density (ρ_p) and lower compressibility (β_p) than the surrounding fluid medium (ρ_m, β_m) will focus at the nodes generated by an acoustic transducer and less dense more compressible particles will focus at the antinode of the fluid filled channel. Particles exhibiting a positive $\Phi(\beta,\rho)$, or acoustic contrast factor, will focus at the pressure node while particles with a negative acoustic contrast will focus at anti-nodes. Most biological particles, i.e. cells, exhibit a positive acoustic contrast and will therefore focus at the pressure node.

The introduction of air bubbles has been known to cause problems in conventional flow cytometers using hydrodynamic focusing.[4,5,18,19] To mimic a high throughput multi-well sampling scenario, air bubbles are introduced and anecdotally used to discern individual sample volumes as well to ‘scrub’ in between each sample to reduce cross-over contamination as was done previously by Ramirez et al. and Kukuck et al.[5,19] In these studies, accounting for air bubbles between sample boluses allows software to read the beginning and end of a sample volume by detecting the terminal regions of the air-water interfaces.

Using a silicon core optically transparent flow chamber coupled with a piezoelectric transducer as our acoustic focusing flow chamber, we observe the behavior of particles focused by a single node acoustic standing wave while being disrupted by the regular introduction of intermittent air bubbles. To model this behavior across a specific set of parameters, we use a custom sensitive imaging flow cytometer.[12] As a model fluorescent microparticle, we selected Nile Red beads at varying sizes (3, 6, and 10 µm) to observe if focusing disruption is less evident given that the magnitude of the primary acoustic radiation force is felt more by larger particles. Polystyrene beads are largely used for calibration and microsphere-based assays, they likewise exhibit a positive acoustic contrast factor and respond to the acoustic standing wave akin to mammalian cells.[20,21,22]

The goal of this research is to explain fundamental behavior occurring in an acoustically focused system with automated sampling at constant flow. After investigating acoustic focusing at the air-water interface for multi-well sampling at various particle sizes and flow rates, we anecdotally analyze the loss of events between sample volumes. The information gained from our experiments also give us a better understanding of optimal parameters regarding flow rates for acoustically focusing small particles.

5.3 Materials and methods

5.3.1 Device fabrication

The microfluidic device used for our experiments is designed and fabricated at the University of New Mexico. We use Auto CAD (version 2013, Autodesk, Inc) to design the pattern of the channel within the silica wafer's dimensions. The channel is a 644 μm wide and 5cm long rectangular channel. The depth of the channel is 500μm, the thickness of the silica wafer.

The device pattern and silicon wafer undergo photolithography at the UNM Manufacturing Training and Technology Center (MTTC) photolithography bay. The device is also cleaned and processed for Etching at UNM MTTC. The patterned silicon wafer is completely etched through using a custom Bosch DRIE etch profile.[23] This design allows minimal photon trapping from the laser source as well as back scatter and reflection which could adversely affect imaging and analysis.

The etched device is prepared for double-side anodic bonding with a piranha cleaning step using standard 70:30 sulfuric acid (H_2SO_4) to hydrogen peroxide (H_2O_2) procedure. Anodic bonding is achieved with a hotplate, aluminum ground plate, and direct current (DC) probe whose current passes through the sandwiched device into the ground plate.[24,25] To interface the inlet and outlet tubing, PDMS is used because it can be bonded to glass permanently using a plasma oxide cleaner. A lead zirconate titonate (PZT) piezoelectric transducer, providing the acoustic force to vibrate the flow chamber, is then firmly attached directly over the channel, upstream of the anticipated interrogation region. Full details on flow chamber device fabrication can be found in chapter 3 of this dissertation.

5.3.2 Particle solutions

Four Nile Red (NR) polystyrene particle solutions are prepared for our experiments. The particle sizes used are 0.93μm, 3μm, 6μm, and 10μm NR polystyrene microspheres. The varying particle size concentrations are all the same order of magnitude in concentration of 10^4 particles/mL. The difference in particle concentration does not change the observed effect of acoustic focusing disruption and nodal position recovery. The particles are mixed in Nano pure water from stock solutions provided by Spherotech Inc.

The particle concentrations are verified using an Accuri flow cytometer and through particle per second counts in custom real-time detection software as done previously.[12] Each particle count was taken 3 times and averaged. The concentration of 10μm particles are 14,000 particles/mL, the 6μm particles are ~54,000 particles/mL, the 3μm particles are ~108,000 particles/mL, and the 0.93μm particles are ~74,000 particles/mL. Before each experimental run, the solutions are vortexed for homogeneity.

5.3.3 Optics and collection

The custom optics and collection using a high-speed Hamamatsu camera is used for the image array data collection. A depiction of the custom optical setup can be seen in supporting information for this chapter (Appendix C) as well as in our previous work.[12]

5.3.4 Experimental

Two sets of experiments are employed; manual and automated where the sample is taken up for a brief period to ensure a fixed volume for each system input of fluid and air. An illustration of the effect of stream disruption when an air bubble is introduced can be seen in Figure 5.1 C, D. These sets of experiments mimic the multi-well sampling in a previously mentioned custom high throughput flow cytometer.[26] The selected factors to investigate acoustic focusing efficiency are to compare particle size and flow rate while holding applied voltage, frequency of the transducer and flow chamber constant in the presence of intermittent air bubbles. It has been previously discussed how optimal transducer frequency and voltage input parameters are tuned for acoustic focusing systems.[12,27,28]

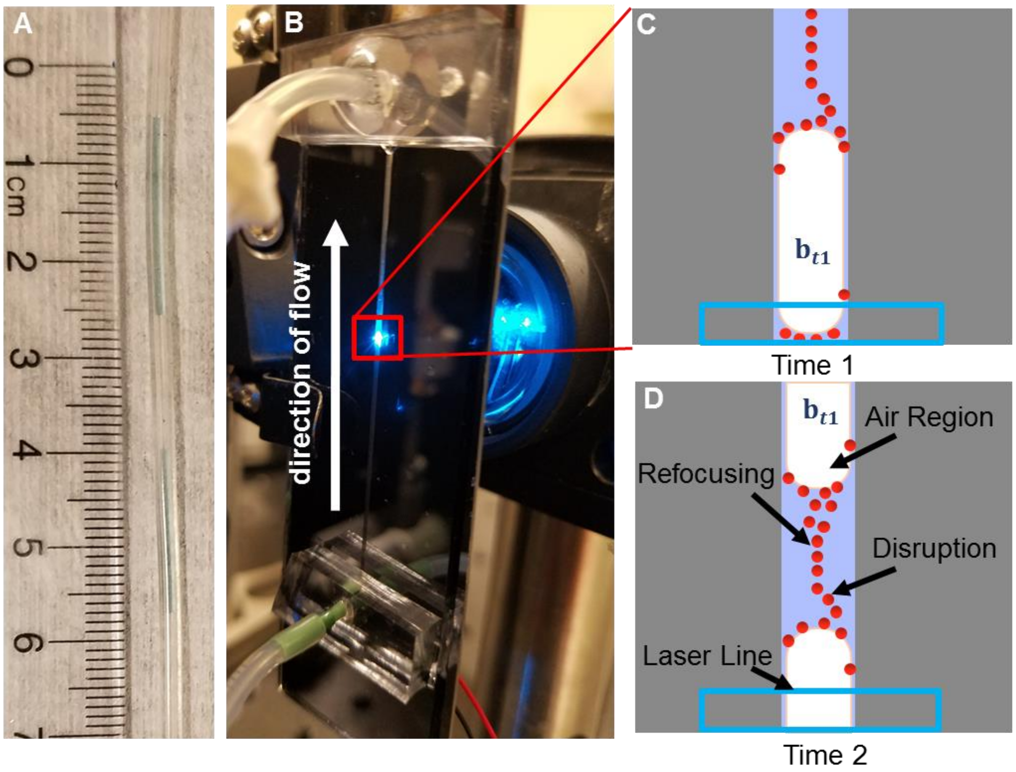

Figure 5.1. Device and focusing disruption due to air. (A) Blue colored solution fluid flowing in the inlet Tygon tubing interspersed between air bubbles. (B) Silicon core optically transparent flow chamber shown in the optical interrogation region of the 488 nm laser. (C) Illustration of focused particle stream behavior as a bubble (bt1) enters the region of interest. (D) Illustration of particle behavior between the trailing edge of a bubble and the leading edge of another.

Flow rate and particle size are varied to assess direct effects on sample stream recovery after air bubbles are introduced into the flow system. For the transducer attached to the fabricated custom silicon-core flow chamber, the optimal single stream focusing parameters, i.e. input voltage and frequency, are set by measuring the particle stream width for each size across multiple flow rates. In this case, the applied voltage of ~16 V peak to peak, and the specific frequency are tuned for each particle size, where the mean frequency for focusing is 1.2 MHz. The input voltage is held constant to reduce heat that can cause evaporation and cavitation from excessive power input.

We collect imaging array data using the high-speed camera optical system mentioned above (zoomed in single frames of the flow chamber region of interest, ROI, can be seen in Figure 5.2) and Kytos software as was done in previous work.[12] The custom camera software we used for this project was acquired from the company Darkling X, Los Alamos, NM. The software obtained, Kytos, is image analysis software that can give important information as in conventional flow cytometry. This software is how we measured where the optimal frequency gave the best particle stream focusing. Each event was captured on an 8 x 2048-pixel image taken at 25,000 frames per second. The software exports fcs files for further analysis in FCS Express software. Figures 5.3, 5.4 illustrate the efficiency of acoustic particle focusing, by size, when the sample volumes are interspersed with air bubbles. The recovery response of our medium particle size (6 µm) by flow rate can be seen later in this chapter.

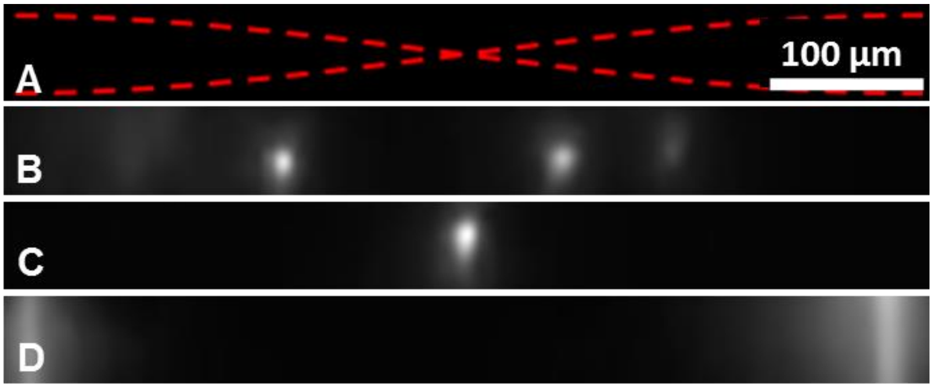

Figure 5.2. Image cross-section of particles in flow chamber. (A) ~41 x 360-pixel cross section zoomed over the flow chamber channel with an overlay of theoretical single node acoustic standing wave (dotted red line). (B) Unfocused 10 µm particles flowing through the ROI. (C) Single node acoustically focused 10 µm particle. (D) Air bubble passing through the ROI.

The focused particle positions are plotted in a histogram and then fit to a Gaussian curve given by equation:

$$f(x) = ae^{-\frac{(x-b)^2}{2c^2}} \tag{3}$$

where *a* is the height of the curve, *b* is the center of the peak, and *c* is the standard deviation or width of the curve. The full width half max (FWHM) of the Gaussian fits was calculated for focused stream width values as done conventionally in the field of flow cytometry.[4,29–31] Following the collection and fitting of the control data for each particle size and flow rate we collected the same data for the bubble disrupted experiments. The Gaussian fit analysis focuses on the regions between bubbles to measure the quality of the recovery to a focused state. The gated regions were plotted as a histogram and fit to a Gaussian to obtain the FWHM values. Following the collection of the FWHM values, we plotted each of them versus the control data.

5.4 Results and discussion

5.4.1 Particle focus at the air-water interface

To observe the behavior of particles in the discussed system, we used our custom high throughput acoustic flow cytometer developed at UNM.[12] The system we have set up has a 0.6 mm wide channel optically transparent silicon core flow chamber coupled with a 488 nm laser excitation source and specialized optics scheme to form a wide thin beam for interrogation across the wide channel flow chamber.

We observed the leading edge of an air bubble disrupts the acoustic focusing of particles (Figures 5.1, 5.2). The particles recover almost instantly (within a second) with small variation in between the different tested flow rates, which seems to be the main factor contributing to particle focusing recovery. Depicted in Figure 5.1, we can see that the particle stream recovers to a focused state and remains so until another air bubble moves through the system.

5.4.2 Focusing recovery by particle diameter

Figure 5.3 illustrates the recovery of each sample by particle diameter. The data set in Figure 5.3 are at the effective medium flow rate of 250 µL/min. It is important to note that 3 µm particles do not focus as well as 6 or 10 µm particles due to the magnitude of the primary acoustic radiation force. The magnitude of this force scales directly with the particle size, V_p from Equation 1. 6 and 10 µm particles remain tightly focused after the bubbles transit through the flow chamber, although we can see an observable shift in the node position of the 10 µm particles after the first bubble flows through. Despite this node position shift, the 10 µm particle stream recovers to a tight focus after the bubbles pass. Figure 5.4 illustrates the same data as Figure 5.3 but as a mean tracking of the event position across the flow channel to clearly depict the immediate and tight recovery of each particle size. The standard deviation of the mean position is shown in red. A histogram of particle positions across the flow chamber channel for controls (no bubbles introduced) and recovered regions (data immediately after the first bubble passes and up to the second) for all particle sizes and flow rates can be seen in supporting information for this chapter (Appendix C).

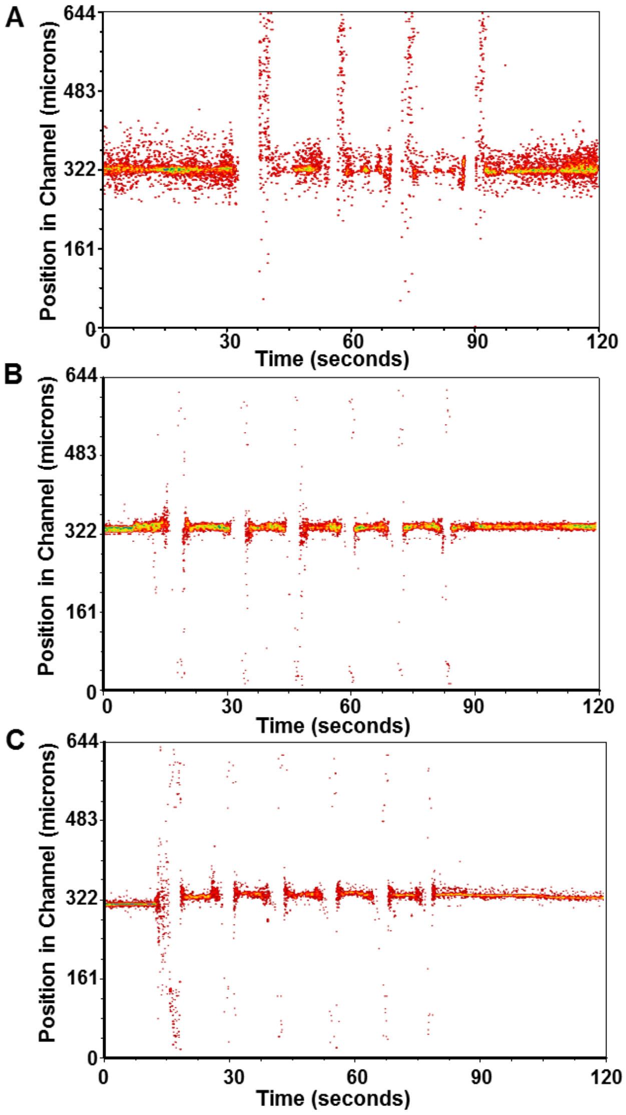

Figure 5.3. Acoustically focused particle streams by particle size with introduced bubbles. Event position tracking data of the three primary analyzed particles sizes at the medium optimal flow rate of 250µL/min over 2 minutes using an autosampler arm. Each data set is displayed at a resolution of 1024 x 1024. (A) 3 µm particles with 5 air bubbles. (B) 6 µm particles with 6 air bubbles. (C) 10 µm particles with 6 air bubbles.

From Figures 5.3-5.5, we see some particles (order of ten) are lost in the air bubble region. A program differentiating each sample bolus would not calculate these events and the data would be counted as a loss. The percent calculated event loss over five bubbles across the three particle sizes at the medium flow rate of 250 µL/min is 1.3, 1.0, and 3.8% for 3, 6, and 10 µm particles respectively. These values were calculated from manually gated regions as seen in supporting information for this chapter (Appendix C). The events were taken from the manually gated regions and divided over the total number of events in the two-minute data sets. The average number of particles lost per bubble rounded to the nearest whole number over 5 bubbles are 17, 19, and 50 particles per bubble for 3, 6, and 10 µm particles respectively.

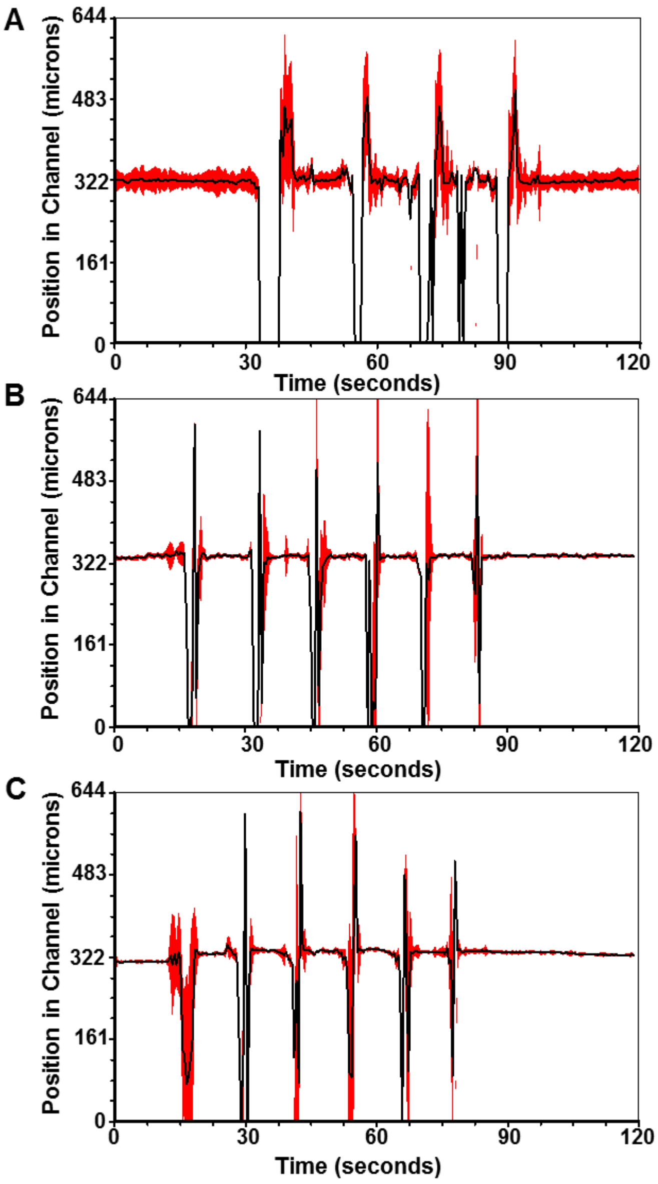

Figure 5.4. Mean particle position with standard deviation. Mean (black) and standard deviation (red) event position tracking data of each of the three primary analyzed particles sizes at the medium flow rate of 250µL/min using an autosampler arm. Resolution is set to 256 x 256 for better display. (A) 3 µm particles with 5 air bubbles. (B) 6 µm particles with 6 air bubbles. (C) 10 µm particles with 6 air bubbles.

To better understand how many events are lost in the air region, we compared the ratio of particles in the focused ‘data collection’ region to particles lost in the air bubble over a 2-minute collection period. The ratios are 46.0, 62.0, 17.5 for 3, 6, and 10 µm particles respectively. These event counts are obtained from manually gated regions of air bubbles and the refocused regions after the particle stream mean returns to a visually focused state.

5.4.3 Focusing recovery by flow rate

The data set for 6 µm particles at low, medium, and high flow rates can be seen in Figure 5.5. For better visibility of stream recovery after bubble transit, we took an extended data collection for the lowest flow rate (25 µL/min) and a zoomed in one for the highest (2,500 µL/min) so that the stream can be viewed to have been disrupted then almost immediately recover. The full, unzoomed, image can be seen in supporting information for this chapter (Appendix C), along with a zoomed figure of the mean position tracing illustrating the rapid recovery after a bubble passes through the device. Low quality of particle focusing can be seen at the lowest flow rate (25 µL/min).

Focusing disruption by intermittent air introduction could adversely affect sample analysis where the particles at the air-water interfaces in an acoustic focusing system may not be counted properly resulting in loss of data. Imaging flow cytometry could potentially be an improvement over standard particle detection schemes found in most flow cytometers. The particles however, do seem to remain within their sampled volume region and crossover does not seem to be an observed issue.

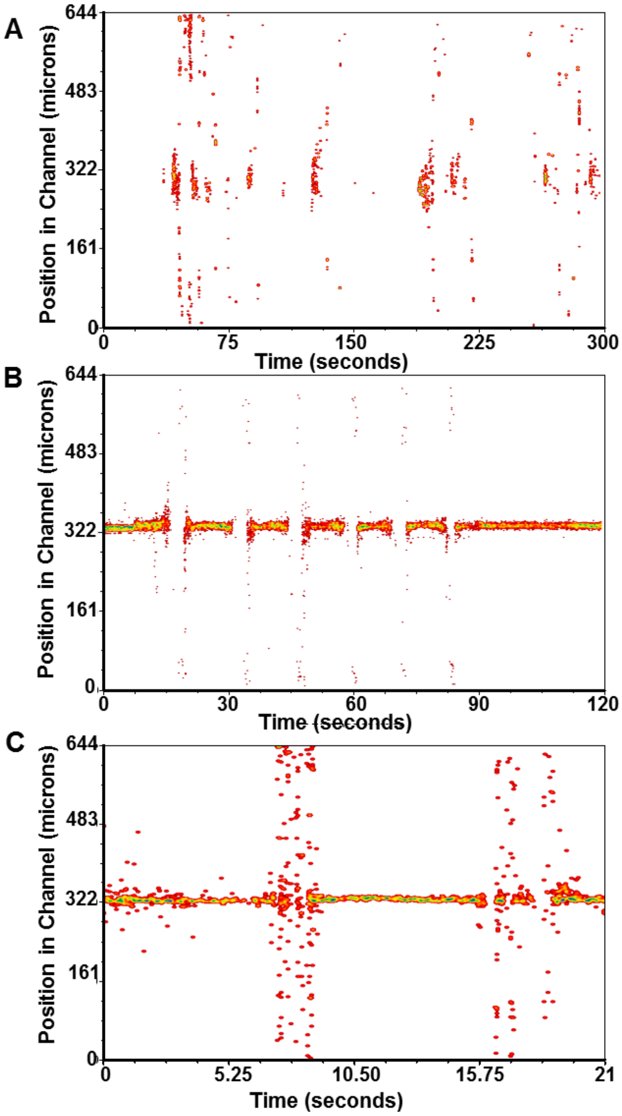

Figure 5.5. 6 µm particle stream recovery across 3 flow rates. Event position tracking data of 6 µm particles at three flow rates, low medium and high, respectively. (A) 25 µL/min with bubbles introduced by hand over 300 seconds to show state change from “disrupted” to “focused”. (B) 250 µL/min with bubbles introduced via autosampler over 120 seconds. (C) 2,500 µL/min with bubbles introduced manually over 21 seconds to show zoomed in state change from “disrupted” to “focused”.

5.4.4 Comprehensive full width at half max analysis

Figure 5.6 illustrates the varying recovery values by particle size across the tested flow rates (table in Appendix C). Our initial experiments included 0.93 µm particles across the selected flow rates, however the primary acoustic radiation force scales with particle size, as seen in Equation 1 by V_p, and particles less than 3µm in diameter do not focus well because the primary acoustic force effectively diminishes and a phenomenon termed acoustic streaming, or Rayleigh streaming, begins to occur.[13,32–35] The other particle sizes, 3µm-10µm, exhibited expected focusing even after being disrupted with intermittent sampling air bubbles.

From the full width at half max (FWHM) value data set we can also see that the quality of sample stream focusing with respect to flow rates has a concave shaped curve (Figure 5.6). This indicates that at the highest and lowest flow rates tested, the quality of particle stream focus is lower than at the median flow rates (25 µL/min to 1000 µL/min). This tells us two things; one, that the particle transit time through the acoustic field over the region where the transducer is attached, affects the focusing quality, and two, that some amount of hydrodynamic force is required to lift the particles off the side walls of the flow chamber to overcome acoustic trapping that occurs when too many particles are in close proximity to each other at lower flow rates.[17-21] The high flow rates also do not exhibit a lower quality of focus due to turbulent flow because the Reynolds numbers here are significantly lower than the lower bound of Re (Re > 1000).[36,37] Theoretically, turbulent flow for our flow chamber occurs at approximately 60 mL/min, while our experimental upper limit is 2.5mL/min.

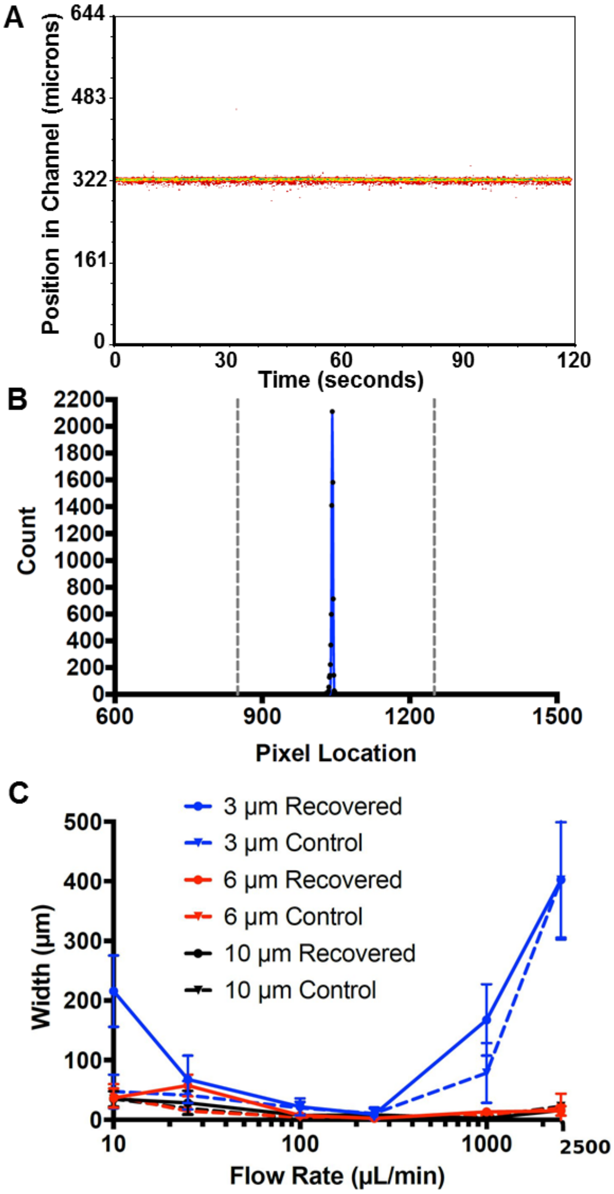

Figure 5.6. FWHM comprehensive data. (A) Control, no bubbles introduced, event position tracking data of 6 µm particles at 250 µL/min. (B) Gaussian fit to histogram data of 6 µm particle control positions at 250 µL/min over 120 seconds, channel bounds displayed as grey dotted lines. (C) Comprehensive full width at half max (FWHM) data from gaussian fits of 3, 6, and 10 µm particles over all flow rates 10, 25, 100, 250, 1000, 2500 µL/min disrupted by air bubbles, and for control sets (no bubbles). Each FWHM for bubble/experimental sets are sections of particle stream recovery of focus immediately after the first air bubble and up to the next bubble. The error bars are calculated single standard deviation values from the gaussian fits for each data point.

5.5 Conclusion

In addition to the benefits acoustic flow cytometry provides i.e., faster sample throughput, sample recovery post processing without the need for dilution, and reduction of consumables (hydrodynamic sheath fluid), this work describes that acoustic flow technology is robust in the presence of intermittent air bubbles. Our work confirms that acoustic focusing flow technology is compatible and robust for high throughput systems where constant flow multi-well sampling is employed. Particle streams perturbed by intermittent air bubbles have their focusing disrupted but immediately recover within one second after the air gap passes. Our results have also given us deeper insight to limits of acoustic particle focusing. Particles with low transit times through the acoustic field, or higher flow rates >1000 µL/min, exhibit an observed weaker quality of focusing. We assert that the lower quality of focus is not due to turbulence as the Reynolds numbers achieved at the highest flow rates do not approach the turbulent regime until ~60 mL/min for our device. Conversely, particles flowing at low flow rates exhibit long transit times in the field but do not focus well because not enough hydrodynamic lift allows the particles to separate from the side walls to overcome acoustic trapping and move into the node region of the acoustic standing wave. Future work will incorporate a quantitative approach to sample stream focus recovery as well as studies of focusing quality across multiple parallel particle streams within a single flow chamber.

5.6 References

(1) Brown, M. and C. Wittwer. Flow Cytometry: Principles and Clinical Applications in Hematology. *Clinical Chemistry*. 2000, 46 (8): 1221.

(2) Barlogie, B.; Raber, M. N.; Schumann, J.; Johnson, T. S.; Drewinko, B.; Swartzendruber, D. E.; Göhde, W.; Andreeff, M.; Freireich, E. J. Flow Cytometry in Clinical Cancer Research. *Cancer Research.* 1983, *43* (9), 3982–3997.

(3) Piyasena, M. E.; Graves, S. W. The Intersection of Flow Cytometry with Microfluidics and Microfabrication. *Lab on a Chip.* 2014, *14* (6), 1044–1059.

(4) Shapiro, H. *Practical Flow Cytometry Fourth Edition*; John Wiley & sons, inc. 2004. 166-178

(5) Kuckuck, F. W.; Edwards, B. S.; Sklar, L. a. High Throughput Flow Cytometry. *Cytometry.* 2001, *44* (1), 83–90.

(6) Yang, R. J.; Fu, L. M.; Hou, H. H. Review and Perspectives on Microfluidic Flow Cytometers. *Sensors and Actuators, B: Chemical*. 2018, 26–45.

(7) Goddard, G. R.; Sanders, C. K.; Martin, J. C.; Kaduchak, G.; Graves, S. W. Analytical Performance of an Ultrasonic Particle Focusing Flow Cytometer. *Analytical Chemistry.* 2007, *79* (22), 8740–8746.

(8) Oakey, J.; Applegate, R. W.; Arellano, E.; Carlo, D. Di; Graves, S. W.; Toner, M. Particle Focusing in Staged Inertial Microfluidic Devices for Flow Cytometry. *Analytical Chemistry.* 2010, *82* (9), 3862–3867.

(9) Cheung, K. C.; Berardino, M. Di; Schade-Kampmann, G.; Hebeisen, M.; Pierzchalski, A.; Bocsi, J.; Mittag, A.; Tárnok, A. Microfluidic Impedance-Based Flow Cytometry. *Cytometry Part A*. 2010. 77A (7), 648-666.

(10) Goddard, G.; Martin, J. C.; Graves, S. W.; Kaduchak, G. Ultrasonic Particle-Concentration for Sheathless Focusing of Particles for Analysis in a Flow Cytometer. *Cytometry Part A.* 2006, *69* (2), 66–74.

(11) Adan, A.; Alizada, G.; Kiraz, Y.; Baran, Y.; Nalbant, A. Flow Cytometry: Basic Principles and Applications. *Critical Reviews in Biotechnology*. 2017. 37 (2), 163-176

(12) Kalb, D. M.; Fencl, F. A.; Woods, T. A.; Swanson, A.; Maestas, G. C.; Juárez, J. J.; Edwards, B. S.; Shreve, A. P.; Graves, S. W. Line-Focused Optical Excitation of Parallel Acoustic Focused Sample Streams for High Volumetric and Analytical Rate Flow Cytometry. *Analytical Chemistry.* 2017, 89 (18), 9967–9975.

(13) Lenshof, A.; Magnusson, C.; Laurell, T. Acoustofluidics 8: Applications of Acoustophoresis in Continuous Flow Microsystems. *Lab on a Chip.* 2012, *12*

(7), 1210.

(14) Krutzik, P. O.; Nolan, G. P. Fluorescent Cell Barcoding in Flow Cytometry Allows High-Throughput Drug Screening and Signaling Profiling. *Nature Methods.* 2006, 3 (5), 361–368.

(15) Edwards, B. S.; Sklar, L. A. Flow Cytometry: Impact on Early Drug Discovery. *Journal of Biomolecular Screening.* 2015, 20 (6), 689–707.

(16) Lenshof, A.; Evander, M.; Laurell, T.; Nilsson, J. Acoustofluidics 5: Building Microfluidic Acoustic Resonators. *Lab on a Chip.* 2012, 12 (4), 684.

(17) Bruus, H. Acoustofluidics 7: The Acoustic Radiation Force on Small Particles. *Lab on a Chip.* 2012, *12* (6), 1014.

(18) Graves, S. W.; Nolan, J. P.; Jett, J. H.; Martin, J. C.; Sklar, L. A. Nozzle Design Parameters and Their Effects on Rapid Sample Delivery in Flow Cytometry. *Cytometry.* 2002, *47* (2), 127–137.

(19) Ramirez, S.; Aiken, C. T.; Andrzejewski, B.; Sklar, L. a; Edwards, B. S. High-Throughput Flow Cytometry: Validation in Microvolume Bioassays. *Cytometry Part A.* 2003, 53A, 55-65

(20) Ai, Y.; Sanders, C. K.; Marrone, B. L. Separation of Escherichia Coli Bacteria from Peripheral Blood Mononuclear Cells Using Standing Surface Acoustic Waves. *Analytical Chemistry.* 2013, *85* (19), 9126–9134.

(21) Hasegawa, T.; Yosioka, K. Acoustic-Radiation Force on a Solid Elastic Sphere. *Journal of Acoustical Society of America.* 1969, *46* (5B), 1139–1143.

(22) Li, P.; Mao, Z.; Peng, Z.; Zhou, L.; Chen, Y.; Huang, P.-H.; Truica, C. I.; Drabick, J. J.; El-Deiry, W. S.; Dao, M.; et al. Acoustic Separation of Circulating Tumor Cells. *Proceedings of the National Academy of Sciences.* 2015, *112* (16), 4970–4975.

(23) Marty, F.; Rousseau, L.; Saadany, B.; Mercier, B.; Français, O.; Mita, Y.; Bourouina, T. Advanced Etching of Silicon Based on Deep Reactive Ion Etching for Silicon High Aspect Ratio Microstructures and Three-Dimensional Micro- and Nanostructures. *Microelectronics Journal*. 2005, 673–677.

(24) Franssila, S. Ch. 17; Bonding. *Introduction to Microfabrication.* 2010, 191-201.

(25) Rogers, T.; Kowal, J. Selection of Glass, Anodic Bonding Conditions and Material Compatibility for Silicon-Glass Capacitive Sensors. *Sensors Actuators, A Physics.* 1995. 46 (1-3), 113-120.

(26) Chen, J.; Carter, M. B.; Edwards, B. S.; Cai, H.; Sklar, L. A. High Throughput Flow Cytometry Based Yeast Two-Hybrid Array Approach for Large-Scale Analysis of Protein-Protein Interactions. *Cytometry Part A.* 2012, *81A* (1), 90–+.

(27) Baptista, F. G.; Filho, J. V. Optimal Frequency Range Selection for PZT Transducers in Impedance-Based SHM Systems. *IEEE Sensors Journal.* 2010, *10* (8), 1297–1303.

(28) Piyasena, M. E.; Suthanthiraraj, P. P. A.; Applegate, R. W.; Goumas, A. M.; Woods, T. A.; López, G. P.; Graves, S. W. Multinode Acoustic Focusing for Parallel Flow Cytometry. *Analytical Chemistry.* 2012, *84* (4), 1831–1839.

(29) Novak, J.; Georgakoudi, I.; Wei, X.; Prossin, a; Lin, C. P. In Vivo Flow Cytometer for Real-Time Detection and Quantification of Circulating Cells. *Optics Letters.* 2004, *29* (1), 77–79.

(30) Wang, H.-W.; Bao, N.; Le, T. L.; Lu, C.; Cheng, J.-X. Microfluidic CARS Cytometry. *Optics Express.* 2008, *16* (8), 5782.

(31) Goodwin, P. M.; Ambrose, W. P.; Martin, J. C.; Keller, R. a. Spatial Dependence of the Optical Collection Efficiency in Flow Cytometry. *Cytometry.* 1995, *21* (2), 133–144.

(32) Rayleigh, Lord. On the Circulation of Air Observed in Kundt's Tubes, and on Some Allied Acoustical Problems. *The Royal Society.* 1884, *175* (1884), 1–21.

(33) Kundt, A. III. Acoustic Experiments. *London, Edinburgh, Dublin Philosophy Magazine and Journal of Science.* 1868, *35* (234), 41–48.

(34) Sadhal, S. S. Acoustofluidics 15: Streaming with Sound Waves Interacting with Solid Particles. *Lab on a Chip.* 2012, *12* (15), 2600.

(35) Sadhal, S. S. Acoustofluidics 16: Acoustics Streaming near Liquid–gas Interfaces: Drops and Bubbles. *Lab on a Chip.* 2012, *12* (16), 2771.

(36) Li, H.; Olsen, M. G. MicroPIV Measurements of Turbulent Flow in Square Microchannels with Hydraulic Diameters from 200 Mm to 640 Mm. *International Journal of Heat Fluid Flow.* 2006, *27* (1), 123–134.

(37) Antfolk, M.; Laurell, T. Continuous Flow Microfluidic Separation and Processing of Rare Cells and Bioparticles Found in Blood – A Review. *Analytical Chemistry*. 2017, 9–35.

Chapter 6: Development Towards a Lab in a Syringe: Acoustic Trapping of Negative Contrast Particles for Biomarker Detection

Frank A. Fencl[1], Aidira Macias Gonzales[1], Jaylene Martinez[1], Steven W. Graves[1], Nick J. Carroll[1], Gabriel P. Lopez[1]

[1]Department of Chemical and Biological Engineering, Center for Biomedical Engineering, University of New Mexico, Albuquerque, NM

6.1 Abstract

The global healthcare demand is in growing need of highly specific point-of-care (POC) testing. Developing portable handheld devices that can accurately help diagnose ailments outside of reference laboratory settings is critical for less developed areas that do not have access to these amenities. Combining the simple yet robust method of separating particles from a blood solution via acoustofluidics and affinity capture microparticles, may aid in the development of such POC testing technologies. We have developed a POC acoustofluidic microparticle-based affinity capture assay using biofunctionalized negative acoustic contrast particles and a simple syringe-like device. We study the affinity capture and separation from positive acoustic contrast media viability at various concentrations of dilute porcine blood. This study demonstrates that acoustofluidics in combination with specialized microparticles will aid in the development of a syringe-like handheld POC affinity capture assay.

6.2 Introduction

Acoustofluidics, the combination of acoustophoresis and microfluidics, has proven a reliable tool for biological media interrogation and component separations.[1–3] Acoustofluidic technologies provide a gentle non-contact method for microsphere and media separations and analysis.[4–6] Among the many applications of acoustofluidic assays, microsphere-based assays have proven useful for both analysis of molecular components with minimal preparation and separation of functionalized surfaces.[7,8] Microparticle assays have also proven to be useful for point-of-care (POC) testing applications.[9] Combining the high fidelity of acoustofluidics media separation with the specificity of microparticle biomolecular detection may greatly enhance point-of-care testing platforms.[10]

The fundamental principles of acoustophoresis, or the manipulation of particles with an acoustic standing wave, have been well defined. The position of particles within an acoustic field is due to their physical response to the primary acoustic radiation force. The response of the particle to the primary acoustic radiation force is due to the intrinsic physical properties of the particle and medium.[11–14] The Force (F) scales directly with the particle's size (V_p), the amplitude of the acoustic pressure (P), the wavenumber (k), the particle's location in the channel (x), and the fluid medium's compressibility (β_m). The wavelength of the acoustic force (λ) scales inversely (Equation 1). In addition to these variables, the acoustic contrast factor [$\Phi(\beta,\rho)$] largely determines the particle location within the acoustic standing wave at equilibrium.

$$F = -\frac{(\pi P^2 V_p \beta_m)}{2\lambda}\phi(\beta,\rho)\sin 2kx \qquad \text{Equation 1}$$

where,

$$\phi(\beta,\rho) = \frac{5\rho_p - 2\rho_m}{2\rho_p + \rho_m} - \frac{\beta_p}{\beta_m}$$

The acoustic contrast factor determines whether the particle exhibits a negative or positive acoustic contrast. Particles with a density (ρ_p) higher than that of the surrounding fluid medium's (ρ_m), and a lower compressibility (β_p) compared to the medium (β_m), will exhibit a positive acoustic contrast, while those with a lower density and higher compressibility will exhibit a negative contrast value. Particles with a negative acoustic contrast will move toward the pressure antinode of the acoustic standing wave, while particles with a positive acoustic contrast factor will move to the pressure node.[15–17]

Previous work using acoustophoretic microparticle focusing has largely been done using positive acoustic contrast (PAC) beads. Some of the more commonly used and commercially available microparticle materials for bio-assays are silica, glass, metals, polystyrene and other materials that exhibit PAC. These materials are used for various bioassays as they have surfaces that can be readily functionalized with different biological molecules.[8,18,19] PAC particles were used for their acoustofluidic properties to focus beads in the first acoustic flow chambers for flow cytometry.[13] Blood and other biological cells typically exhibit positive acoustic contrast which was explored in the 1990's by Yasuda et al. to develop compact acoustofluidic flow chambers for red blood cell enrichment.[20]

As blood and most other biological media exhibit PAC, research has been done to acoustically separate specific components out of whole blood solutions. In 2013, an article by Cushing et al. demonstrated the use of elastomeric negative acoustic contrast particles (NACPs or NACs) with biofunctionalized surfaces to bind to prostate specific antigen and separate from red blood cells in solution.[16] The synthetic polydimethylsiloxane (PDMS) particles presented provide a simple low-cost method of synthesizing NAC particles. PDMS is an ideal material for biological assays as it is a non-toxic, biocompatible material.[21,22] Additional literature by the group demonstrated NAC to binding to target positive contrast particles and separation from other solution components.[17]

One of the current limitations in acoustofluidic assays is that individual molecules are impossible to focus. To overcome the difficulties of molecular focusing, microparticle affinity capture assays are desirable. Antibodies have proven capable model biomarkers for many antigenic studies and have been shown to functionalize on the surface of microparticles[10,23,24]. Microparticle-based systems have illustrated high flexibility and complexity as well as the ability to test for multiple analytes in parallel (defined as multiplexing).[25–27]

Here we explore the use of elastomeric negative acoustic contrast microspheres (NACs) that focus at the anti-nodes of an acoustic standing wave within a compact handheld syringe-based device. Using a round glass capillary coupled with a 1.5 MHz piezoelectric lead zirconate titonate (PZT) transducer, we assembled a device to capture labeled antibodies on biofunctionalized NACs and filter undesired positive contrast components out of a solution. This method provides a useful portable tool to capture desired components out of solution for measurements using methods such as fluorescence microscopy, flow cytometry, or fluorimetry. We present the use of NACs for rapid separations and molecular assays using fluorescently labeled antibodies as an ideal biomarker within various concentrations of dilute porcine whole blood to demonstrate the development towards a handheld syringe-like device for POC testing applications.

6.3 Materials and methods

6.3.1 Synthesis of elastomeric negative acoustic contrast particles (NACs)

Polydispersed Population synthesis. Bulk NACs are synthesized largely as done previously.[16] 5 g of ratio of 10:1 pre-polymer to curing agent of Sylgaurd 184

Polydimethylsiloxane (PDMS) is prepared for bulk synthesis. For fluorescent imaging of the NACs, we stained the PDMS by adding 50 µL of 17 mg/mL in acetone solution of Nile Red (NR) to the 5 g of PDMS mixture. The 5 g mixture is submerged into 50mL of 1% w/v Cetyltrimethyammoniumbromide (CTAB) in Millipore filtered water. The solution is shaken and vortexed for ~5 minutes to create a polydispersed emulsion of PDMS drops in CTAB solution. The solution is then placed in a 60 ^oC oven for 2 hours to cure. The resulting solution is filtered using a 30 µm an then 20 µm Nylon filter attached to a 60 mL plastic syringe. Particles are collected within the 20-30 µm range on the 20 µm filter. The resulting population of cured CTAB-PDMS particles are counted using a Z series Beckman Coulter Counter after being spun down and resuspended in PBS and 0.1% w/v albumin from bovine serum (BSA). The resulting concentration varies but is on the order of 1 X 10^5 particles/mL. This process is scalable if greater volumes of particles are desired.

6.3.2 Biofunctionalization of NACs

1 mL of 20-30 µm filtered NACs are spun down at 7500 rpm for 3 minutes and resuspended in 0.1% BSA and 138 mM Phosphate buffered saline (1 X PBS) twice for washing. The BSA is added to ensure NACs do not clump. 3 mg of avidin is added to the solution and incubated for 16 hours overnight (enough time for adequate passive adsorption of avidin onto the NAC surface). The solution is washed again in 0.1% BSA and 1X PBS after incubation to remove excess avidin. 0.8 mL of NAC solution with 0.2 mL 8.7 pH $NaCO_3$ is aliquoted into a microcentrifuge tube and 5 µL of 0.5 mg/mL primary Antibody (biotinylated Mouse Anti-Human IgG_1 from BD Biosciences) is incubated with the NACs for 30 minutes at room

temperature and 200 µL. The basic pH is aids in biotinylation of the primary Ab to avidin. After incubation the NACs with primary Ab are washed in 1 mL 0.1% BSA in 1X PBS and spun down at 7500 rpm for 3 minutes to remove excess primary Ab. The solution is brought to 1 mL 0.1% BSA in 1X PBS. An illustration of to biofunctionalized surface can be seen in the supporting information for this chapter (Appendix D).

Affinity capture target secondary antibody (polyclonal FITC labeled Goat anti-mouse Ig from BD Biosciences; GAM-FITC) is purchased with FITC label for fluorescence detection and imaging. Biofunctionalized NACs are suspended in 1 mL buffer solution (1X PBS + 0.1% BSA) and incubated with 6 µL of 0.2 mg/mL GAM-FITC in PBS and 0.1% sodium azide over 45 minutes to allow antibody binding interaction. See below for details on incubation within various dilute blood concentrations. Illustration of biomolecular complex can be seen in the supporting information for this chapter (Appendix D). We verified binding using epifluorescence microscopy (Appendix D).

6.3.3 Device assembly and imaging platform

A 1 / 0.58 OD/ID (mm) round glass capillary from World Precision Instruments is cut with a diamond pen to a 6.2 cm length and coupled to the 5 mL plastic syringe via 2.38 / 0.79 OD/ID (mm) Tygon tubing. A 1 x 3 x 29.5 mm lead zirconate titanate (PZT) piezoelectric ceramic is attached to the cylindrical capillary with adhesive for acoustic actuation. For microscopy, the capillary is taped to PDMS blocks on a glass slide. An amplifier coupled to an Agilent Technologies 33250A Function/Arbitrary Waveform Generator supply's the acoustic signal to the PZT. For infusion of solutions at a constant flow rate, the syringe is attached to a Chemyx Inc. syringe pump, Model: N300. Imaging is performed using an Andor camera on a Zeiss epifluorescence Microscope (MODEL NO. DL-658M-TIL). Schematic of setup is found in the supporting information for this chapter (Appendix D).

6.3.4 Trapping efficiency characterization

A solution of unstained NACs was synthesized as described previously and filtered manually using 30, 20 µm Nylon filters through a 60 mL BD plastic syringe. The particles were collected from the filter holder following 20 µm filtering assuring a particle distribution between 20-30 µm. 5 mL of particle solutions was spun down (7500 rpm for 3 min) to a pellet and resuspended in 5 mL of 0.1% BSA in 1X PBS solution buffer. Particles were counted using a Z Series Coulter Counter three times at a yield of 6×10^5 particles/mL. To measure trapping efficiency, we infused the particles from the 5 mL BD plastic syringe at a rate of 200 µL/min through the 1 / 0.58 OD/ID (mm) capillary with PZT actuator. The frequency was set to 1.59 MHz and amplitude of ~15 Vpp. The particles were observed to trap and clump over 25 minutes until the 5 mL was expended. The resulting solution was collected after trapping. The solution was counted three times to assess the number of NACs that did not trap. 2.5×10^3 particles/mL were counted, which made it into the collection vial (20 mL scintillation vial) after trapping. The efficiency is calculated as the average amount of particles collected during trapping divided by the total number (counted before trapping) multiplied by 100. The calculated efficiency is 95.8% of particles remained within the capillary and 4.2% were expelled during acoustic actuation.

6.3.5 NAC trapping in the presence of PAC polystyrene particles

As a proof of principle, we wanted to demonstrate the behavior of positive acoustic contrast media focusing in conjunction with trapping of Nile Red (NR) stained NACs in our capillary device. To demonstrate the particle behavior, we used a concentration of 5×10^5 10 µm NR stained polystyrene particles (positive acoustic contrast media) with the 6.6×10^5 NR stained NACs in 5 mL total volume of solution buffer. The solution was infused from a 5 mL plastic syringe at 200 µL/min through the capillary device with PZT actuation at a frequency of 1.59 MHz and ~15 Vpp voltage. Fluorescent images were collected by the Andor camera on the epifluorecence microscope setup.

6.3.6 Acoustic trapping biomarker assay and separation in dilute Nile red stained porcine red blood cells

We demonstrate the separation of FITC labeled secondary Ab on NACs from NR stained porcine red blood cells (prbcs) through fluorescence microscopy. To stain the red blood cells with NR, we followed a protocol by Greenspan et al. by adding 10 µL of 17 mg/mL NR in acetone to 100 µL of 1X PBS washed prbcs.[28] Removing the serum from the blood is necessary because the proteins present in whole blood serum have a higher affinity for the dye and thus draw NR out of the blood cell membranes. The blood cells are incubated on rotisserie for 30 min to ensure diffusion of NR into the membrane. After incubation the suspension is further washed in 1X PBS to remove excess NR. We added 5 µL of the stained prbcs to 1 mL of 6×10^5 NACs with secondary Ab (polyclonal FITC labeled Goat anti-mouse Ig from BD Biosciences) in buffer solution and acoustically separated the contents in our capillary device at a flow rate of 150 µL/min. The transducer was actuated at 1.646 MHz and ~15 Vpp to trap NACs and focus the positive acoustic contrast red blood cells. Images were collected on the previously mentioned epifluorescence microscope. It should be noted that after several minutes the PDMS NACs begin to draw NR out of the stained prbcs, more on this is described in the discussion.

6.3.7 Acoustic trapping biomarker assay and separation in varying concentrations of dilute porcine blood

To demonstrate capture of a FITC labeled secondary antibody in the presence of whole blood media we ran four varying solutions of dilute porcine whole blood (SWB), 0.5, 1, 5, and 50% w/v in buffer solution with our biofunctionalized NACs. A solution of 6.6 x 10^5 particles/mL biofunctionalized NACs are aliquoted in a 1 mL (or 500 µL for 50% SWB) volume in 0.1% BSA in 1X PBS buffer solution. A 6 µL solution of 0.2 mg/mL secondary labeled antibody (FITC-polyclonal Goat anti-mouse IgG from BD Biosciences), model biomarker, is added separately to 5, 10, 50, and 500 µL porcine whole blood in Heparin Sodium from Animal Tech. The solution of blood and secondary Ab is vortexed prior to adding NACs in buffer solution to 1 mL total volume for each sample and incubated, covered, for 45 minutes at room temperature on rotisserie. Separately, 5% w/v SWB was incubated with secondary Ab and NACs for 3.25 hrs. to observe binding over a longer incubation period. The solution is taken up into the syringe after incubation and then infused into a collection vial (1.5 mL centrifuge tube) at volumetric flow rate of 200 µL/min. The PZT is actuated prior to infusion with an applied power of ~15 Vpp at a frequency of 1.646 MHz. The NACs are trapped while the positive acoustic contrast media, porcine RBCs and excess unbound secondary Ab, flow into the collection vial. A secondary solution of 1X PBS + 0.1% BSA buffer solution is withdrawn into the syringe as an additional wash to evacuate excess porcine blood media. After the wash with buffer solution, an additional 500 µL buffer solution is withdrawn to flow out, with PZT off, the trapped NACs and the captured Ab for counting and image analysis with the epifluorescent microscope. For sample imaging, we washed solutions of particles by centrifugation (7500 rpm for 3 min) to remove excess unbound secondary Ab to minimize background fluorescence.

As a negative control, 6.6 x 10^5 particles/mL NACs without primary Ab functionalization are ran in 1 mL volume of 0.5 % w/v SWB diluted in 0.1% BSA in 1X PBS. Another solution of 6 µL from 0.2 mg/mL secondary FITC labeled antibody is added to the blood prior to mixing with the NACs and incubated for 45 minutes, covered, at room temperature to test for nonspecific biomarker adsorption. Negative control particles are collected and analyzed by the same method as described above.

6.4 Results and discussion

6.4.1 NAC particle solution preparation

NACs are prepared in bulk solution of 1% w/v CTAB to yield polydisperse populations of particles. It was observed that lower concentrations of the CTAB surfactant yield larger particles (0.5, 0.05% w/v CTAB in Millipore filtered water was experimented with). As was found by Cushing et al., the uncoated silicone particles tend to clump after washing out excess CTAB therefore, due to their hydrophobic surfaces, we added 0.1% BSA in buffer to facilitate particle stability and reduce the clumping effect.[16] We also found albumin from bovine serum (BSA) at 1% w/v was found to work as a biocompatible surfactant for the NACs in place of CTAB. Further work is needed to evaluate efficacy of BSA as an ideal surfactant for the synthesis of these particles.

6.4.2 NAC trapping from positive contrast media

Robust NAC particle trapping occurs with high reproducibility in our system. Negative acoustic contrast PDMS microparticles move to the anti-nodes of an acoustic standing wave generated by a PZT transducer on our glass capillary and cluster due to secondary acoustic forces while ~5% of the NACs flow out of the device (Figure 6.1). Over the course of the trapping and separation, NACs tend to trap immediately as they enter the glass capillary in discrete regions along the walls upstream of the PZT while positive acoustic contrast media will stay unfocused until passing over the PZT transducer (depiction of focused prbcs can be seen in Figure 6.1 G). Laminar flow profiles within the capillary carry focused PAC media in the center (nodal region) of the capillary as they pass over the PZT. This can be observed with NR stained polystyrene particles in Figure 6.1 B-F. The pressure node and anti-node regions of the resonant acoustic standing wave within the device are determined by the drive frequency of the PZT. At ~1.6 MHz there is a single node and two anti-nodes within the cylindrical capillary. We demonstrate the separation and trapping of the NACs from PAC media in the presence of NR polystyrene microspheres, NR stained prbcs, and in various w/v fractions of whole porcine blood. While our experiments held the number of buffer rinses and subsequent trapping and separation constant at two, it should be noted that further washes within the capillary device are possible while keeping in mind the constant ~5% loss of NACs during each run.

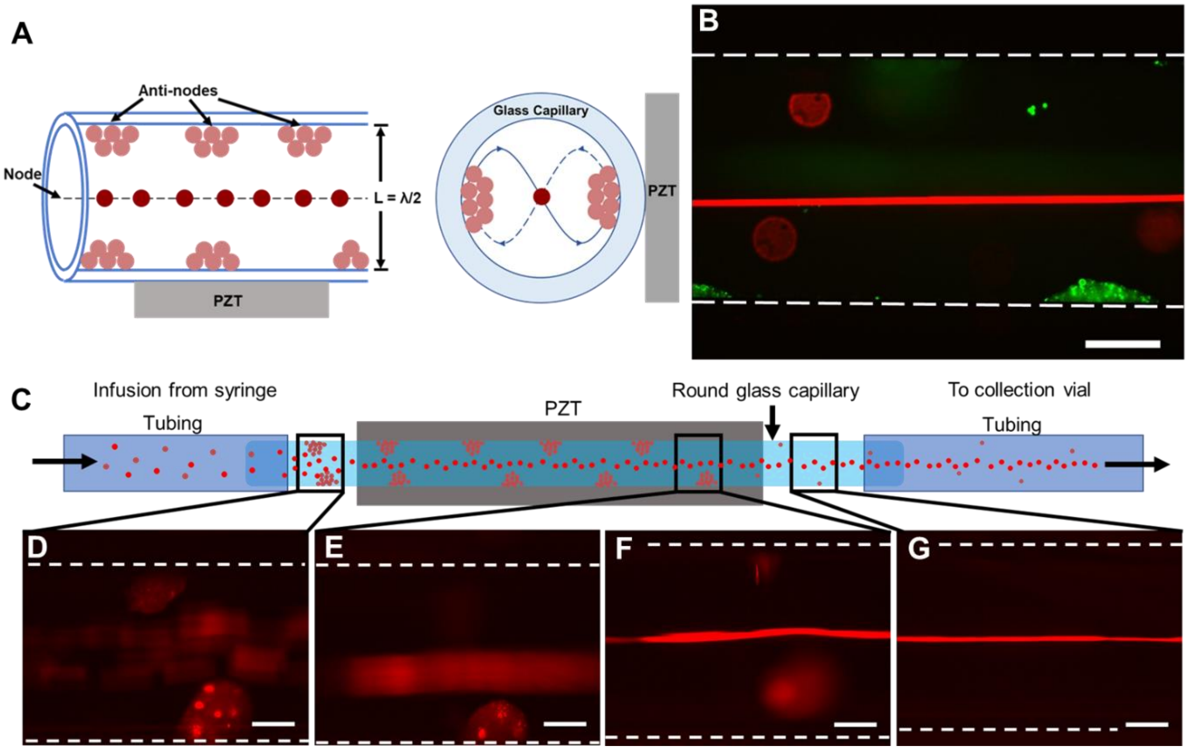

Figure 6.1. Illustration and images of NAC trapping in capillary device. (A) side view and cross section of capillary device with PZT transducer actuated. Negative acoustic contrast silicone particles focus at antinodes and positive acoustic contrast particles focus within the node of the resonant acoustic standing wave. (B) Representative fluorescence overlay image of 6 x 10^4 particles/mL NACs (green) trapping in antinode regions of glass capillary in the presence of focused 10 µm NR polystyrene particles (scale bar = 200 µm). (C) Schematic and insets from various locations across the capillary corresponding to fluorescent image locations. (D-G) Red channel fluorescent images of 6 x 10^5 NR stained NACs and 5 x 10^5 NR polystyrene PAC particles flown at 200 µL/min in buffer solution. Dashed lines represent capillary walls (scale bars = 200 µm). (D) Image at capillary upstream of PZT. (E) Image at distal position on capillary over PZT focused on NACs and (F) on polystyrene particles. (G) Image of focused polystyrene particles downstream of PZT.

6.4.3 Separation of affinity capture NACs from Nile red stained porcine red blood cells

For the purposes of demonstrating separation from red blood cells, we suspended a 1 mL solution of primary Ab labeled NR-NACs, 0.5% w/v NR stained prbcs, and secondary capture target Ab (GAM-FITC). The solution was washed after incubation to remove excess secondary unbound FITC-Ab to reduce background for fluorescence imaging. We ran the solution through the capillary device and captured images of NACs trapping with secondary Ab and separating from focused NR-prbcs. The NR-prbcs appear dim in the images likely due to the diffusion of NR into our NACs. Images of antibody captured NACs trapping and separating from NR-prbcs can be seen in Figure 6.2. We explored this by forming a solution of unstained NACs with secondary Ab already bound and ran them through the device with NR stained prbcs. Theoretically, the labeled NACs should have only shown in the green fluorescence channel and not in the red channel with the NR stained prbcs but we found that after a short period of time, on the order of minutes, the NR diffused into the NACs. We verified this by incubating the particles without NR in a solution of 0.5% NR stained prbcs (washed to remove excess dye) for 45 minutes and observed red fluorescence within the NACs. Over time the dye within the red blood cell membrane diffuses out until they are too dim to image in the presence of NACs.

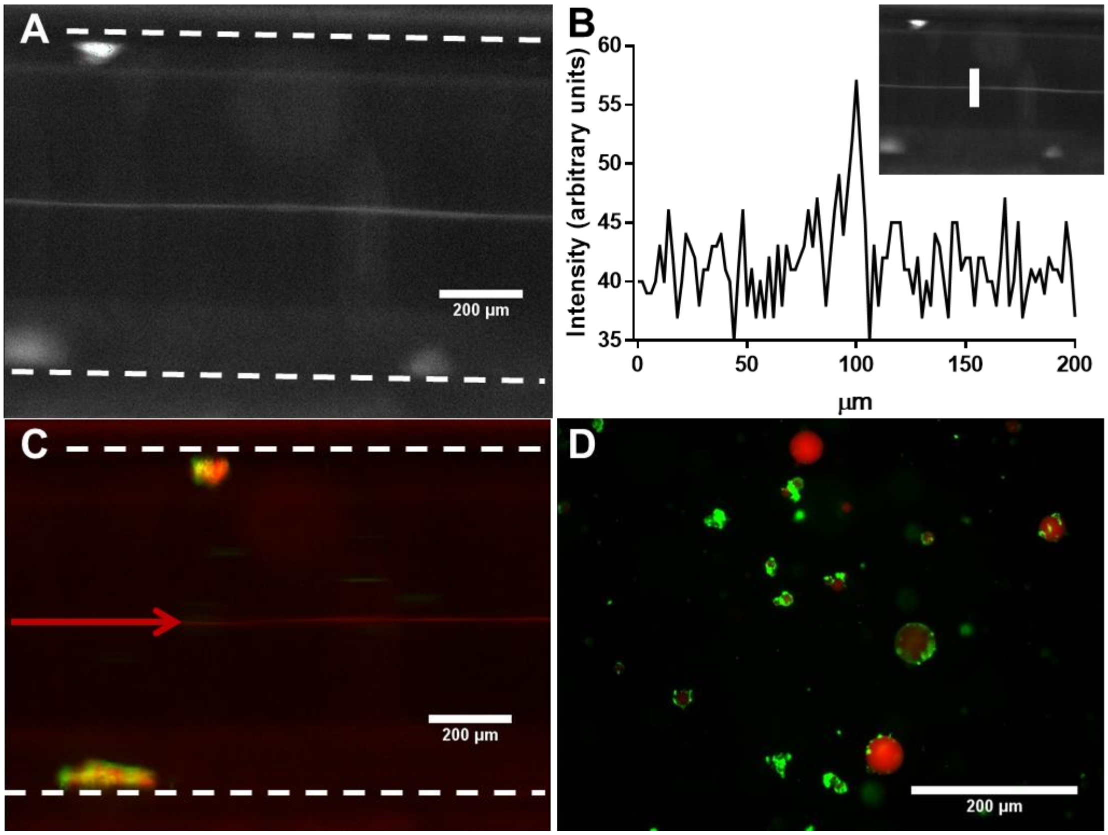

Figure 6.2. Capture assay of biofunctionalized NACs from purified NR stained prbcs in buffer solution. (A) Greyscale enhanced contrast red fluorescence channel image of NR-NACs trapping at capillary walls in the presence of focused dim NR-prbcs (center). (B) Fluorescence intensity line plot of NR-rbcs within a 200 µm region of panel image A (inset). (C) Overlay of red and green channel fluorescence of affinity capture NACs in the presence of NR-prbcs. Red arrow illustrating location of focused NR-rbcs and direction of flow. (D) 20X magnification red/green channel fluorescence overlay of NR-NACs with captured FITC-labeled secondary Ab after separation in microcapillary device on glass slide. Dashed lines represent capillary walls. Scale bars = 200 µm.

6.4.4 Dilute blood affinity capture assay at various whole blood concentrations dilute blood solutions and negative control

To assess the viability of our platform for POC testing, we tested the limit of detection of our model Ab (FITC-goat anti-mouse IgG) within various dilute blood samples. As a negative control, we incubated NACs without Avidin-biotinylated MAH primary Ab to test for non-specific interaction. Our results indicate the FITC-GAM secondary Ab does not visually non-specifically adsorb onto our particles. Each dilute blood experiment was washed within our device two times with buffer solution to acoustically separate and collect red blood cells while trapping NACs with captured target FITC-GAM secondary Ab.

Affinity capture of GAM-FITC and blood component interactions

While polyclonal IgG (our capture target secondary Ab) exists as a major component within whole blood, we wanted to model the capability of detection at concentrations lower than biological (0.001 experimental vs. 1.0 mg/mL biological) to imitate a concentration of less prevalent targets. IgG accounts for ~75% of serum antibodies (1.0 mg/mL) found in human whole blood which facilitates the immune system's early detection and elimination of various pathogens.[29–31] The presence of proteins and other compounds within whole blood inhibit detection of specific ligands due to passive adsorption of the proteins onto the hydrophobic surface of our NACs effectively blocking the Ab interactions. Previous work with these NACs showed detection in the presence of 10% extracted plasma and separately in 0.1% SWB.[16] We used a higher starting concentration of whole blood (0.5%) as well as subsequently higher concentrations, 1, 5, and 50%, w/v thereafter. Prior to acoustic separation within the capillary, each solution was incubated with target Ab and whole blood for 45 min. To simulate steps involved in a handheld device, we infused each sample with acoustic actuation to trap labeled NACs and remove red blood cell effluent. After infusion, 1 mL buffer was taken up into the device for additional red blood cell removal. This process was repeated two times. As seen in Figure 6.3, NACs in 1% and 0.5% w/v SWB bind to our target secondary Ab. At 5% and higher whole blood concentrations, the various components within whole blood block the binding of our secondary Ab.

We wanted to observe if longer incubation periods, 3.25 hrs. (as opposed to the previous 45 min incubation), would allow the target Ab to bind given that components in blood desorb in the presence of competitive binding for our 5% whole blood solution (our observed upper limit of affinity Ab capture).[32,33] Due to the specificity of our Ab interactions, we hypothesized that given a longer period incubation, the secondary Ab would adsorb and bind to our biofunctionalized NACs while nonspecific adsorption would be reduced. Our observations of the resulting solution of NACs show that some component within the whole blood prevents our secondary Ab from binding possibly due to another protein component within the blood having higher affinity for the hydrophobic surfaces of our NACs. Very little to no fluorescence was observed on the surfaces after the longer incubation period for 5% whole blood as seen in Figure 6.3. The small amount of bound secondary Ab was observed in small aggregates of NACs after washing excess supernatant with unbound Ab.

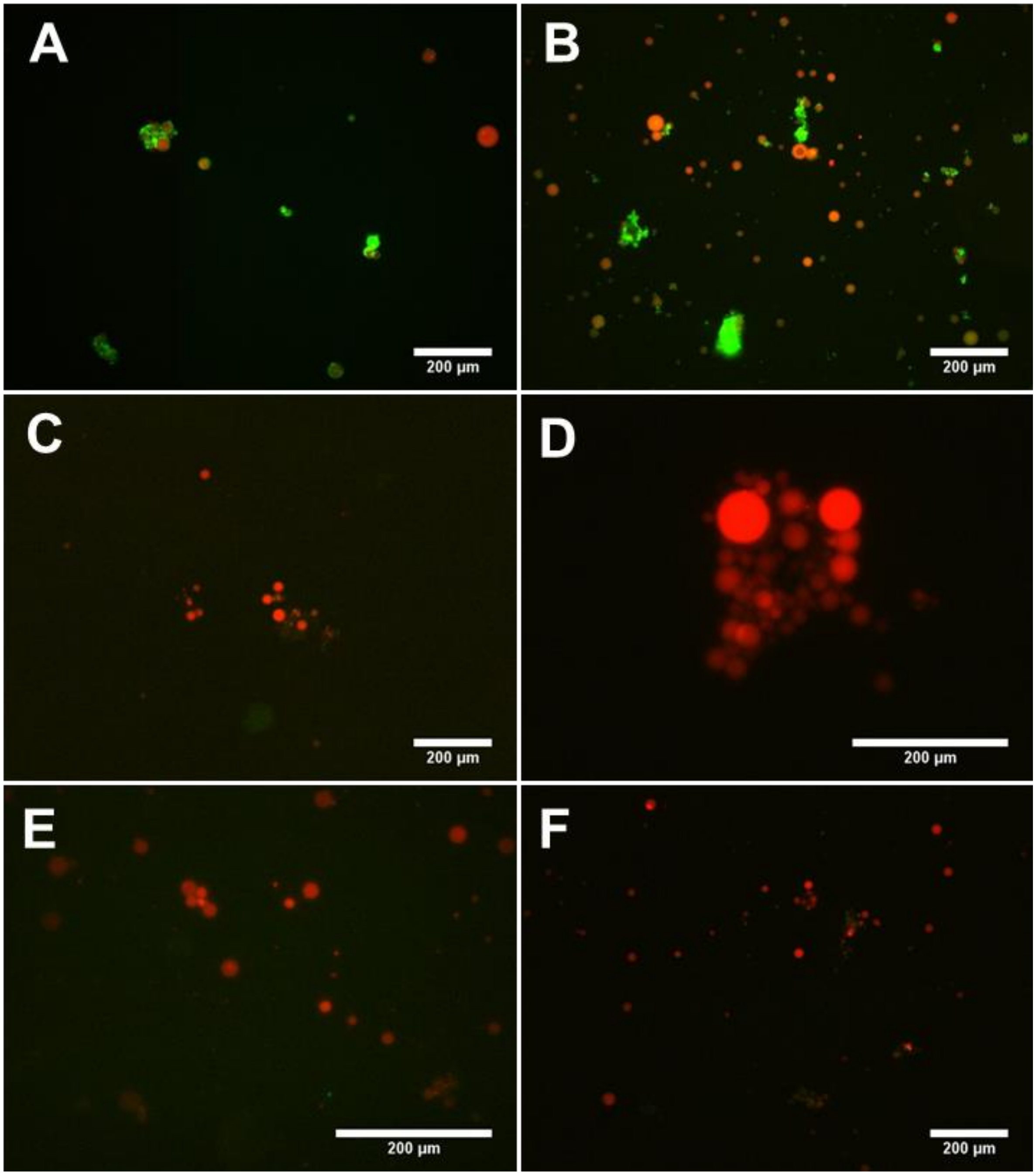
A
200 µm
B
200 µm
C
200 µm
D
200 µm
E
200 µm
F
200 µm

Figure 6.3. Affinity capture in the presence of various dilute blood concentrations. Each red and green fluorescence channel overlay image is of a washed sample after 45 min incubation (with exception of E) and 2 acoustic separation buffer washes within the capillary device. (A) NR stained NACs after affinity capture of FITC labeled secondary Ab (green) in the presence of 0.5% SWB. (B) NR stained NACs after affinity capture of FITC labeled secondary Ab (green) in the presence of 1% SWB. More particles can be seen without green capture target Ab. (C) NR-NACs exhibiting minimal to no capture of secondary Ab after incubation in 5% SWB. Small clusters of NACs exhibit low amounts of green secondary Ab captured. (D) NR-NACs cluster at higher magnification exhibiting no capture of secondary Ab in after incubation in 50% SWB. (E) Negative control; incubation of non-biofunctionalized NR-NACs, secondary Ab, and 0.5% SWB exhibiting no green capture target Ab on the surfaces. (F) 3.25 hrs. incubation of NR-NACs in the presence of 5% SWB and secondary Ab. After longer incubation at 5% SWB, no increased fluorescence signal for secondary Ab was observed. Scale bars = 200 µm.

To further asses the lower limit of detection at the working concentrations of dilute porcine whole blood, a fluorescence calibration curve via flow cytometry needs to be incorporated in future work.

6.4.5 Particle Counts After Trapping and Separation from Dilute Porcine Whole Blood

To determine the amount of prbcs expelled with our trapped NAC contents, we collected and tested the solutions after the second buffer wash. In an ideal system a greater portion of the volume of whole blood would be expelled after each trapping experiment however due to the physical limit of the syringe pump and dead volume within the capillary and tubing, we keep a calculated (based on device component dimensions) ~493 µL volume within the syringe, capillary device, and tubing. Approximately half of the total tested volume is not expelled from the device.

The additional buffer wash steps are therefore necessary to aid in the removal of excess blood media. Our results illustrate that a large amount of the red blood cells is expelled as waste during trapping experiments, however it should be noted that the Coulter Counter does not discern between NACs and prbcs at the 6-10 µm (prbc size) set range of detection meaning our resolution is limited to the particle sizes (Figure 6.4).

While our filtering process during NACs preparation removes a large volume of silicone particles less than 20 µm in diameter, some smaller particles remain within the collected region that stick to larger particles as is evident from observations of NAC clusters. Of the ~500 µL of contents that are expelled, it can be seen in Figure 6.4 that a majority of prbcs are focused out of the device for each run. Future improvements to the system will eliminate the dead volume of unprocessed sample. The future goal is to advance the platform to a completely handheld syringe with PZT-capillary needle which will greatly reduce the amount of unprocessed volume evident within the tubing. Our preliminary work illustrates that the NACs trap and separate from whole blood media and remain within the capillary while the red blood cells will flow to the collection vial.

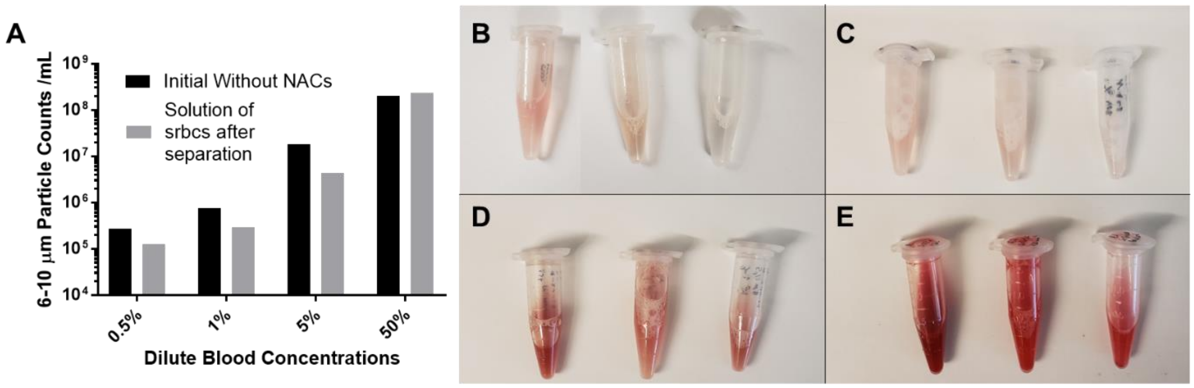

Figure 6.4. Porcine red blood cell collection during acoustic separation experiments. (A) Bar graph of 6-10 µm particle counts for initial blood cell concentrations (black) without NACs at 0.5, 1, 5, 50% w/v dilute SWB in buffer solution vs. 6-10 µm counts of effluent blood cells after first trapping (grey). (B) Recovered solutions of 0.5% SWB experiments after initial trapping (left), first buffer wash (middle), and collection of NACs and residual blood after second wash (right). (C) Recovered solutions of 1% SWB after initial trapping (left), first buffer wash (middle), and collection of NACs and residual blood after second wash (right). (D) Recovered solutions of 5% SWB after initial trapping (left), first buffer wash (middle), and collection of NACs and residual blood after second wash (right). (E) Recovered solutions of 50% SWB after initial trapping (left), first buffer wash (middle), and collection of NACs and residual blood after second wash (right). Reduction of prbcs in total volume is evident from the decrease in red observed from subsequent collections.

6.5 Conclusions

We present work towards the development of a simple, low-cost lab in a syringe assay using our engineered negative acoustic contrast particles for the purposes of POC testing. Our work illustrates the potential to detect specific biomarkers within a biological solution for the purposes of detecting early onset of infection by applying an acoustic standing wave to a sample mixed with our specialized microparticles within a cylindrical glass capillary for separation from positive acoustic contrast media. We demonstrate affinity capture of fluorescently labeled antibodies in the presence of up to 1% w/v porcine whole blood. Separating red blood cells and other components reduces interference to enhance fluorescence signal on the surfaces of our NACs for downstream analysis. Future work includes synthesis of monodispersed populations of NACs which will aid in the discrimination from red blood cells during analysis and counting. We are incorporating glass capillary microfluidics and oil-in water emulsion techniques to generate monodispersed populations of PDMS drops (see supporting info in Appendix D). Additional work will improve on the device design by eliminating the dead volume between the capillary, syringe, and collection vial to increase the efficiency of positive acoustic contrast media removal from our target trapped NACs.

6.6 References

(1) Lenshof, A.; Magnusson, C.; Laurell, T. Acoustofluidics 8: Applications of Acoustophoresis in Continuous Flow Microsystems. *Lab on a Chip.* 2012, *12* (7), 1210.

(2) Wiklund, M. Acoustofluidics 12: Biocompatibility and Cell Viability in Microfluidic Acoustic Resonators. *Lab on a Chip*. 2012, 12 (11), 2018-2028

(3) Fu, Y. Q.; Luo, J. K.; Nguyen, N. T.; Walton, A. J.; Flewitt, A. J.; Zu, X. T.; Li, Y.; McHale, G.; Matthews, A.; Iborra, E.; et al. Advances in Piezoelectric Thin Films for Acoustic Biosensors, Acoustofluidics and Lab-on-Chip Applications. *Progress in Materials Science*. 2017, (89), 31-91.

(4) Travagliati, M.; Shilton, R. J.; Pagliazzi, M.; Tonazzini, I.; Beltram, F.; Cecchini, M. Acoustofluidics and Whole-Blood Manipulation in Surface Acoustic Wave Counterflow Devices. *Analytical Chemistry.* 2014, 86 (21), 10633–10638.

(5) Ahmed, H.; Destgeer, G.; Park, J.; Jung, J. H.; Ahmad, R.; Park, K.; Sung, H. J. A Pumpless Acoustofluidic Platform for Size-Selective Concentration and Separation of Microparticles. *Analytical Chemistry.* 2017, 89 (24), 13575–13581.

(6) Antfolk, M.; Magnusson, C.; Augustsson, P.; Lilja, H.; Laurell, T. Acoustofluidic, Label-Free Separation and Simultaneous Concentration of Rare Tumor Cells from White Blood Cells. *Analytical Chemistry.* 2015, 87 (18), 9322–9328.

(7) Shi, J.; Ahmed, D.; Mao, X.; Lin, S. C. S.; Lawit, A.; Huang, T. J. Acoustic Tweezers: Patterning Cells and Microparticles Using Standing Surface Acoustic Waves (SSAW). *Lab on a Chip.* 2009, 9 (20), 2890-2895.

(8) Whitaker, M. J.; Hao, J.; Davies, O. R.; Serhatkulu, G.; Stolnik-Trenkic, S.; Howdle, S. M.; Shakesheff, K. M. The Production of Protein-Loaded Microparticles by Supercritical Fluid Enhanced Mixing and Spraying. In *Journal of Controlled Release.* 2005, Vol. 101, 85–92.

(9) St John, A.; Price, C. P. Existing and Emerging Technologies for Point-of-Care Testing. *Clinical Biochemistry Reviews.* 2014, *35* (3), 155–167.

(10) Aliano, A.; Cicero, G.; Nili, H.; Green, N. G.; García-Sánchez, P.; Ramos, A.; Lenshof, A.; Laurell, T.; Qi, A.; Chan, P.; et al. Acoustic Contrast Factor. *Encyclopedia of Nanotechnology*. Springer Netherlands: Dordrecht. 2012; Vol. 548, 30–31.

(11) Gor'kov, L. P. Forces Acting on a Small Particle in an Acoustic Field within an Ideal Fluid. *Doklady Akademii Nauk. SSSR* 1961, *140* (1), 88–91.

(12) Bruus, H. Acoustofluidics 7: The Acoustic Radiation Force on Small Particles. *Lab on a Chip.* 2012, *12* (6), 1014.

(13) Goddard, G. R.; Sanders, C. K.; Martin, J. C.; Kaduchak, G.; Graves, S. W. Analytical Performance of an Ultrasonic Particle Focusing Flow Cytometer. *Analytical Chemistry.* 2007, *79* (22), 8740–8746.

(14) Bassindale, P. G.; Phillips, D. B.; Barnes, A. C.; Drinkwater, B. W. Measurements of the Force Fields within an Acoustic Standing Wave Using Holographic Optical Tweezers. *Applied Physics Letters.* 2014, *104* (16). 163504.

(15) Laurell, T.; Petersson, F.; Nilsson, A. Chip Integrated Strategies for Acoustic Separation and Manipulation of Cells and Particles. *Chemical Society Reviews*. 2007, 492–506.

(16) Cushing, K. W.; Piyasena, M. E.; Carroll, N. J.; Maestas, G. C.; López, B. A.; Edwards, B. S.; Graves, S. W.; López, G. P. Elastomeric Negative Acoustic Contrast Particles for Affinity Capture Assays. *Analytical Chemistry.* 2013, *85* (4), 2208–2215.

(17) Johnson, L. M.; Gao, L.; Shields IV, C.; Smith, M.; Efimenko, K.; Cushing, K.; Genzer, J.; López, G. P. Elastomeric Microparticles for Acoustic Mediated Bioseparations. *Journal of Nanobiotechnology.* 2013, *11* (1), 22.

(18) Darmanis, S.; Nong, R. Y.; Hammond, M.; Gu, J.; Alderborn, A.; Vänelid, J.; Siegbahn, A.; Gustafsdottir, S.; Ericsson, O.; Landegren, U.; et al. Sensitive Plasma Protein Analysis by Microparticle-Based Proximity Ligation Assays. *Molecular and Cellular Proteomics.* 2010, *9* (2), 327–335.

(19) Lee, H.; Kim, J.; Kim, H.; Kim, J.; Kwon, S. Colour-Barcoded Magnetic Microparticles for Multiplexed Bioassays. *Nature Materials.* 2010, *9* (9), 745–749.

(20) Yasuda, K.; Haupt, S. S.; Umemura, S.; Yagi, T.; Nishida, M.; Shibata, Y. Using Acoustic Radiation Force as a Concentration Method for Erythrocytes. *Journal of Acoustical Society of America.* 1997, *102* (c), 642–645.

(21) Lee, D. S.; Kim, S. J.; Sohn, J. H.; Kim, I. G.; Kim, S. W.; Sohn, D. W.; Kim, J. H.; Choi, B. Biocompatibility of a Pdms-Coated Micro-Device: Bladder Volume Monitoring Sensor. *Chinese Journal of Polymer Science. (English Ed.* 2012, *30* (2), 242–249.

(22) Peterson, S. L.; McDonald, A.; Gourley, P. L.; Sasaki, D. Y. Poly(Dimethylsiloxane) Thin Films as Biocompatible Coatings for Microfluidic Devices: Cell Culture and Flow Studies with Glial Cells. *Journal of Biomedical Materials Research. - Part A.* 2005, *72* (1), 10–18.

(23) Dincer, C.; Bruch, R.; Kling, A.; Dittrich, P. S.; Urban, G. A. Multiplexed Point-of-Care Testing – XPOCT. *Trends in Biotechnology*. 2017, 728–742.

(24) Ullal, A. J.; Reich, C. F.; Clowse, M.; Criscione-Schreiber, L. G.; Tochacek, M.; Monestier, M.; Pisetsky, D. S. Microparticles as Antigenic Targets of Antibodies to DNA and Nucleosomes in Systemic Lupus Erythematosus. *Journal of Autoimmunity.* 2011, *36* (3–4), 173–180.

(25) Birtwell, S. W.; Morgan, H. Microparticle Encoding Technologies for High-Throughput Multiplexed Suspension Assays. In *IFMBE Proceedings*. 2010, Vol. 27, pp 316–319.

(26) Wu, H.; Han, Y.; Yang, X.; Chase, G. G.; Tang, Q.; Lee, C. J.; Cao, B.; Zhe, J.; Cheng, G. A Versatile Microparticle-Based Immunoaggregation Assay for Macromolecular Biomarker Detection and Quantification. *PLoS One.* 2015, *10* (2), e0115046.

(27) Nolan, J. P.; Mandy, F. Multiplexed and Microparticle-Based Analyses? Quantitative Tools for the Large-Scale Analysis of Biological Systems. *Cytometry Part A.* 2006, *69* (5), 318–325.

(28) Greenspan, P.; Mayer, E. P.; Fowler, S. D. Nile Red: A Selective Fluorescent Stain for Intracellular Lipid Droplets. *Journal of Cell Biology.* 1985. 100 (3): 965.

(29) Gonzalez-Quintela, A.; Alende, R.; Gude, F.; Campos, J.; Rey, J.; Meijide, L. M.; Fernandez-Merino, C.; Vidal, C. Serum Levels of Immunoglobulins (IgG, IgA, IgM) in a General Adult Population and Their Relationship with Alcohol Consumption, Smoking and Common Metabolic Abnormalities. *Clinical and Experimental Immunology.* 2008, 151 (1): 42-52.

(30) Stern, E.; Vacic, A.; Rajan, N. K.; Criscione, J. M.; Park, J.; Fahmy, T. M.; Reed, M. A. Label-Free Biomarker Detection from Whole Blood. In *ICSICT-2010 - 2010 10th IEEE International Conference on Solid-State and Integrated Circuit Technology, Proceedings*. 2010, Vol. 5, 138.

(31) Junqueira, L.; Carneiro, J. Basic Histology: Text & Atlas. *Statrefcom.* 2005, 234, 265.

(32) Truskey, G. a; Yuan, F.; Katz, D. F. Transport Phenomena in Biological Systems. *Proceedings of the National Academy of Science.* 2004, 270-281.

(33) Gray, J. J. The Interaction of Proteins with Solid Surfaces. *Current Opinion in Structural Biology*. 2004. 14 (1), 110-115.

Chapter 7: Acoustically Generated Droplets in Aqueous Two-Phase Systems for 3D Microgels

Frank A. Fencl[1], Jacqueline A. De Lora[1], Aidira Dora Yajaira Macias Gonzales[1], Alireza Bandegi[2], Reza Foudazi[2], Gabriel P. Lopez[1], Andrew P. Shreve[1], Nick J. Carroll[1]

[1]Department of Chemical and Biological Engineering, Center for Biomedical Engineering University of New Mexico, Albuquerque, NM, USA

[2] Department of Chemical and Materials Engineering, New Mexico State University, Las Cruces, NM, USA

Author contributions

The primary author of this work is shared with myself, Jacqueline De Lora, and Aidira Macias. My contribution here as one of the primary authors is in the development of the acoustofluidic device and subsequent characterization of monodisperse droplet synthesis. I fabricated multiple devices and characterized the droplet synthesis for three devices across four inner phase flow rates and eleven input frequencies including one case where cells were present. Jacqueline De Lora and Aidira Macias were responsible for the recovery of cell laden hydrogels and subsequent culturing over the course of nine days. Jacqueline De Lora was also responsible for the flow cytometry analysis of the live/dead assay.

7.1 Abstract

The integration of aqueous two-phase systems (ATPS) with microfluidics for droplet-based cell culturing applications is currently limited by the need for thermodynamically stabilized phase enrichment as well as the use of simple gelation chemistries to provide a scaffolding biomaterial for long term cell culture. Here we introduce a new method of synthesizing size-controlled dextran-alginate (DEX/ALG) microgels encapsulating a suspension of cells within a polyethylene glycol (PEG) phase. Acoustic modulation of a microcapillary fluidics system is optimized and enhances the droplet formation of enriched PEG-DEX polymeric solutions. This platform provides an efficient and robust method for the templated encapsulation of cells and growth in long-term 3D suspension culture.

7.2 Introduction

Fabrication of complex, hierarchical 3D cell culture constructs within hydrogel microspheres is enabled by droplet microfluidics. An accessible acoustofluidic system comprises water-in-water emulsions, where aqueous droplets are dispersed in a surrounding immiscible water phase. These emulsions, coined aqueous two-phase systems (ATPS), make use of phase separation at specific volume fractions to form immiscible polymer solutions with distinct boundaries.[1–4] ATPS are advantageous in comparison to the use of potentially cytotoxic hydrocarbon oils as an outer phase, enabling simple gel forming chemistries in water environments.[5] Oil-water interfacial tensions are on the order of tens of millinewtons/meter (mN/m), meaning stable phase separation is favorable.[6,7] In contrast, ATPS exhibit a very low interfacial tension on the order of hundreds of micronewtons/meter (μN/m), requiring higher input energy to favor separation in microfluidic systems.[6,7] A simple implementation of ATPS uses DEX drops suspended in PEG, where droplets are formed by coflowing equilibrated fluid phases in a microfluidic channel with the addition of an applied secondary mechanical or acoustic force to break up the coflowing DEX fluidic jet stream.[8,9] This secondary force overcomes the low interfacial tension of the two aqueous phases, enhancing droplet breakup. We apply an acoustic force supplied by an amplified signal from a speaker to facilitate the breakup of the two aqueous solutions into droplets. Additionally, the cell encapsulating droplets can transition immediately into cytocompatible cell culture conditions after drop gelation.

Long term cell culture assays in microsphere gels formed using existing ATPS platforms are limited by cytotoxic gel forming chemistries, lack of diversity in gel-forming additives that recapitulate native extracellular matrix, microsphere polydispersity, and complex device configurations.[10–17] An ideal ATPS platform for cell culture should include (1) material diversity allowing for bioinspired gelling agents to be added to the polymeric droplet phase, (2) easily implemented device design using inexpensive components to promote droplet formation, and (3) cytocompatible methodology to improve control over 3D culture environment, reproducibility, and long-term cell culture. The use of crosslinked macroscale hydrogels with ATPS for cell encapsulation has been studied.[16,18,19] However, implementing a simple and cost-effective device that produces ideal hydrogel microspheres for long-term 3D cell culture has yet to be realized.

In this work, we describe a simple cytocompatible microgel fabrication technology using a fluidic device engineered to acoustically break-up an equilibrated aqueous two-phase DEX/ALG-PEG system into monodisperse droplets for long-term cell culture. Our work emphasizes the low-cost construction and simple operation of a glass capillary microfluidic device interfaced with a frequency-controlled audio loudspeaker. Cell-laden DEX/ALG drops dispersed into a PEG outer phase form within the microfluidics device and solidify in a collection solution containing calcium to form hydrogel microspheres amenable to long term culture of mammalian cells.

7.3 Materials and methods

7.3.1 Device setup, construction and coupling with loud speaker

For the construction of our microfluidic glass microcapillary device, we use a Sutter Instrument co. P-97 micropipette puller to make our 100 µm injection tip and 200 µm collection tip. The diameters are filed with fine sand paper to exact measurements. The diameter of the unpulled regions of the World Precision Instruments borosilicate glass capillaries are 1.0 / 0.58 mm OD/ID. The injection and collection capillaries are housed in a 1.5 / 1.05 mm OD/ID Harvard borosilicate glass square capillary tubes. The ends of the square capillary are covered with Probe Needles M919 plastic-steel syringe tips normal to the surface of the horizontal orientation of the glass capillaries. A square pattern is cut on either side of the syringe tips to snugly cover the capillary components of the device. The syringe tips are then covered and glued down with Deycon Epoxy to prevent leaking over a plain 25 x 75 x 1 mm cm Swiss glass slide. The capillaries are aligned using a Zeiss Axio brightfield microscope at 10X magnification. The capillary ends and syringe tips are coupled to Scientific Commodities, Inc. LDPE 1.3208 mm OD Micro Medical Tubing. This device setup can be seen in Figure 7.1.

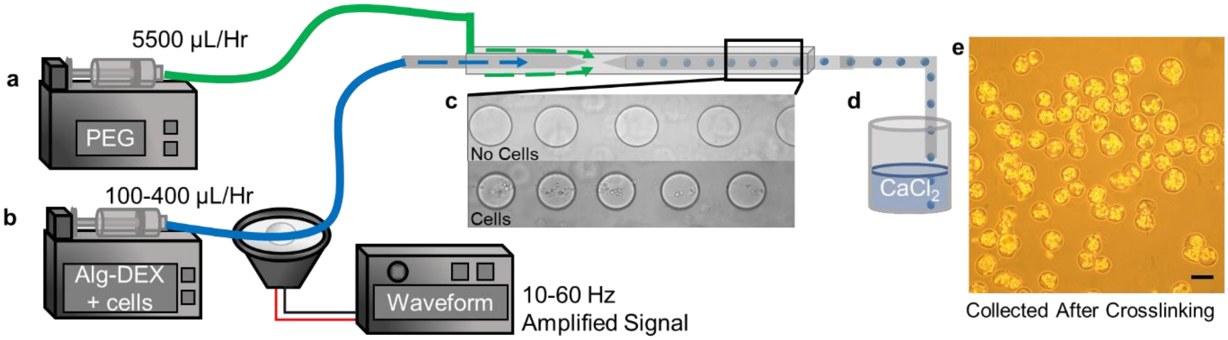

Figure 7.1. Integrating a loud speaker into the microfluidics device operation enables break-up of the otherwise low interfacial tension ATPS fluidic jet and control over the droplet size. (**a**) Syringe pumps inject the inner (alg-DEX) and outer phase (PEG) fluids into the microfluidics device. (**b**) The function generator/amplifier/loud speaker coupled to the inner phase fluidic line oscillates across a small frequency range (10-60 Hz), modulating droplet formation within the device which is demonstrated in (**c**), with and without cells. (**d**)**,** The droplets are collected into a calcium bath, which crosslinks the alginate in the inner phase, and transferred to suspension culture for up to 9 days where (**e**)**,** cell growth is observed. Scale bar = 100 μm.

The microfluidic device is placed on the microscope stage for droplet synthesis. The injection tubing, coupled to the injection capillary for inner phase infusion, is taped directly to an uncovered loudspeaker surface (Figure 7.1 b). The loudspeaker is connected to a Fosi Audio 50W 4 ohms, 20 Hz - 20 kHz, 0.04% THD) Stereo Audio Amplifier Mini Hi-Fi Professional Amp for Home Speakers approximately 10 cm from the microfluidic device. The frequency input signal’s source is an Agilent Technologies 33250A Function/Arbitrary Waveform Generator connected directly into the amplifier. The input peak-to-peak voltage is set to 10 V from the function generator for all the experiments. We vary the frequency in 5 Hz intervals from 10 to 60 Hz to generate the matrices. The injection tubing is connected to a Becton Dickson 10 mL plastic syringe and Harvard Apparatus, PHD 200 Infuse/Withdraw, CAT#: 70-2001, FREQ(HZ) 50/60 Syringe Pump approximately 74 cm from the microfluidic device.

7.3.2 ATPS solutions and cell laden hydrogels

The injection syringe contains the ~107 cells/mL of EMT6 mouse mammary carcinoma cells in 5% enriched 550 kDa Dextran 25mM HEPES, 150mM NaCl aqueous solution from Sigma Aldrich with 0.5% weight per volume (w/v) alginate from Sigma Aldrich at pH 7.4. The tubing connected to the outer phase infusion syringe tip is connected to a Becton Dickson 60mL plastic syringe on another Harvard Apparatus Syringe Pump approximately 80 cm from the microfluidic device. The 60mL syringe contains the outer phase solution of 17% enriched 8 kDa Poly(ethylene glycol) 25mM HEPES, 150mM NaCl aqueous solution at pH 7.4 from Sigma Aldrich. The second syringe tip distal to the injection side is coupled with the same Micro Medical Tubing and connected to a Becton Dickson 10 mL plastic syringe for excess outer phase waste approximately 20 cm from the device. The collection capillary is interfaced with a short 2.38 mm OD Tygon tubing to another 1.0 / 0.58 mm OD/ID ~90^{o} bent World Precision Instruments borosilicate glass capillary that is submerged in a 20 mL Scintillation vial half-filled with a solution of 1M CaCl2, 150 mM NaCl, 25 mM HEPES, and pH 7.4 crosslinking solution.

7.3.3 Aqueous polymer phase separation (polymer phase enrichment)

The Dextran (DEX) and Poly(ethylene glycol) (PEG) solutions are enriched prior to hydrogel synthesis. 5% w/w of a 50mL aqueous solution of 550 kDa DEX in 25mM HEPES buffer, 150 mM NaCl at pH of 7.4 is dissolved thoroughly. A 17% w/w

50mL aqueous solution of 8 kDa (PEG) 25mM HEPES buffer, 150mM NaCl at pH of 7.4 is dissolved as well. The two solutions are added to a 125 mL glass separatory funnel and mixed thoroughly. The two aqueous polymer phases are given ~48-hours to separate into distinct phases. The higher density DEX phase separates into the bottom of the funnel and the lower density PEG remains as the top phase. A Kruss, DR6200-TF Refractometer was used to verify the bottom phase as DEX. The DEX phase is confirmed as the bottom partitioned volume of the enriched ATPS by refractive index measurements (Figure 7.2). Each data point's respective standard deviation error bar is smaller than the diameter of the plotted points. Each phase is then collected into separate vials. 0.5% w/w alginate is added to the collected DEX and stirred for 24 hours for complete mixing. The DEX-alginate and PEG solutions are then both filtered using a 0.2 µm Nalgene bottle top filter to sterilize for cell culture.

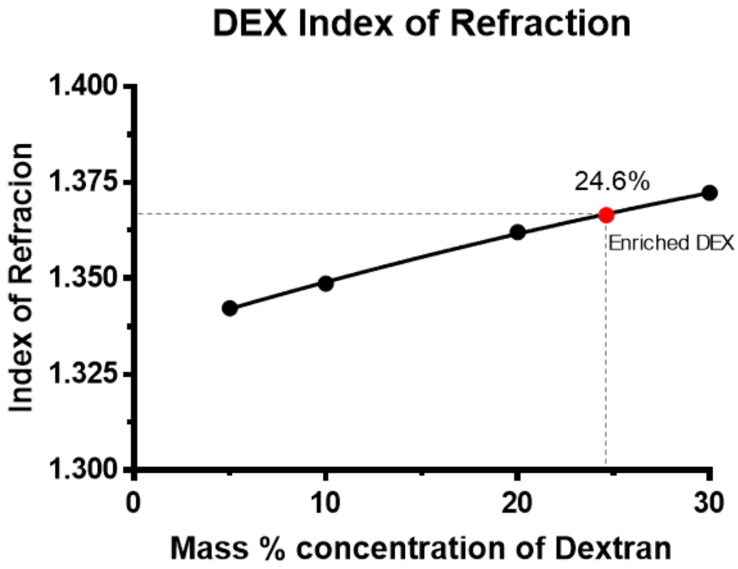

Figure 7.2. DEX bottom phase index of refraction. Four pure dextran weight percent solutions were mixed in buffer solution, used for the cell encapsulation experiments, consisting of millipore filtered water, 150 mM NaCl, and 25 mM Hepes pH controlled at 7.4 (polymer buffer). The solutions were prepared at 5% w/v, 10% w/v, 20% w/v, and 30% w/v of DEX in polymer buffer (black points). The solutions were measured for their index of refraction values 5 times each with a standard deviation smaller than the area of the points on the graph. A 17% PEG and 5% DEX in aqueous polymer buffer solution was enriched as described previously; the bottom phase was collected for interrogation. The value of the unknown bottom phase was plotted against the known indexes of refraction and interpolated to the fit polynomial curve to determine the mass % of 24.6 (red).

7.3.4 Three-dimensional hydrogel cell culturing

EMT6 mouse mammary carcinoma cells are maintained using standard sterile cell culture conditions (37 ^{o}C, 5%CO_2) in 150 mm tissue culture treated polystyrene dishes (Corning) with 20 mL of Minimal Essential Media supplemented with 10% Fetal Bovine Serum and 1% Penicillin/Streptomycin (Sigma-Aldrich) to grow up for encapsulation. In general, if desired cell/droplet occupancy is 10 cells/100 µm DIA droplet then 2x107 cells/mL is required for the encapsulation protocol. This concentration is easily adjusted by changing the initial cell encapsulation concentration. Cells at ~80% confluence in 150 mm dishes (depending on the desired final concentration) are washed with 3 mL of 0.5% Trypsin and then incubated in 5 mL of 0.5% Trypsin (Sigma-Aldrich) for up to 30 minutes to digest and release attached cells. The cells are then washed off the dish with gentle pipetting by adding 5 mL of media to the 5 mL of trypsin and cells. This 10 mL cell suspension is transferred into a 50 mL centrifuge tube (and combined with cells recovered from additional 150 mm dishes if applicable), a sample is taken for cell counting using a Z Series Coulter Counter and centrifuged at 1500 RPM for 10 minutes to pellet.

The cell concentration to be used is determined, the cell pellet is resuspended into 20 mL physiological buffer (25 mM HEPES, 150 mM NaCl, pH 7.4), and the volume corresponding to the desired final cell concentration is transferred to a fresh 50 mL centrifuge tube. This adjusted cell suspension is then centrifuged at 1500 RPM for 10 mins to wash and pellet. The physiological buffer supernatant is then aspirated, and the cell pellet is resuspended into 500 µL of sterile filtered DEX-alginate by gentle pipetting using a 1000 µL pipette. The 500 µL of DEX-alginate cell suspension is drawn up into an 18G needle/10 mL syringe (BD) and then added dropwise to 2.5 mL of DEX-alginate in a 50 mL centrifuge tube while vortexing. The 3 mL cell suspension is then passed through a 40 µm cell strainer test-tube filter insert (BD Falcon) into a fresh 50 mL centrifuge tube to produce the final single cell suspension in DEX-alginate. A sample is taken from this solution to count the final cell concentration as there is some cell loss during the protocol due to the highly-viscous nature of the DEX-alginate and the filtering out of any cell clumps. This dropwise-vortex mixing, and filtering of the DEX-alginate and cells guarantees a single cell suspension which is paramount to avoiding clogs in the microfluidics device. The cell suspension is loaded into a 10 mL syringe for droplet synthesis in the microfluidics system.

Over the course of droplet synthesis (about once/hour), crosslinked droplets are removed from the setup and allowed to settle in the 1 M $CaCl_2$ buffer so that the excess Ca^{2+} may be removed and the cell encapsulating droplets can be transferred by gentle pipetting into a temperature equilibrated 125 mL spinner flask bioreactor (Corning) with 125 mL of complete media adjusted to pH 7.4 with 25 mM HEPES. For the t0 initial time point, a 20 µL sample of droplets is pipetted onto a microscope slide (VWR) and placed onto a brightfield microscope for imaging using a Nikon camera and SPOT Basic software. Once the total cell encapsulating droplet population has been transferred into the spinner flask bioreactor, the head space is backfilled with 5% CO_2 and placed onto a slow stir plate in a warm room maintained at 37 ^{o}C for the duration of the time course (9 days). At days 3, 5, 7, and 9 samples are taken from the culture for imaging as described above and the culture media is changed. The spinner flask bioreactor is removed from the stir plate, allowing the droplets to settle to the bottom of the flask. Once settled, the media is aspirated being careful to leave about 20 mL at the bottom to not aspirate droplets and then refiled to a final volume of 125 mL with temperature equilibrated complete media and backfilled as before.

On day 9, the total droplet population is collected, and the cells are recovered as well as counted for comparison to the initial cell concentration. To collect the droplet population, the droplets are allowed to settle, and the media is aspirated until 20 mL of media and droplets remain in the spinner flask. The 20 mL of droplets and media is pipetted into a 50 mL centrifuge tube and the droplets can settle once more (~10 minutes). The remaining media is carefully aspirated and 20 mL of a droplet dissolving buffer (0.5% trypsin, 50 mM sodium citrate, 25 mM HEPES, 150 mM NaCl pH 7.4) is added to the droplets in the 50 mL tube. The tube is incubated at 37 ^{o}C for 30 minutes with vortexing every 5 minutes to encourage dissociation of cell aggregates. The recovered cells in dissolving buffer are then centrifuged at 1500 RPM for 10 minutes, resuspended into 1 mL of physiological buffer and counted using the Coulter Counter.

7.3.5 Flow cytometry analysis

Upon completion of droplet synthesis, we assay the cells from the remaining cell suspension in DEX-alginate for apoptosis by annexin V and necrosis by propidium iodide (also known as LIVE/DEAD). The DEX-alginate cell suspension is compared to LIVE and DEAD control populations. The LIVE cells are processed with trypsinization into a single cell suspension and remain in complete media on ice during the experiment while the DEAD control cells are treated by suspension in 50% ethanol for 60 minutes at 37 ^{o}C and 5% CO_2 in the incubator. Once the DEX-alginate cell suspension has been in ambient conditions for the duration of droplet generation (~2 hours), it is transferred to a 15 mL centrifuge tube and diluted by the addition of physiological buffer to dilute the viscosity of the solution. The suspension is centrifuged at 3000 RPM for 10 minutes. In this first wash, the cells form a band towards the bottom of the test tube but have not yet been fully pelleted so ~5 mL of the diluted DEX-alginate is removed by aspiration and 5 mL of physiological buffer is added and vortexed. The tube is centrifuged at 3000 RPM for 10 minutes. This wash/centrifugation protocol is repeated once more to pellet the cells at the bottom of the tube and remove as much residual DEX-alginate solution as possible. The DEX-alginate-buffer supernatant is removed, and the cells are washed in 10 mL of physiological buffer followed by aliquoting into 4, 15 mL test tubes and centrifugation at 2000 RPM for 10 minutes. The staining protocol is then followed as described in

Alexa Fluor 488 annexin V/Dead cell apoptosis Kit with Alexa Fluor 488□ annexin V and PI for flow cytometry from Invitrogen. The samples are analyzed (100,000 events per group) using an Attune NxT flow cytometer.

7.4 Results and discussion

7.4.1 System characterization and size distributions by varying applied frequency and flow rates

Droplet size variation by speaker frequency modulation is observed in our preliminary work where enriched 17% w/w 8 kDa PEG (outer phase) is co-flowed with enriched 5% w/w 550 kDa DEX (droplet phase) and monodispersed DEX drops form. These observations motivate the idea to use this method as a mode of generating monodispersed hydrogels for cell culturing by incorporating ALG as a simple crosslinkable matrix for cell encapsulation. Varying the weight percent concentrations of ALG drastically changes the viscosity of the already highly viscous DEX droplet phase. High concentrations of ALG inhibit the breakup of the inner phase even with incorporation of an amplified signal to the speaker. We scale the amount of ALG to 0.5% w/v in the DEX droplet phase, enabling droplet generation after increasing the amplitude of the applied acoustic force generated from the speaker. To operate the device, the inner phase (composed of 5% w/v 550 kDa dextran, 0.5% w/v sodium alginate and a suspension of EMT6 mouse mammary carcinoma cells) is directly attached to a speaker enabling acoustic oscillation of the coflowing fluidic jet to modulate droplet formation. We investigated a combinatorial range of input frequencies (10-60 Hz) and inner phase flow rates (100-400 µL/Hr) to manipulate the size of the hydrogel droplets in real time (Figure 7.3 a).

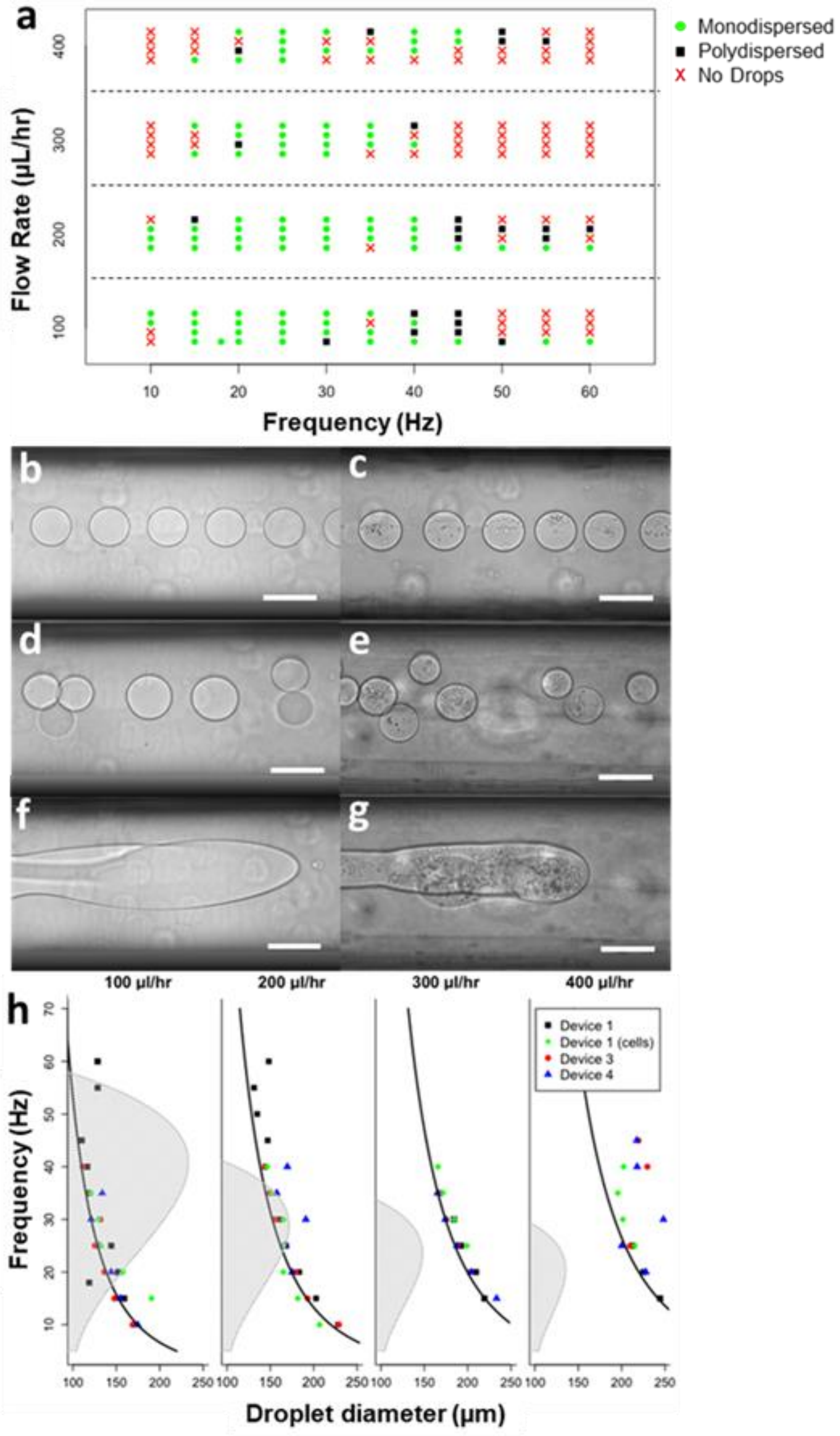
a
Flow Rate (µL/hr)
100
200
300
400
Frequency (Hz)
10
20
30
40
50
60
● Monodispersed
■ Polydispersed
X No Drops
b
c
d
e
f
g
100 µl/hr
200 µl/hr
300 µl/hr
400 µl/hr
h
Frequency (Hz)
10
20
30
40
50
60
70
Droplet diameter (µm)
100
150
200
250
Device 1
Device 1 (cells)
Device 3
Device 4

Figure 7.3. Characterizing the microfluidics system across a range of flow rate/frequency combinations both with and without cells enables robust, controllable, and reproducible droplet generation. (a) Droplets synthesized are visually characterized as monodisperse, poly disperse or no regular drop formation. Each set of points represents four experimental runs varying applied frequency and flow rates using Device 1 (bottom point), Device 1 with cells (2nd from bottom), Device 2 (3rd from bottom), and Device 3 (top point). Representative images of characterizing samples without (b, d, f) and with (c, e, g) cells and by their size distribution (h) ; monodispersed (b, c), polydisperesed (d, e), or no droplet generation observed (f, g). Each experiment used a constant outer phase flow rate of 5500 ul/hr and Function Generator input voltage of 10 Vp-p into the amplifier and each image was taken 5.5 cm downstream from the injection nozzle. (h) Droplet size distribution is plotted against a theoretical mass conservation curve (black line) as a function of applied frequency and flow rates across 3 different microfluidic devices. Growth rate for monodisperse droplet formation determined by a variant of Plateau-Rayleigh instability is plotted as an overlay (grey curve). Scale bars = 200 µm.

Droplet formation is characterized by microscopy across three individual devices without a cell suspension in the inner phase and with cells in one repeat instance with $n \geq 2$ (Figure 7.3 b-g). We observed monodisperse as well as polydisperse formation of droplets across a size range of 100 to 250 µm diameters and in some cases no droplet formation for inner phase solution with and without cells (Figure 7.3 a-g). Resultant monodisperse droplet sizes, as a function of frequency, agree with a theoretical mass conservation model that predicts diameter at given inner phase flow rates (Figure 7.3 h, data points and black line). Interestingly, the 400 µL/Hr flow rate demonstrates points of deviation from the theoretical droplet formation regime likely due to growth of spontaneous perturbations and not as a result of the acoustic driving frequency as is evident in the lower inner phase flow rates (100, 200, and 300 µL/Hr).[20–22]

The droplet breakup regime for such an ATPS is understood by a variant of Plateau-Rayleigh instability growth rate (Figure 7.3 h grey curve overlay), studied by Adjari et al.[23] Their model predicts droplet formation as a result of the growth rate for specific frequencies for a spontaneous (non-driven) system. However, we observed a stable fluidic jet in the absence of acoustically induced perturbations. This observed discrepancy of the Plateau-Rayleigh instability between non-driven and spontaneous droplet formation has been documented before by Kreutzer et al. for DEX/PEG ATPS.[5,24] Spontaneous droplet systems for DEX/PEG ATPS have been observed at weak hydrostatic pressures by Tsai et al. providing a counterpoint to our observations.[25]

Although certain frequency and flow rate combinations do not produce drops or produce polydisperse droplet populations, there are driving parameters that reproducibly yield monodisperse droplet populations (Figure 7.3). Intuitively, we observe a decrease in droplet size with increasing acoustic frequency and decreased flow rates. Collecting the flowing droplets into a $CaCl_2$ bath enables rapid crosslinking of the DEX/ALG gels which results in hydrogel droplets with an almost perfect aspect ratio and sphericity. After characterizing our improved technique for using an ATPS system with a gelling agent to create droplets in our acoustofluidic device, we investigated the viability for 3D cell culture applications.

7.4.2 Hydrogel culturing viability

We grow the EMT6 mouse mammary carcinoma cell line, which is well characterized to grow in conventional tumor spheroid models[27], in standard culture conditions and use a protocol developed for preparing a single cell suspension in the

DEX/ALG droplet phase. Details on cell culturing can be seen in the Supplementary Information. After adding the cells to the DEX/ALG phase, we operate the system at various inner phase flow rate and frequency combinations to determine if the addition of the cells affects droplet generation. The resultant matrix of droplet formation with cells contains fewer stable droplet generating regimes in comparison to the inner phase solutions without cells incorporated (Figure 7.2 a). This observation motivated us to investigate the rheological properties of the fluid components both with and without cells. Further details can be seen in Supplementary Information. From the rheology measurements, we conclude that the presence of cells in the droplet phase at both low and high cell concentrations does not substantially change the viscosity however the droplet generation matrix with cells is still limited. We hypothesize that this may be caused by observed cell aggregation within the inner phase solution over the duration of a droplet synthesis experiment. The aggregation of cells over time is a natural phenomenon that has been exploited for conventional tumor spheroid formation but in our case, influences the injection of the inner phase solution out of the glass microcapillary and therefore changes the dynamics effecting the droplet generation.[28]

A well-known challenge with the interface of microfluidic droplet generation and cell culture is the necessity for low volumetric flow rates, where cells in a biomaterial suspension may be out of ideal culture conditions for up to hours at a time. To demonstrate that our new method of 3D cell encapsulation with an ATPS system and the time to synthesize enough droplets for relevant biological assays is still a biocompatible approach, we measured the fraction of live to necrotic cells recovered from the inner phase directly after droplet generation using an adapted Annexin V/Propidium iodide flow cytometric assay (Figure 7.4 a). Quantitatively, there is no statistically significant difference between the live control group and our experimental (cells in DEX/ALG) group for necrosis. There was a qualitative increase in the necrosis of the cells in the DEX/ALG however this is likely due to the rigorous dilution, washing, and centrifugation protocol necessary to recover the cell population from the DEX/ALG pre-gel for assay and not due to exposure to the biomaterial, exposure to shearing or acoustic forces, and the time for device operation. Furthermore, the viability of these microgels proved exceptional after nine days of suspension culture in spinner flask bioreactors. We demonstrated the robustness of the system by encapsulating EMT6 cells on 3 separate occasions using different cell concentrations, imaged the proliferation of each culture immediately after encapsulation and at 3, 5, 7 and 9 days (Figure 7.4 b). Qualitatively, it appears that there is a lag phase in the proliferation rate of the cells from initial encapsulation to day 3 which is likely caused by a low cell encapsulation concentration (~10 cells/droplet) and the cells being isolated from one another. Once cell-cell contact is established, the growth rate becomes more exponential and cellular aggregation as in tumor spheroid formation is observed.

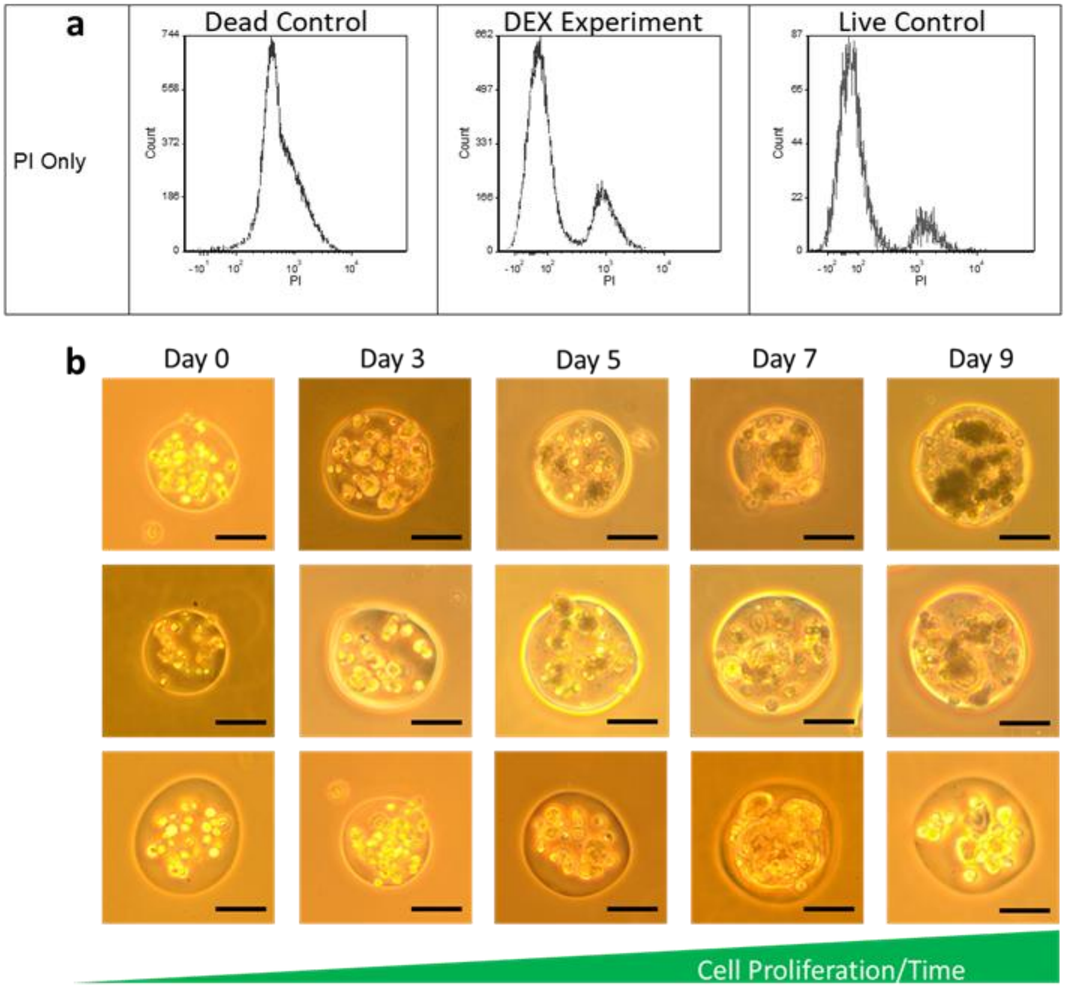

Figure 7.4. Encapsulating cells in DEX-ALG droplets produces a reliable platform for cell proliferation and eventual formation into multicellular tumor spheroids. (a) The results from an apoptosis/ necrosis (annexin V/propidium iodide) flow cytometric assay indicate that the polymer solutions and the method to encapsulate the cells are biocompatible and the slight shift in necrosis is because of post processing affects to centrifuge cells out of the DEX-alginate solution. EMT6 mouse mammary carcinoma cells are encapsulated at different initial concentrations (rows in b) and observed to proliferate up to the end of our culture time course of 9 days (scale bars 50 µm).

7.5 Conclusions

Acoustically assisting water-in-water droplet generation for 3D cell culturing hydrogels provides a low cost and reproducible method to grow and study cell systems across multiple applications. This technology provides a robust method to generate 3D hydrogels for cell culture and has the potential to be used alongside drug discovery platforms or for 3D printing applications. Our initial work proves to be a platform with feasibility for scaling up by incorporating higher volume microfluidics with an acoustic actuator to yield larger, monodispersed populations of 3D cell encapsulating hydrogels. Future application for this method will be applied to encapsulating biological components including trapping giant unilamellar vesicles which have a notoriously short lifespan in vitro. Finally, using this gentle method to encapsulate biological components may prove to aid in study for future cancer therapeutics or other drug discoveries.

7.6 Acknowledgements

We’d like to acknowledge prof. Steven W. Graves for his involvement in the speaker to amplifier set up.

7.7 References

(1) Grilo, A. L.; Aires-Barros, M. R.; Azevedo, A. M. Partitioning in Aqueous Two-Phase Systems: Fundamentals, Applications and Trends Partitioning in Aqueous Two-Phase Systems: Fundamentals, Applications and Trends. *Separation and Purification Reviews.* 2016, *45* (45), 68–80.

(2) MacE, C. R.; Akbulut, O.; Kumar, A. A.; Shapiro, N. D.; Derda, R.; Patton, M. R.; Whitesides, G. M. Aqueous Multiphase Systems of Polymers and Surfactants Provide Self-Assembling Step-Gradients in Density. *Journal of the American Chemical Society.* 2012, *134* (22), 9094–9097.

(3) Iqbal, M.; Tao, Y.; Xie, S.; Zhu, Y.; Chen, D.; Wang, X.; Huang, L.; Peng, D.;

Sattar, A.; Shabbir, M. A. B.; et al. Aqueous Two-Phase System (ATPS): An Overview and Advances in Its Applications. *Biological Procedures Online*. 2016, 1–18.

(4) Johansson, G. , Hartman, A. and Albertsson, P. Partition of Proteins in Two-Phase Systems Containing Charged Poly(ethylene glycol). *European Journal of Biochemistry.* 1973, 33: 379-386.

(5) Ziemecka, I.; van Steijn, V.; Koper, G. J. M.; Rosso, M.; Brizard, A. M.; van Esch, J. H.; Kreutzer, M. T. Monodisperse Hydrogel Microspheres by Forced Droplet Formation in Aqueous Two-Phase Systems. *Lab on a Chip.* 2011, *11* (4), 620–624.

(6) Jian, C.; Poopari, M. R.; Liu, Q.; Zerpa, N.; Zeng, H.; Tang, T. Reduction of Water/Oil Interfacial Tension by Model Asphaltenes: The Governing Role of Surface Concentration. *Journal of Physical Chemistry B.* 2016, *120* (25), 5646–5654.

(7) Peters, F.; Arabali, D. Interfacial Tension between Oil and Water Measured with a Modified Contour Method. *Colloids Surfaces A: Physicochemical and Engineering Aspects.* 2013, *426*, 1–5.

(8) Ziemecka, I.; van Steijn, V.; Koper, G. J. M.; Rosso, M.; Brizard, A. M.; van Esch, J. H.; Kreutzer, M. T. Monodisperse Hydrogel Microspheres by Forced Droplet Formation in Aqueous Two-Phase Systems. *Lab on a Chip.* 2011, *11* (4), 620–624.

(9) Song, Y.; Shum, H. C. Monodisperse w/w/w Double Emulsion Induced by Phase Separation. *Langmuir.* 2012, *28* (33), 12054–12059.

(10) Song, Y.; Chan, Y. K.; Ma, Q.; Liu, Z.; Shum, H. C. All-Aqueous Electrosprayed Emulsion for Templated Fabrication of Cytocompatible Microcapsules. *ACS Applied Materials and Interfaces.* 2015, 7 (25), 13925–13933.

(11) Liu, H.-T.; Wang, H.; Wei, W.-B.; Liu, H.; Jiang, L.; Qin, J.-H. A Microfluidic Strategy for Controllable Generation of Water-in-Water Droplets as Biocompatible Microcarriers. *Small.* 2018, *14* (36), 1801095.

(12) Fang, Y.; Frampton, J. P.; Raghavan, S.; Sabahi-Kaviani, R.; Luker, G.; Deng, C. X.; Takayama, S. Rapid Generation of Multiplexed Cell Cocultures Using Acoustic Droplet Ejection Followed by Aqueous Two-Phase Exclusion Patterning. *Tissue Engineering Part C: Methods.* 2012, *18* (9), 647–657.

(13) Mellott, M. B.; Searcy, K.; Pishko, M. V. Release of Protein from Highly Cross-Linked Hydrogels of Poly(Ethylene Glycol) Diacrylate Fabricated by UV Polymerization. *Biomaterials.* 2001. 22 (9), 929-941

(14) Lopérgolo, L. C.; Lugão, A. B.; Catalani, L. H. Direct UV Photocrosslinking of

Poly(N-Vinyl-2-Pyrrolidone) (PVP) to Produce Hydrogels. *Polymer (Guildf).* 2003. 44 (20), 6217-6222

(15) Mironi-Harpaz, I.; Wang, D. Y.; Venkatraman, S.; Seliktar, D. Photopolymerization of Cell-Encapsulating Hydrogels: Crosslinking Efficiency versus Cytotoxicity. *Acta Biomaterials.* 2012, 8 (5), 1838-1848

(16) Sung, H. W.; Huang, D. M.; Chang, W. H.; Huang, R. N.; Hsu, J. C. Evaluation of Gelatin Hydrogel Crosslinked with Various Crosslinking Agents as Bioadhesives: In Vitro Study. *Journal of Biomedical Materials Research.* 1999, 46 (4), 520-530

(17) Sahiner, N.; Singh, M. In Situ Micro/Nano-Hydrogel Synthesis from Acrylamide Derivates with Lecithin Organogel System. *Polymer (Guildf).* 2007, 48 (10), 2827-2834

(18) Fichman, G.; Gazit, E. Self-Assembly of Short Peptides to Form Hydrogels: Design of Building Blocks, Physical Properties and Technological Applications. *Acta Biomaterials*. 2014, 10 (4), 1671-1682

(19) Andersen, T.; Auk-Emblem, P.; Dornish, M. 3D Cell Culture in Alginate Hydrogels. *Microarrays.* 2015, *4* (2), 133–161.

(20) Sugiura, S.; Nakajima, M.; Kumazawa, N.; Iwamoto, S.; Seki, M. Characterization of Spontaneous Transformation-Based Droplet Formation during Microchannel Emulsification. *Journal of Physical Chemistry B.* 2002, 106 (36), 9405–9409.

(21) Sugiura, S.; Nakajima, M.; Iwamoto, S.; Seki, M. Interfacial Tension Driven Monodispersed Droplet Formation from Microfabricated Channel Array. *Langmuir.* 2001, 17 (18), 5562–5566.

(22) Sauret, A.; Shum, H. C. Beating the Jetting Regime. *International Journal of Nonlinear Sciences and Numerical Simulation.* 2012, 13 (5), 351–362.

(23) Guillot, P.; Colin, A.; Ajdari, A. Stability of a Jet in Confined Pressure-Driven Biphasic Flows at Low Reynolds Number in Various Geometries. *Physics Review E - Statistical Nonlinear, Soft Matter Physics.* 2008, E78, 016307.

(24) Geschiere, S. D.; Ziemecka, I.; Van Steijn, V.; Koper, G. J. M.; Esch, J. H. va.; Kreutzer, M. T. Slow Growth of the Rayleigh-Plateau Instability in Aqueous Two Phase Systems. *Biomicrofluidics.* 2012, 6 (2), 022007.

(25) Moon, B. U.; Abbasi, N.; Jones, S. G.; Hwang, D. K.; Tsai, S. S. H. Water-in-Water Droplets by Passive Microfluidic Flow Focusing. *Analytical Chemistry.* 2016, 88 (7), pp 3982–3989.

(26) Eggers, J.; Villermaux, E. Physics of Liquid Jets. *Reports on Progress in Physics.* 2008, *71* (3), 036601.

(27) Freyer, J. P.; Sutherland, R. M. Proliferative and Clonogenic Heterogeneity of Cells from EMT6/Ro Multicellular Spheroids Induced by the Glucose and Oxygen Supply. *Cancer Research.* 1986, *46* (7), 3513–3520.

(28) Kelm, J. M.; Timmins, N. E.; Brown, C. J.; Fussenegger, M.; Nielsen, L. K. Method for Generation of Homogeneous Multicellular Tumor Spheroids Applicable to a Wide Variety of Cell Types. *Biotechnology Bioengineering.* 2003, *83* (2), 173–180.

Chapter 8: Conclusions and Future Directions

The motivation for this dissertation is to provide basis for the integration of acoustic focusing and separation technologies for various platforms in the biomedical field. Each chapter has contributed to the investigation of using acoustics in the fields of flow cytometry, high-throughput systems, point-of-care testing platforms, and in the synthesis of 3D hydrogels for cell culturing. Improvements toward the development of flow chambers for acoustic flow cytometry have been illustrated and reduced to practice in practical and analytical applications. We have also demonstrated the ability to develop point of care handheld devices with engineered microparticles that trap media and separate from positive contrast cells in various dilute blood concentrations. Finally, we have illustrated the ability to synthesize monodispersed 3D hydrogels for cell culturing coupling an acoustic actuator with the inner phase of an aqueous two-phase system.

Further work can be done to develop the optically clear acoustic flow chambers. The methods presented to construct the device require cleanroom access and hazardous chemicals. A method to more efficiently construct silicon-core glass bonded devices without the need of a cleanroom would be beneficial to the field of acoustofluidics. 3D printers are still a new emerging field and may soon be able to construct these flow chambers with a glass or metallic molding material. Once this is taken to practice, it will likely remove the need to use photolithography, DRIE, and chemical etchants. Even though silicon has proven to be optimal for acoustofluidic devices, using metal or glass would perform adequately and could remove the need for cleanroom procedures for device fabrication of this kind. In addition to fabrication methods, this work can be used to run multiple samples in parallel etched channels within the same device. For example, four wide channels can be interrogated in parallel while sampling four different test volumes.

The highly parallel acoustic flow cytometer is an example of growth in the field of state-of-the-art flow cytometry. Being able to run high volume samples and detect specific events will prove ideal for assays where rare event detection is critical. In general, this platform will continue improving volumetric and analytical rates. The work presented focuses on assessing viability against known quality control particles with given fluorescence intensities and sizes. Further work will focus in biological assays where individual events, like circulating tumor cells, are of interest from the assay. Additionally, we seek to further increase the processing and image analysis for devices with channel dimensions greater than 2 mm wide.

Regarding the analysis of acoustic focusing at air-water interfaces, the work will benefit from further studies where incorporating multiple parallel streams and assessing the focusing recovery across at each stream will be analyzed. Additional analysis in varying applied voltage for higher flow rates will also aid in the understanding of acoustic focusing at the air-water interface. This work will continue to increase in interest for high throughput systems that integrate the highly parallel acoustic flow cytometry technology with an automated sampling system.

Future work on the lab in a syringe device will incorporate an integrated detection system for trapped analytes. The device is currently limited by having a post processing analysis step required to observe a fluorescent signal. In addition to incorporating a fluorescence signal sensor, our device will have the dead volume regions removed so that it can be incorporated into a more pipette-like device. Further work also needs to be done to assess the lower limit of affinity capture and signal detection for various concentrations of target antibody.

We can also further the development of our ATPS droplets for 3D cell culture technology. The device and materials described for this portion of our work could have iterations done on two fronts. First the capillary device constructed has a collection capillary that may hinder the droplet breakup. We can potentially remove the collection capillary to improve breakup of the inner phase fluidic jet. Second, we can also develop alternative materials to facilitate crosslinking of the hydrogels. Our group is currently working on Zinc crosslinkable elastin-like proteins that can be used as a substitute for alginate. A protein matrix may provide a more native like structure which can increase the proliferation of target cell cultures.

Acoustic technologies are still a relatively new and growing field. Integration into varying platforms holds promise in growing the efficiency of diagnostic tools such as the topics described herein. There are still more areas of research that need to be investigated to fully assess the viability of acoustic technology in the biomedical field. The research illustrated here illustrates a better understanding of the versatility of acoustic technologies ranging from media separations and assays to droplet generation in soft materials sciences. some of the immediate benefits of acoustic integration have already been identified i.e. faster throughput and gentle biological media interrogation. Given these benefits, Acoustic technologies are proving to be impactful in the field of biomedical research.

Appendices

Appendix A: Additional Information for Chapter 3

A.1 Positive resist soft lithography process

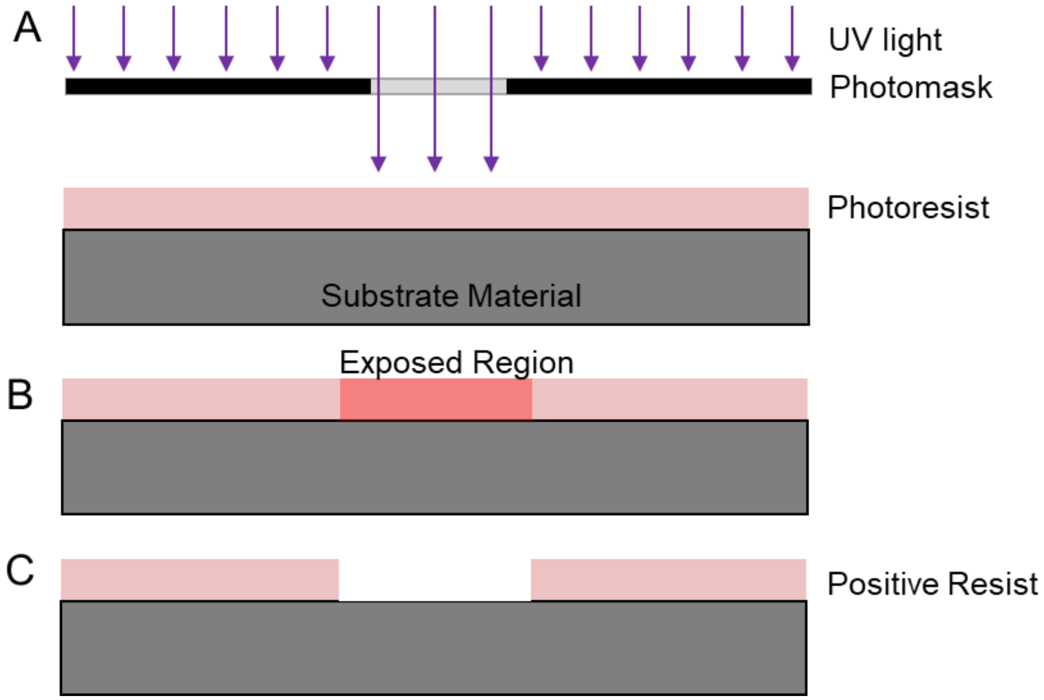

Figure A.1. Soft lithography steps using positive photoresist. (A) photomask transmitting high energy UV light after photoresist on silicon wafer baking. (B) Exposed region has polymer bonds scissioned by high energy uv light. (C) Device is developed using the specified developer solvent (AZ 400 K series) of the positive resist leaving only photoresist of unexposed regions.

A.2 Additional fabricated devices

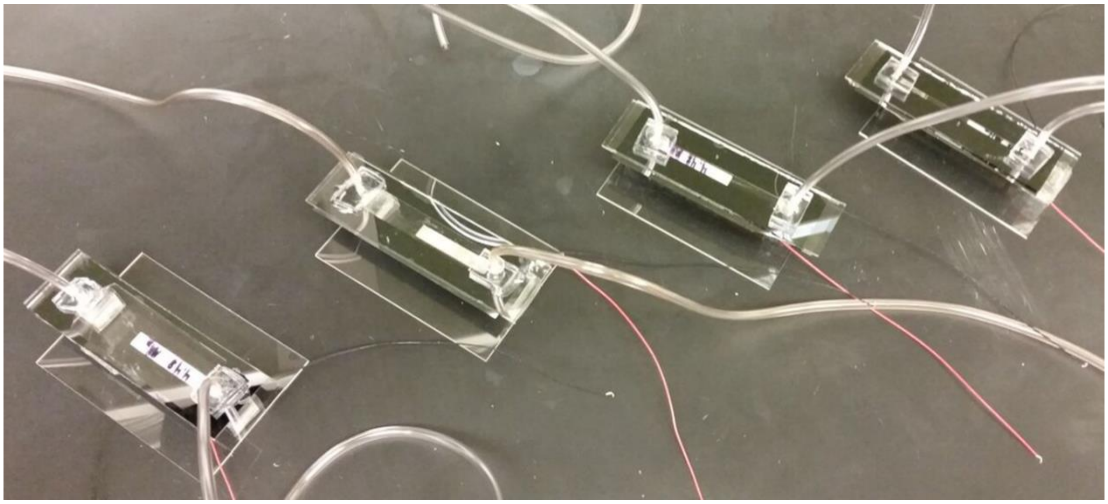

Figure A.2. Fabricated devices to completion. From left to right etched channel width dimension by device; 20 mm, 10 mm, 5 mm, 2 mm. Each device has PZT and inlet/outlet tubing attached. Tubing is interfaced through biopsy punched PDMS pad that is plasma cleaner bonded to glass slide device surface.

A.3 Thermocouple temperature measurements

To examine whether the optically transparent devices experienced a reduction in heating from exposure to an incident laser beam, we measured the surface temperature of an optically clear device (Device1) and compared to the response of an opaque-bottom channel device (Device 2). A 6802 II Durable Precision Dual Channel Digital Thermometer with 2 K-Type Thermocouple Sensor with two input leads was used to measure the temperature changes. The initial temperature of each device was recorded prior to switching on the laser (T0), and then temperatures were recorded at several time points over 15-minute intervals for a 60 min period, and then recorded at 30 min intervals after that, for a total time of 3 hours. The ambient room temperature was first measured to be 21.6 ^{o}C for Device 1 and 21.8 ^{o}C for Device 2 (two leads, three measurements averaged per time point). After the room temperature was recorded, the leads were taped to the back-side of the silicon surface on the opaque bottom flow chamber, precisely behind where the laser was being transmitted. The laser is a 150 mW 488 nm laser (MiniWhisperIT, Pavillion Integration Corporation, San Jose, CA) set up in a custom system as described previously in Chapter 4. The beam was focused into narrow wide profile using the previously described optics into a ~2.3 mm wide by ~ 10 – 20 µm height(1). Device 1 experienced 0.2 ^{o}C increase in temperature after 15 min, moreover, the temperature was relatively stable for the entire duration of the experiment (3 hrs.) for both devices, with minimal increase overall, despite exposure to the incident laser beam for the entire experiment. The changes in temperature seemingly did not measurably fluctuate above room temperature (at 15 minutes and then 60 minutes but went back to ambient room temperature for the remainder of the experiments as seen in Table S2. The final temperatures of 20.6 and 21.1 confirmed to be that of room temperature (21.1 and 21.3 respectively) measured after the experiment.

A.4 Device surface temperature measurements during laser transmittance

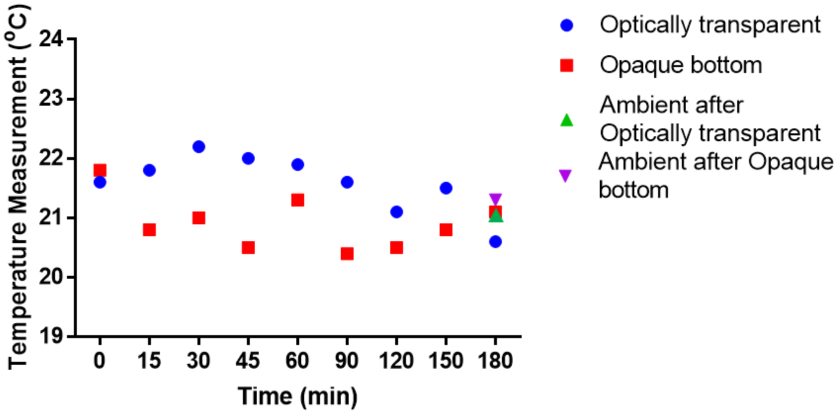

Time (minutes)	Device 1 temp (°C)	Device 2 temp (°C)
T0	21.6	21.8
15	21.8	20.8
30	22.2	21.0
45	22.0	20.5
60	21.9	21.3
90	21.6	20.4
120	21.1	20.5
150	21.5	20.8
180	20.6	21.1
Ambient temp	21.1	21.3

Figure A.4. Graph and table of opaque and clear device temperatures during laser transmittance. Device temp measurements of optically transparent etched device (Device 1) and opaque bottom channel device (Device 2) with temperature measurements at 15 min intervals over 3 hrs. Temperature measurements taken on side opposite of laser transmittance on back side of etched channels

Appendix B: Additional Information for Chapter 4

B.1 KYTOS and MATLAB image analysis definitions

All of these parameters are analyzed and logged for every single particle that triggers an event. Event triggers are done based upon an integrated threshold (single brightest pixel and 8 nearest neighbors) across each stream number or a peak threshold (single brightest pixel) for each stream number.

UNMHamamatsu-ID: The focusing stream number in which the event occurs. For our current system there are 16-17 stream numbers and nodes depending upon the excitation frequency.

UNMHamamatsu-Frame: The camera frame number in which the event occurrs.

UNMHamamatsu-TOF: The number of frames that the particle has above the threshold.

UNMHamamatsu-PeakIntensity: The brightest single pixel on the camera data 16-bit scale within a particle time of flight through the laser excitation beam.

UNMHamamatsu-BPX: The brightest x position across the width (2048 pixels wide) of the camera. Used as a representation of particle position within the device.

UNMHamamatsu-Event: The event number.

Integrated Intensity: Integrated sum of all pixels within a single stream. This integrated intensity is stored as a waveform and the following parameters are extracted: A) UNMHamamatsu-Height, peak intensity of integrated waveform. Integrated intensity of brightest single frame. B) UNMHamamatsu-Width: The width of the waveform in number of frames. C) UNMHamamatsu-Area: Area of integrated waveform.

B.2 Ultra-rainbow 6 peak calibration beads

Six peak ultra-rainbow calibration beads (6 μm diameter, Spherotech) were used as a calibration standard to characterize the performance of our cytometer. The five fluorescent peaks are clearly visible in the center of the channel with CV's comparable to those acquired on a commercial flow cytometer (4-6%) and are clearly distinguishable from each other. It is also promising that we are in fact seeing the population of blank beads, but further analysis is needed to confirm this.

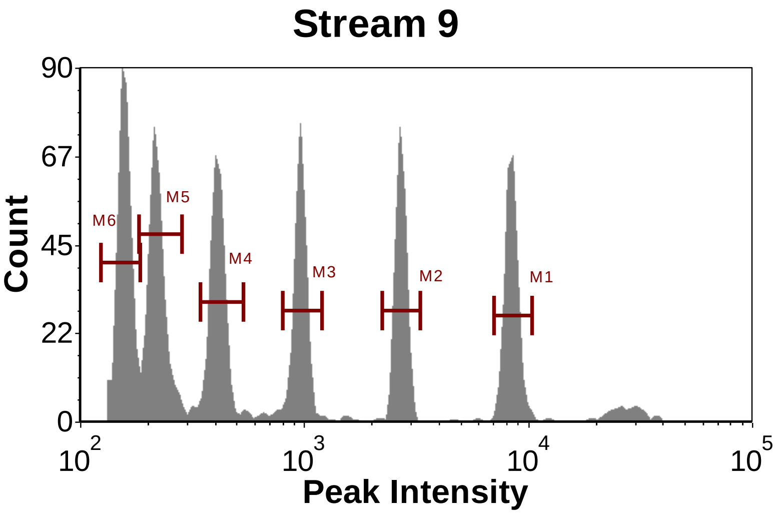

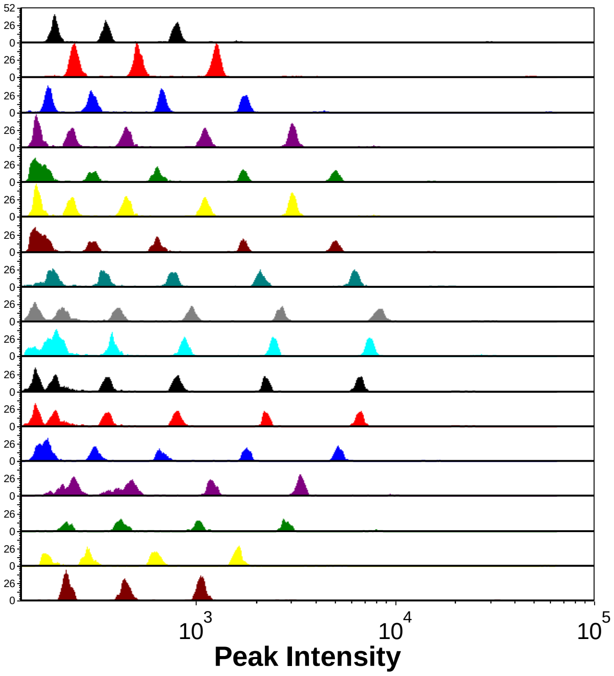

Figure B.2. Histograms of six-peak ultra-rainbow beads. The best performing stream (top) and all of the streams (bottom) with 6 µm calibration beads.

B.3 Sensitivity as a function of laser power

The sensitivity of our system increases linearly with the applied laser power. We can increase the absolute sensitivity of our system by increasing the applied laser power.

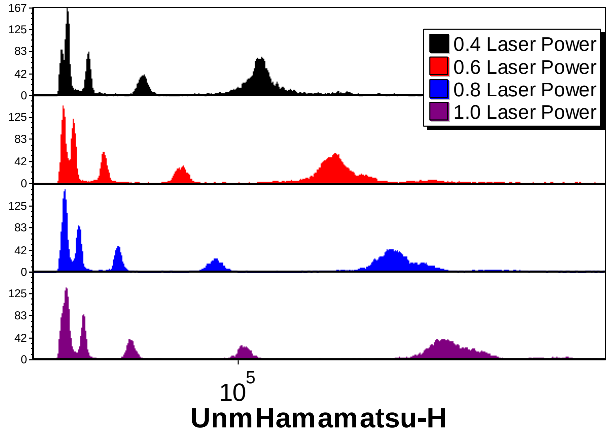

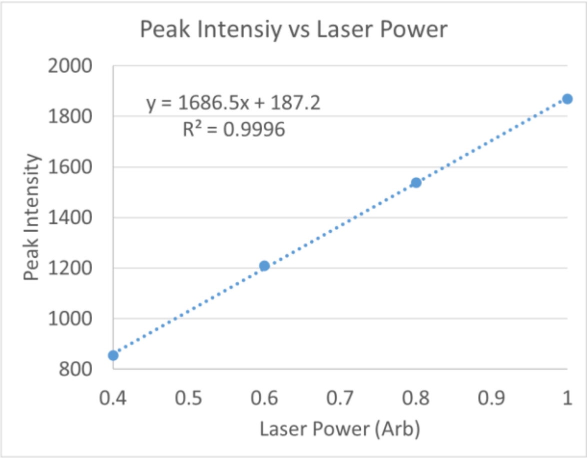

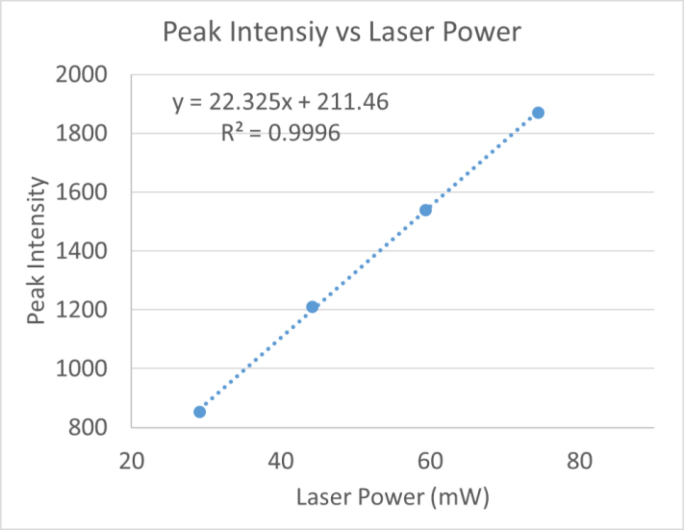

Figure B.3. Peak intensity vs laser power. Top: For a 6-peak bead population, we see that all bead populations increase in fluorescent intensity with applied laser power. Bottom: The peak intensity of the beads increase with applied laser power. With a relativity constant background noise, this leads to increased sensitivity with applied laser power.

B.4 Analysis of multiple colors

Analysis of multiple colors can be achieved without large system modifications. The acoustic focusing positions the particles such that there is a significant amount of free space on the camera chip. The addition of a small optical displacement and the appropriate filters yields a multi-color system as shown in Figure A3.5. We believe that a 5-color system could be achievable.

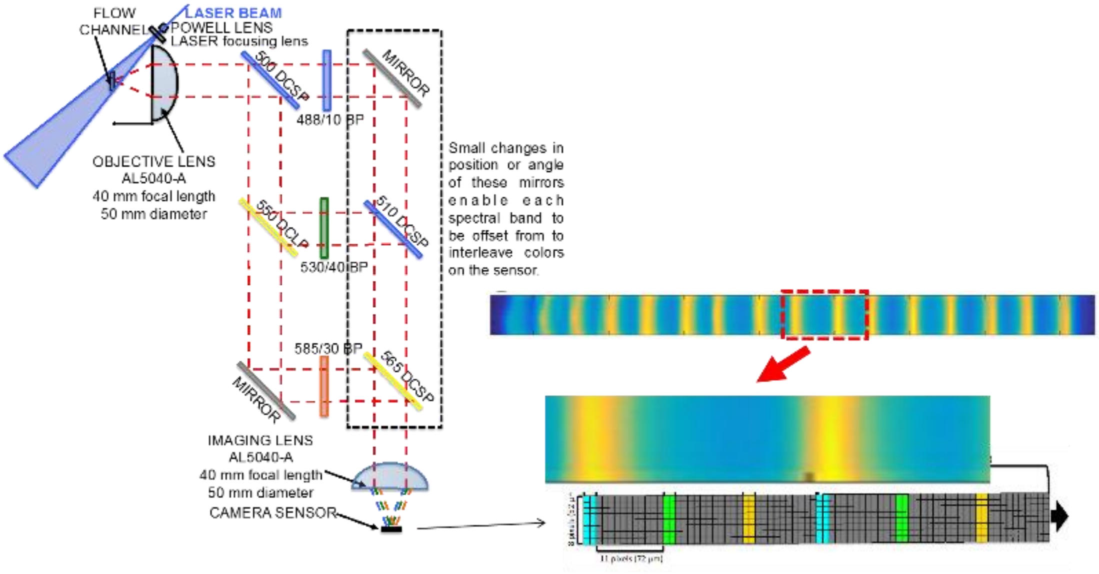

Figure B.4 Schematic of a multi-color instrumentation design.

B.5 Event rate vs flow rate

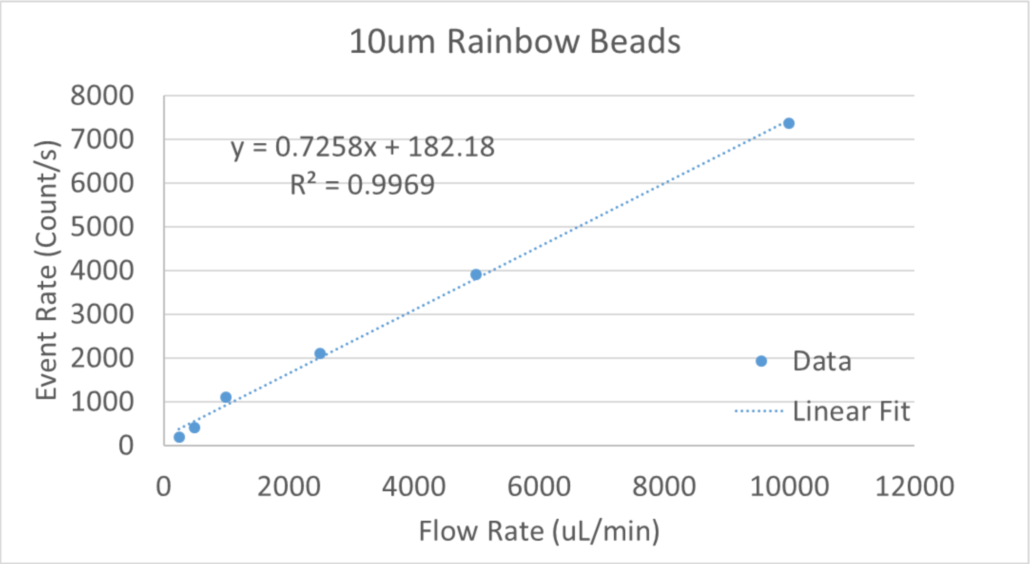

Figure B.5. Event rate vs flow rate. For a constant beads input, we see a linear relationship between event rate and input flow rate. This suggests that we are seeing all beads across the range of flow rates. We are not missing the fastest flowing beads at the highest flow rates.

B.6 Focusing width, intensity and CV, vs flow rate

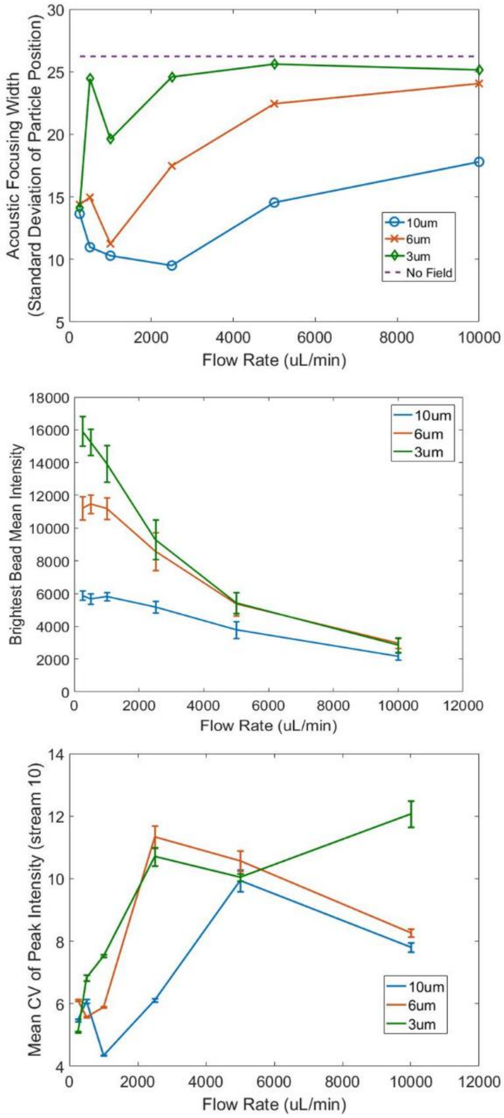

Figure B.6. Focusing width, intensity and CV, vs flow rate. Performance of standard beads vs. flow rate. (A) Focusing width (standard deviation of particle position relative to the mean particle position in each mode, averaged over all particle streams) vs. flow rate. (B) Mean intensity of the brightest bead population across flow rate. (C) Mean CV of all bead populations in stream 10 across flow rate.

Appendix C: Additional Information for Chapter 5

C.1 Instrument layout

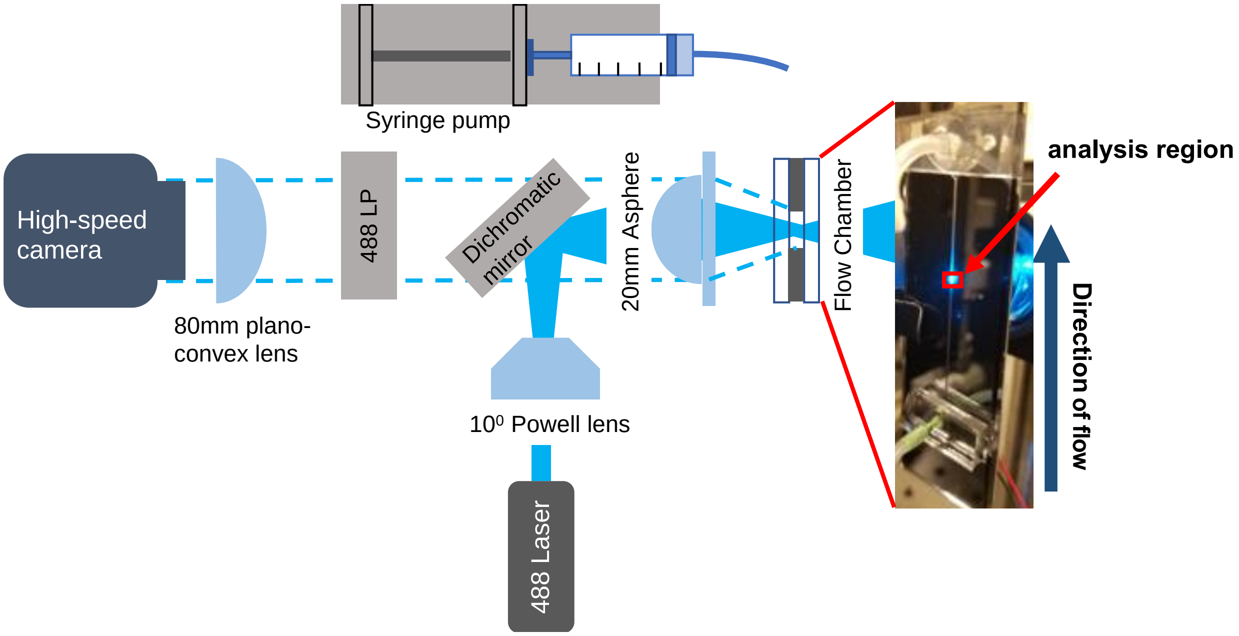

Figure C.1. Optical setup of custom flow cytometry system. A 150 mW 488 nm laser (MiniWhisperIT, Pavillion Integration Corporation, San Jose, CA) emits into a 10⁰ Powell Lens (Laserline Optics Canada Inc., Canada) and reflected off a dichromatic mirror (Semrock, Rochester, NY) into the 20 mm Aspherical lens (AL2520-A, ThorLabs, Inc. Newton, NJ) which focuses the beam into a ~2.3 mm wide by ~ 10 – 20 µm rectangular region. The exited fluorescent particle light emits back into the optical setup (denoted by the dashed line) and filtered by the 488 long-pass filter Lens (488 nm Edge Basic, Semrock, Rochester, NY) and into the 80 mm focal length plano-convex lens 25 mm diameter which transmits into the high speed sCMOS sensor (Hamamatsu Orca flash 4.0 v2).

C.2 1 µm particle position analysis (control)

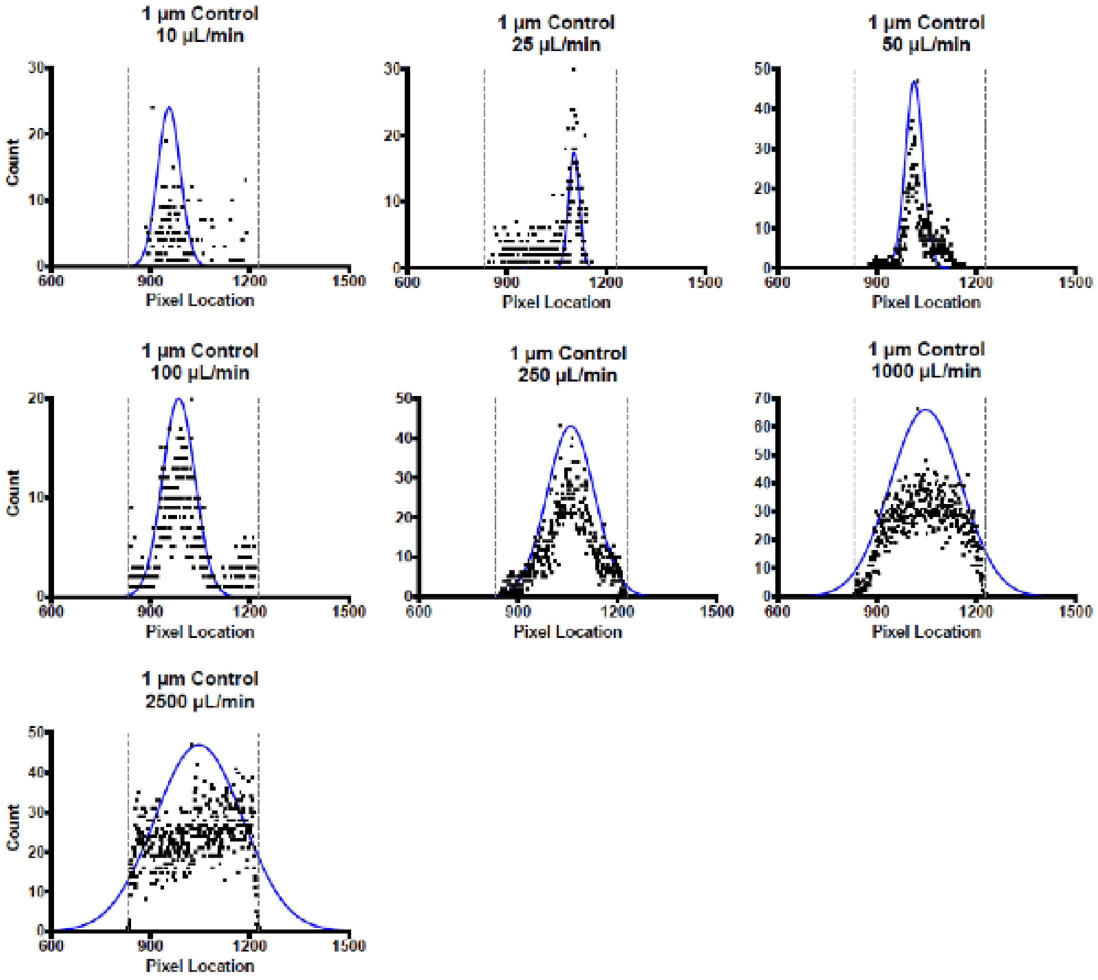

Figure C.2. 0.93 µm diameter particle histogram position focusing data with the 1.5 MHz transducer activated and no bubbles added (control data). The 0.93 particles do not focus well across all the experimental flow rates. Due to the poor focusing quality we did not analyze any bubble experimental data. Data was taken between 2 minutes for the higher flow rates (250 µL/min to 2,500 µL/min) and 15 minutes for the lower flow rates (10 µL/min to 100 µL/min). The gray dotted lines represent the channel wall's physical bounds across a zoomed in region (600 to 1500 pixels) of the total 2048-pixel width. The blue line is a gaussian curve fit to the data.

C.3 3 µm particle position analysis (control)

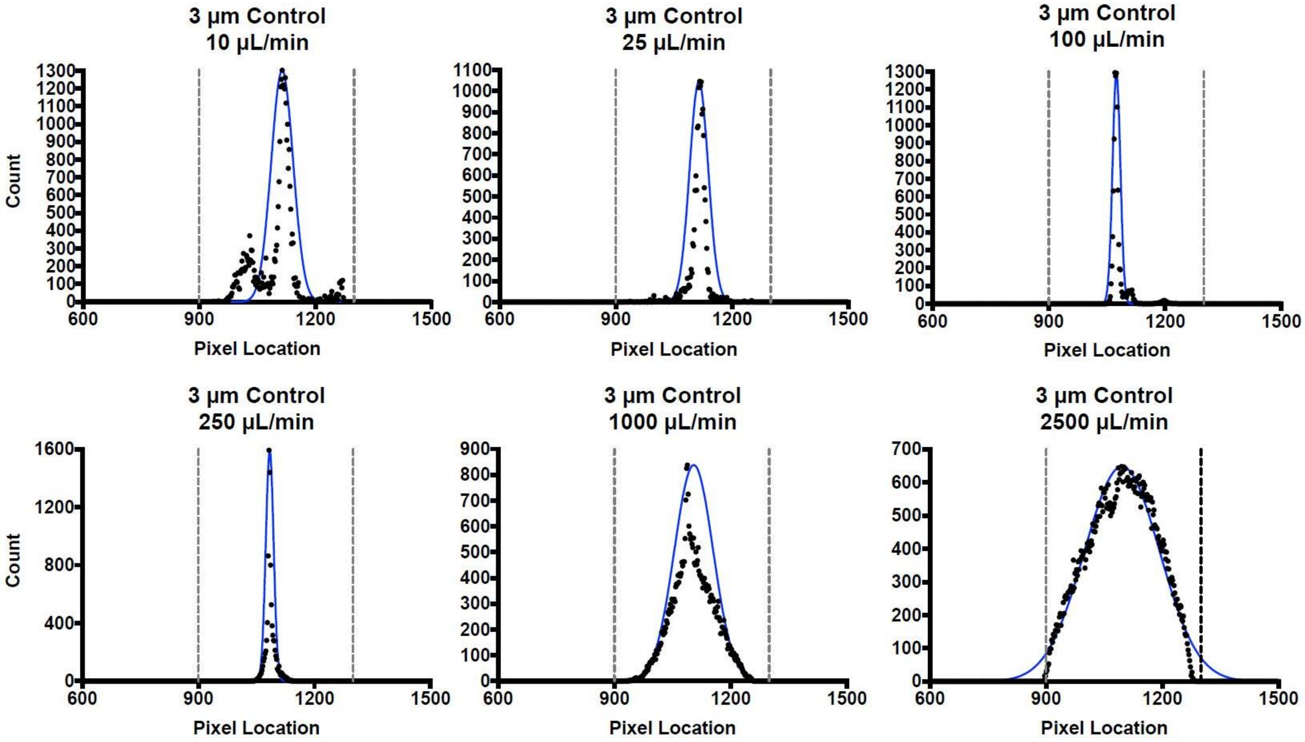

Figure C.3. 3 µm diameter particle histogram position focusing data with the 1.5 MHz transducer activated and no bubbles added (control data). The 3 µm particles focus significantly better than the 0.93 µm particles as is illustrated by the much tighter gaussian fits to the data sets. Data was taken between 2 minutes for the higher flow rates (250 µL/min to 2,500 µL/min) and 15 minutes for the lower flow rates (10 µL/min to 100 µL/min). The gray dotted lines represent the channel wall's physical bounds across a zoomed in region (between 500 and 1800 pixels) of the total 2048-pixel width. The blue line is a gaussian curve fit to the data.

C.4 3 μm particle position analysis (recovery after bubble)

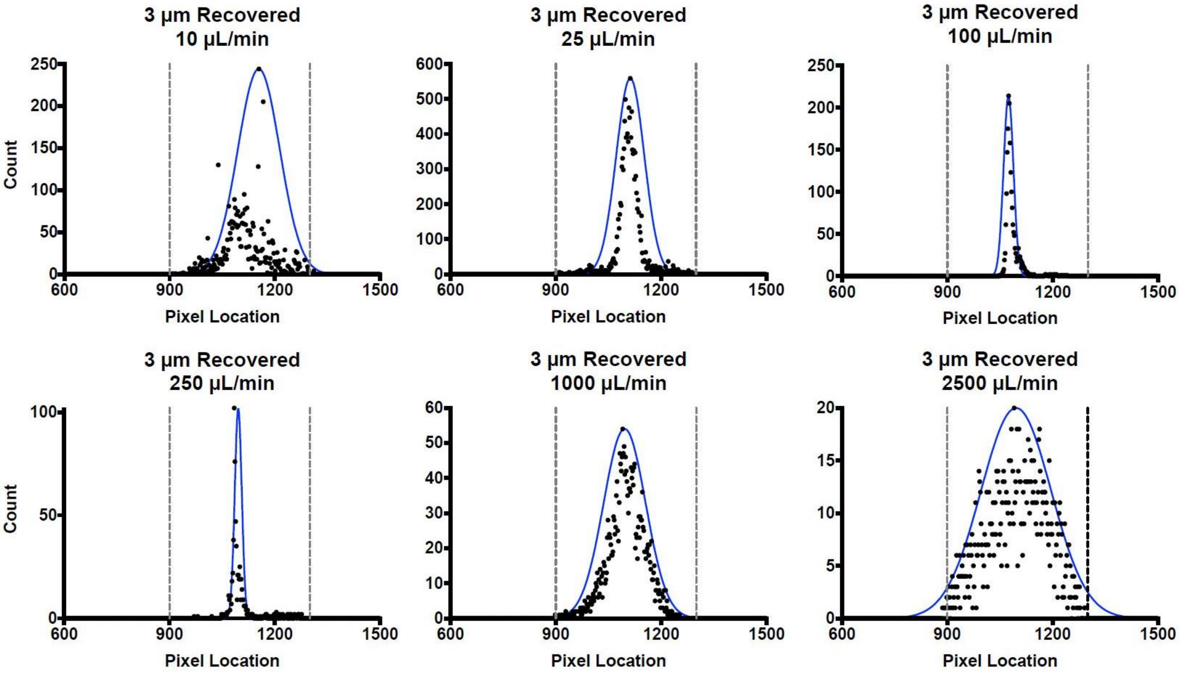

Figure C.4. 3 μm diameter particle histogram position focusing recovery data after the first bubble with the 1.5 MHz transducer activated (stream focus recovery data). Data was taken from a manually inserted gate over the region between the first bubble and the start of the second. The gray dotted lines represent the channel wall's physical bounds across a zoomed in region (between 600 and 1500 pixels) of the total 2048-pixel width. The blue line is a gaussian curve fit to the data.

C.5 6 µm particle position analysis (control)

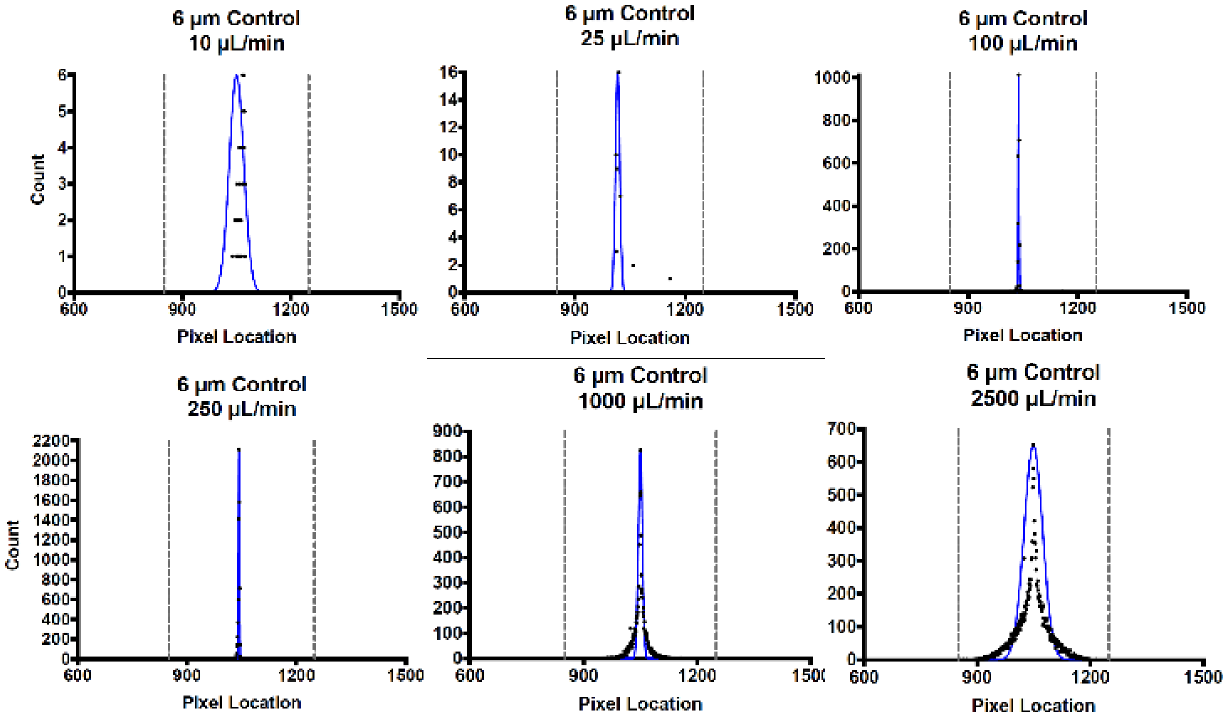

Figure C.5. 6 µm diameter particle histogram position focusing data with the 1.5 MHz transducer activated and no bubbles added (control data). The 6 µm particles focus largely across all flow rates with the optimal range between 100-1000 µL/min. Data was taken between 2 minutes for the higher flow rates (250 µL/min to 2,500 µL/min) and 15 minutes for the lower flow rates (10 µL/min to 100 µL/min). The gray dotted lines represent the channel wall's physical bounds across a zoomed in region (between 600 and 1500 pixels) of the total 2048-pixel width. The blue line is a gaussian curve fit to the data.

C.6 6 μm particle position analysis (recovery after bubble) C.6.

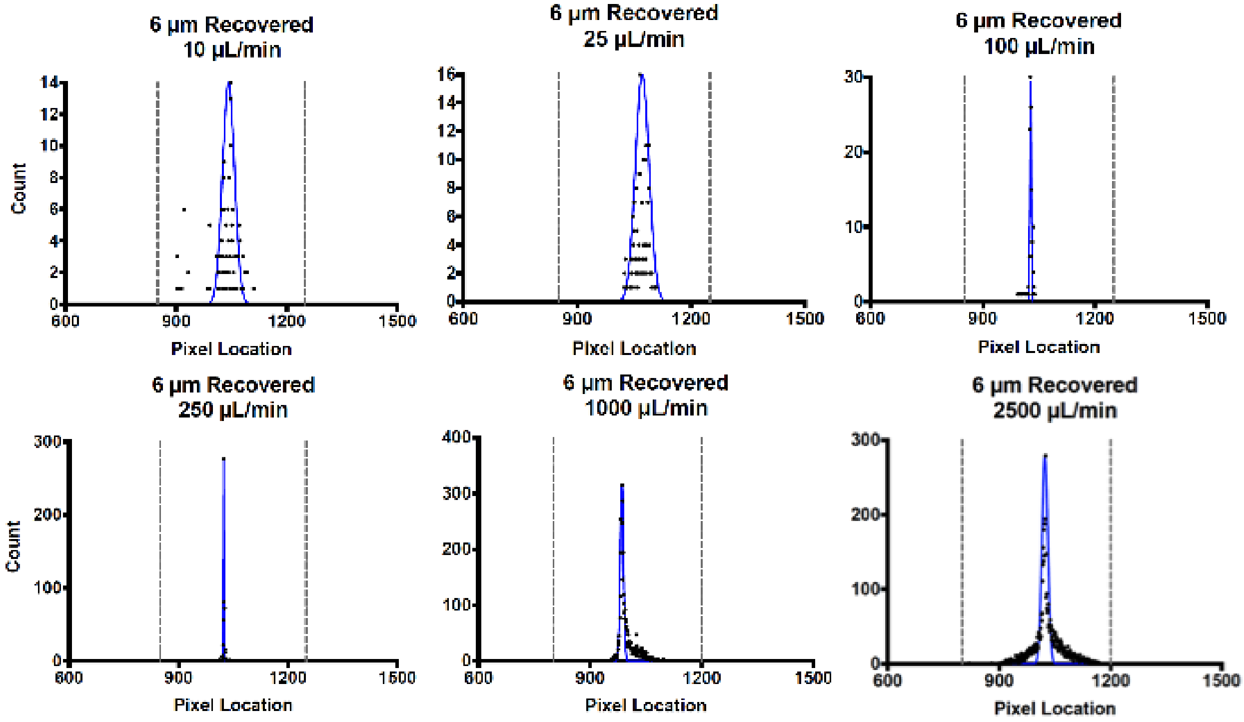

Figure C.6. 6 μm diameter particle histogram position focusing recovery data after the first bubble with the 1.5 MHz transducer activated (stream focus recovery data). Data was taken from a manually inserted gate over the region between the first bubble and the start of the second. The gray dotted lines represent the channel wall's physical bounds across a zoomed in region (between 600 and 1500 pixels) of the total 2048-pixel width. The blue line is a gaussian curve fit to the data.

C.7 10 µm particle position analysis (control)

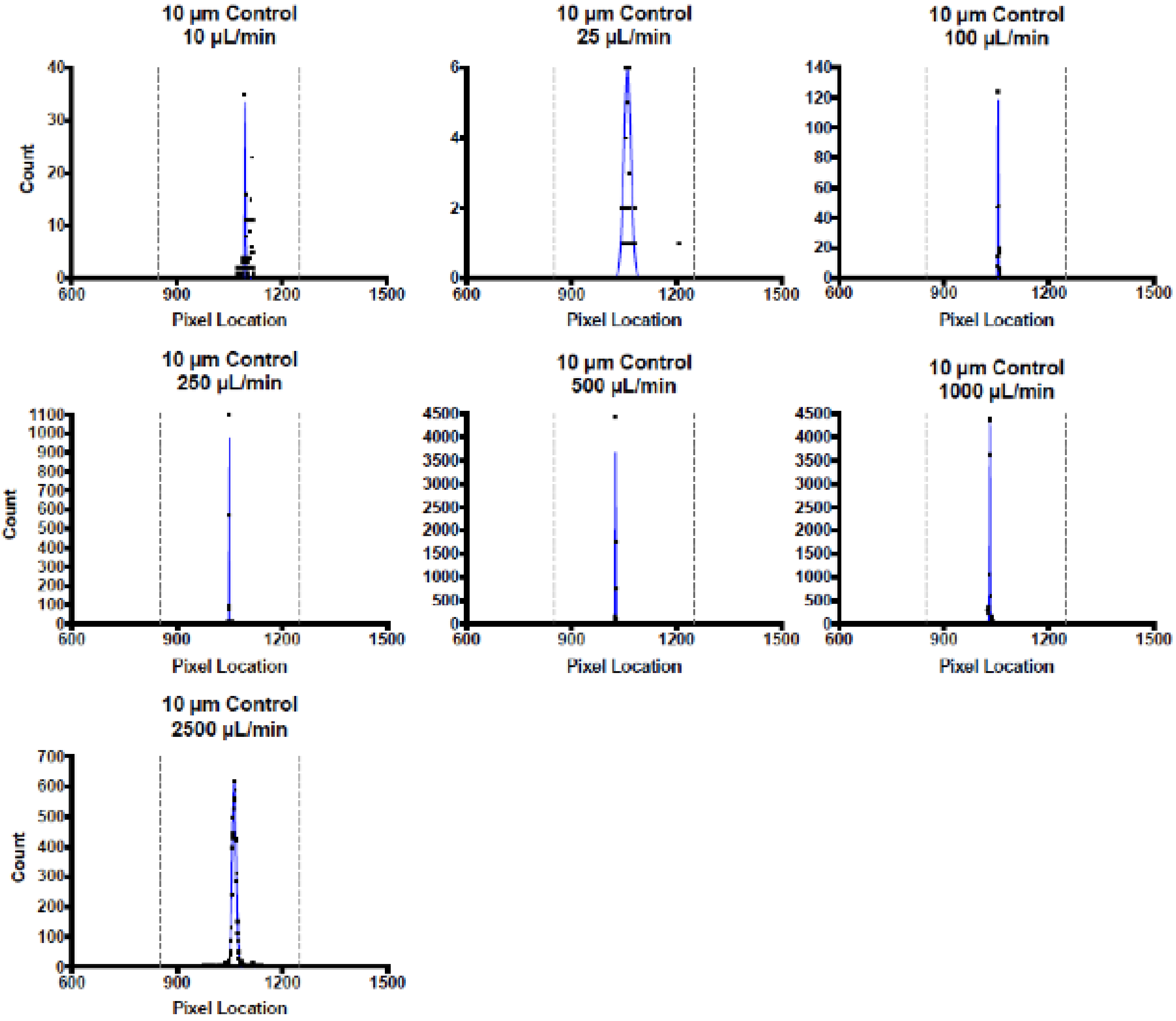

Figure C.7. 10 µm diameter particle histogram position focusing data with the 1.5 MHz transducer activated and no bubbles added (control data). As with the 6 µm particles, the 10 µm particles focus largely across all flow rates with the optimal range between 100-1000 µL/min. Data was taken between 2 minutes for the higher flow rates (250 µL/min to 2,500 µL/min) and 15 minutes for the lower flow rates (10 µL/min to 100 µL/min). The gray dotted lines represent the channel wall's physical bounds across a zoomed in region (between 600 and 1500 pixels) of the total 2048-pixel width. The blue line is a gaussian curve fit to the data.

C.8 10 µm particle position analysis (recovery after bubble) C.8

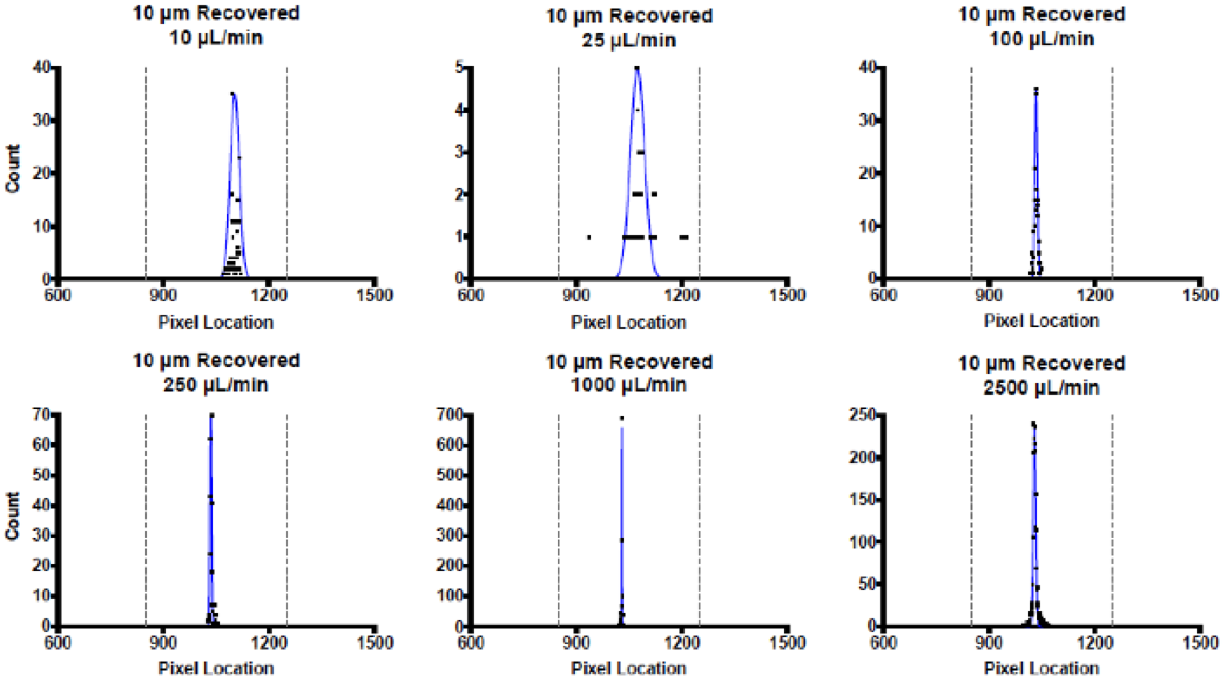
10 µm Recovered 10 µL/min

10 µm Recovered 25 µL/min

10 µm Recovered 100 µL/min

10 µm Recovered 250 µL/min

10 µm Recovered 1000 µL/min

10 µm Recovered 2500 µL/min

Figure C.8. 10 µm diameter particle histogram position focusing recovery data after the first bubble with the 1.5 MHz transducer activated (stream focus recovery data). Data was taken from a manually inserted gate over the region between the first bubble and the start of the second. The gray dotted lines represent the channel wall's physical bounds across a zoomed in region (between 600 and 1500 pixels) of the total 2048-pixel width. The blue line is a gaussian curve fit to the data.

C.9 2500 μL/min with inset

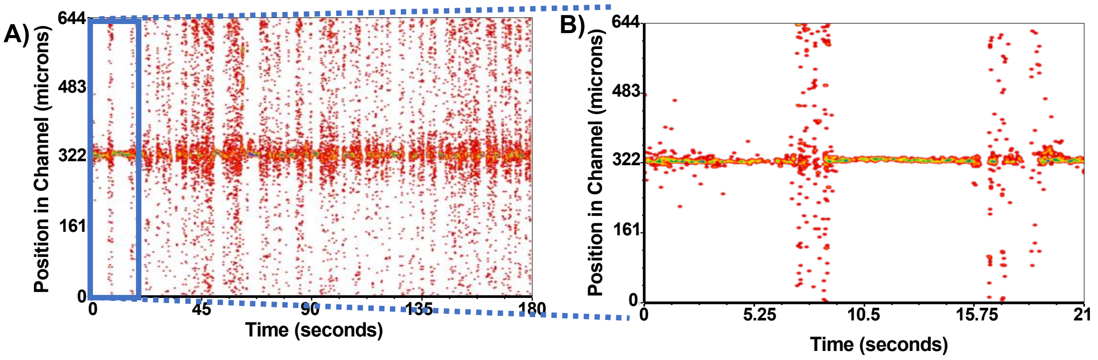

Figure C.9. 6 μm diameter particle acoustically focused at a flow rate of 2,500 μL/min with several manually sampled bubbles over a three-minute period. The 1024 X 1024 resolution data was zoomed in on, as shown by the blue box, to more clearly show sample stream recovery between bubbles.

C.10 6 μm mean position tracking with inset

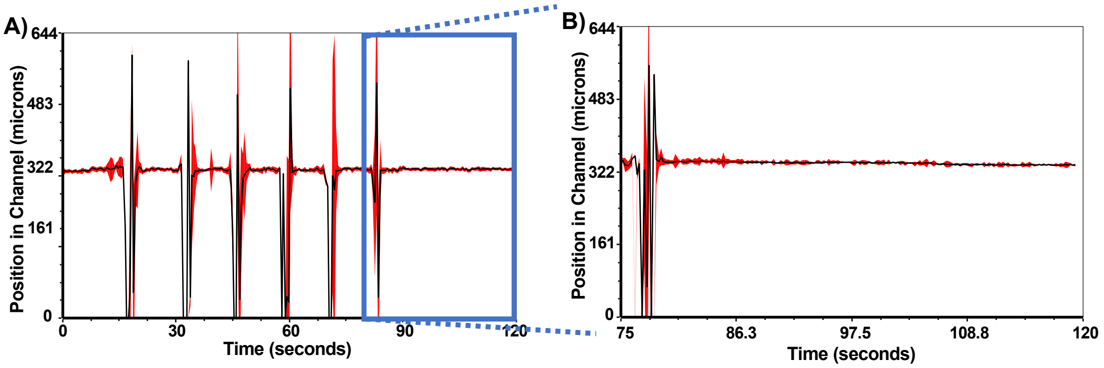

Figure C.10. 6 μm diameter particle acoustically focused at a flow rate of 250 μL/min with six automatically sampled bubble regions over a two-minute period. The data shown is a mean trace (black) with standard deviation (red) of each bin in 256 X 256 resolution. The data was zoomed in on, as shown by the blue box, to more clearly show the mean position trace of the recovered stream following the final bubble.

Table of FWHM values C.T1.

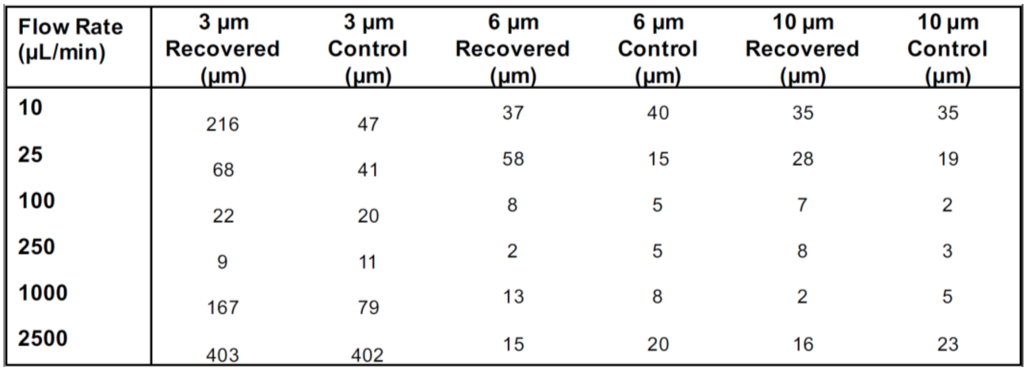

Flow Rate (µL/min)	3 µm Recovered (µm)	3 µm Control (µm)	6 µm Recovered (µm)	6 µm Control (µm)	10 µm Recovered (µm)	10 µm Control (µm)
10	216	47	37	40	35	35
25	68	41	58	15	28	19
100	22	20	8	5	7	2
250	9	11	2	5	8	3
1000	167	79	13	8	2	5
2500	403	402	15	20	16	23

Table C.T1. Table of 3, 6, 10 µm particle FWHM stream width values (in µm). Each FWHM value is converted from pixel values of each particle position histogram by a factor of 1.67 µm/pixel. This was done to better conceptualize how tight the streams are. The value represents how wide the particle streams are outside the diameter of a particle. For example, a FWHM of zero would mean that particle stream is perfectly focused to the diameter of the particle with no variation in position.

Appendix D: Additional Information for Chapter 6

D.1 Additional supporting figure

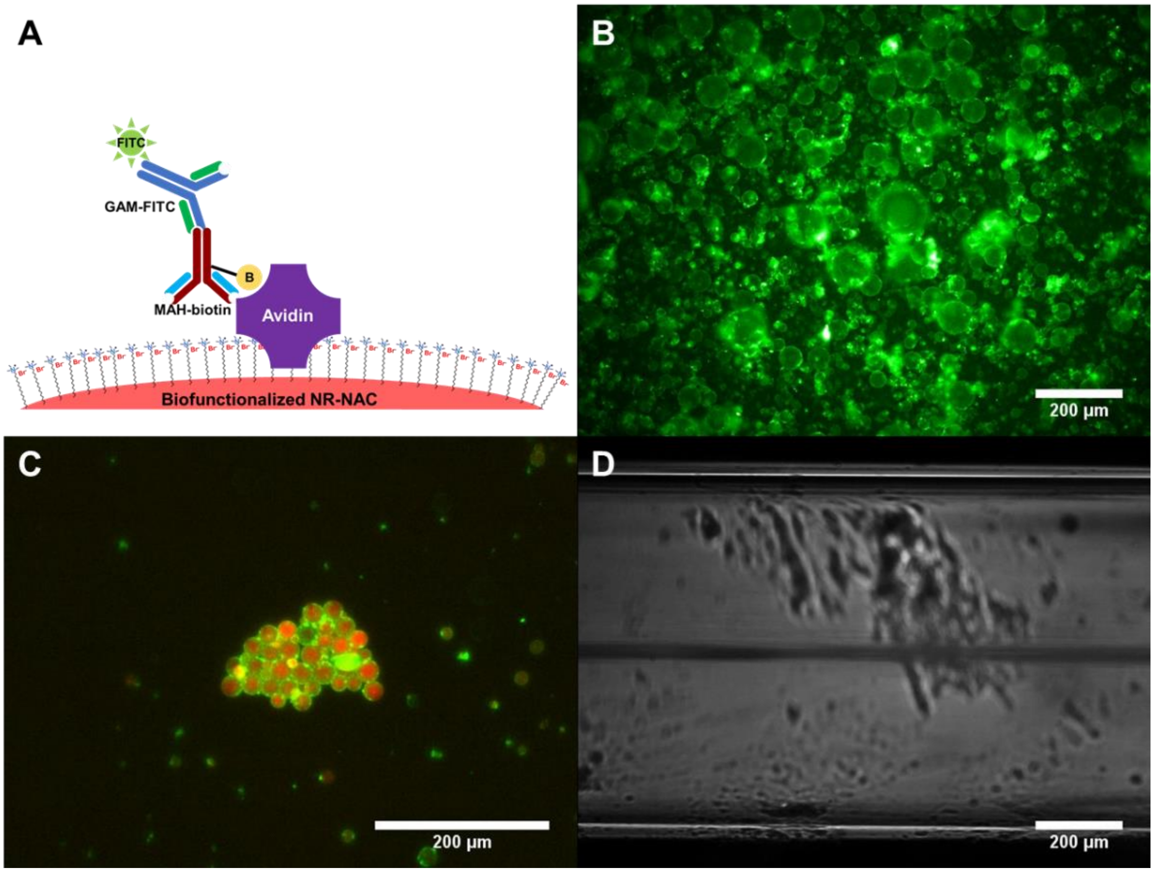

Figure D.1. Supporting figures of functionalized particles and prbc focusing. (A) Illustration of NAC biofunctionalized surface. Biomolecular complex of passively adsorbed avidin bound after incubation to biotinylated mouse antihuman Ab. Secondary FITC labeled goat anti-mouse Ab binds specifically to target primary antibody forming complex. (B) Colorized green channel fluorescence image of high concentration unstained NACs labeled with secondary Ab (GAM-FITC). Particles were incubated with secondary Ab target in buffer solution. (C) Red and green fluorescence channel overlay of NR stained NACs cluster with secondary Ab on the surface (green). particles were incubated in buffer solution. (D) Brightfield image of capillary device acoustically focusing prbcs downstream of PZT transducer. Scale bars = 200 µm.

D.2 Schematic of capillary device and syringe setup

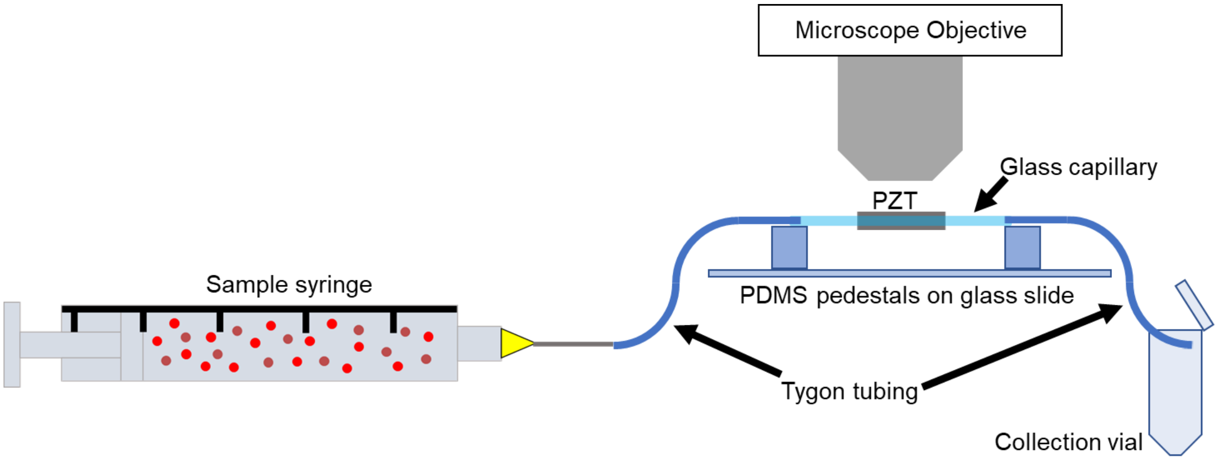

Figure D.2. Device schematic. 5 mL plastic syringe infuses sample via syringe pump through Tygon tubing at 200 µL/min into capillary device with PZT. Contents are trapped or focused depending on their acoustic contrast during PZT actuation. Positive contrast media is pumped into a 1.5 mL microcentrifuge tube while trapped contents remain within capillary. Capillary device is suspended on PDMS pedestals under epifluorescent microscope objective for imaging.

D.3 Images of preliminary work towards monodispered particle synthesis

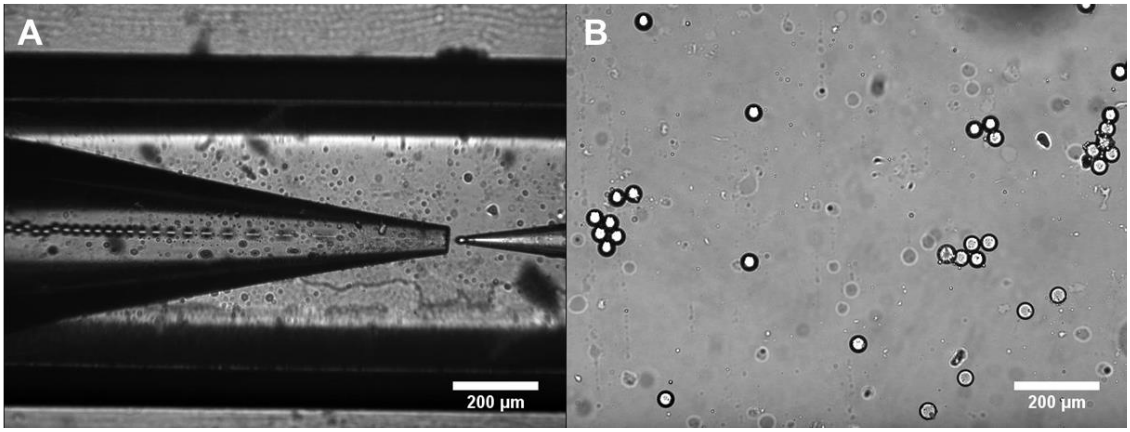

Figure D.3. Microfluidic device for monodisperse NAC synthesis. Glass capillary microfluidic device using 1% BSA in water (outer fluidic phase) and 1:1 ratio of toluene to PDMS; 10:2 prepolymer to curing agent Sylgaurd 184 (inner phase). (A) 20 µm ID injection tip infusing the organic PDMS phase at 200 µL/hr into the co flowing 1% BSA in water outer phase flowing at 10,000 µL/hr into the

60 µm ID collection capillary tip. (B) 10X magnification of collected sample with largely monodispersed PDMS particles. The excess toluene organic solvent makes the particles jelly-like as opposed to more solid and rubbery from our polydispersed particle synthesis method (scale bars 200 µm).

Appendix E: Additional Information for Chapter 7

E.1 Rheology methods and results

Rheology

A Discovery Hybrid Rheometer HR-3 with the 40 mm 2.0 cone plate, peltier plate steel geometry has been used to do the rheology analysis. Each sample was loaded two times on the rheometer and the experiment was repeated for three times for each load. The rheological characteristic of the samples has been analyzed with two different method. The first one is the frequency sweep with the angular frequency from 628 to 0.1 rad/s and the second one is the flow ramp with shear rate from 0.01 to 1000 1/s. The young and storage modulus and complex viscosity can be obtained from the frequency sweep test and the viscosity can be obtained from the flow ramp test (used for Figure 2 of the manuscript). Each measurement has been repeated three for consistency of the results.

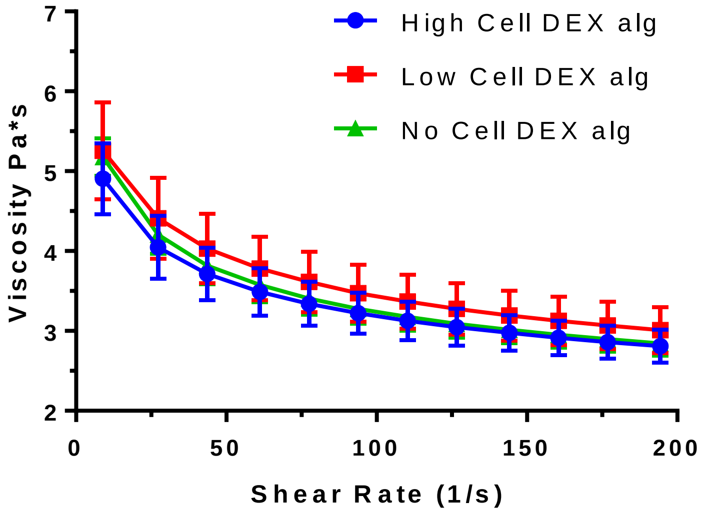

Figure E.1. Viscosity vs shear rate. Complex viscosity measurements done by collaborators at New Mexico State University. No significant change in viscosity measurements in solutions with high (blue), low (red), or no cells.

The results obtained for the following solutions of PEG and DEX are listed below. We chose these solutions to observe whether cell concentration affects viscosity which therefore affects the droplet generation capabilities of our microfluidic device.

1. DEX+PBS (no, low, and high cell)
2. ALG+PBS (no, low, and high cell)
3. DEX+PBS (no, low, and high cell)
4. ALG (no, low, and high cell)
5. DEX (no, low, and high cell)

From our results we conclude the viscosity variations are within error of each other for each solution, and therefore is not the reason for the difference in droplet generation. Cell clumping may provide reasoning for the disruption of hydrogel formation.